The formation of brown dwarfs as revealed by the mass function of IC 2391

Steve Boudreault
Max-Planck-Institut für Astronomie

Heidelberg 2008

Dissertation in Astronomy
submitted to the
Combined Faculties for the Natural Sciences and for Mathematics
of the Ruperto-Carola University of Heidelberg, Germany.
for the degree of
Doctor of Natural Sciences

presented by
Dipl.-Astron. *Steve Boudreault*
born in Sept-Îles, Canada
Oral examination: 20.11.2008, 14:00 pm

The formation of brown dwarfs as revealed by the mass function of IC 2391

Referees: Prof. Dr. Ralf S. Klessen
            Dr. Coryn A.L. Bailer-Jones

Abstract

This PhD thesis deals with the formation and evolution of brown dwarfs. Here, we present the stellar and substellar mass function of the open cluster IC 2391, plus its radial dependence, and use this to put constraints on the formation mechanism of brown dwarfs. Our multiband optical and infrared photometric survey with spectroscopic follow up covers 11 square degrees, making it the largest survey of this cluster to date. We observe that there is no variation in the mass function over the stellar/substellar boundary at all three cluster radius intervals analyzed. From this lack of discontinuity, we conclude that the stellar embryo ejection mechanism cannot be the unique brown dwarf formation path if this formation mechanism produces a higher velocity dispersion for brown dwarfs than the stars obtain. Alternatively, the ejection mechanism could be a dominant brown dwarf formation path only if it produces the same velocity dispersion for brown dwarfs as exists for stars in the cluster. In addition, we observe a radial variation in the mass function over the range 0.15 to $0.5\,\mathrm{M_\odot}$. We conclude that this is a signature of mass segregation via dynamical evolution. Analysis of mass functions of other open clusters from different ages and environment, at each side of the stellar/substellar boundary, also indicates that dynamical evolution influences the shape of the mass function.

Zusammenfassung

Diese Dissertation behandelt die Entstehung und Entwicklung von Braunen Zwergen. In ihr wird die stellare und substellare Massenfunktion des offenen Sternhaufens IC 2391 einschließlich ihrer radialen Abhängigkeit untersucht und die gefundenen Ergebnisse werden dazu verwendet Randbedingungen für die Entstehungsmechanismen von Braunen Zwergen zu ermitteln. Unsere photometrische Vielfarbenuntersuchung im optischen und infraroten Bereich überdeckt elf Quadratgrad. Dies ist die bisher umfassendste Studie dieses Haufens. Wir haben in der Massenfunktion keine Änderung beim Übergang von der stellaren zur substellaren Grenze gefunden; dies gilt für alle drei untersuchten ringförmigen Haufenregionen. Aus dieser Stetigkeit schließen wir, dass der Auswurfmechanismus von stellaren Embryos nicht der einzige Entstehungsmechanismus von Brauner Zwergen sein kann, falls dieser Entstehungsprozess eine höhere Geschwindigkeitsverteilung für Braune Zwerge als für Sterne zur Folge hat. Der Auswurfmechanismus könnte nur dann ein dominanter Entstehungsmechanismus Brauner Zwerge sein, falls er dieselbe Geschwindigkeitsverteilung für Braune Zwerge und Sterne in dem Haufen erzeugt. Zusätzlich beobachten wir eine radiale Änderung in der Massenfunktion im Bereich von 0.15 bis $0.5\,\mathrm{M_\odot}$. Wir schließen daraus, dass es sich um ein Anzeichen für Massensegregation durch dynamische Entwicklung handelt. Die Analyse der Massenfunktion beidseitig der stellaren/substellaren Grenze in anderer offener Sternhaufen unterschiedlichen Alters und in unterschiedlichen Umgebungen deutet auch darauf hin, dass dynamische Evolution die Form der Massenfunktion beeinflusst.

Contents

Chapter 1

Introduction

1.1 Brown dwarfs

Most of the visible light in the Universe comes from stars. All stars on the main sequence are massive enough to burn hydrogen in their core by nuclear reactions. They are in hydrostatic equilibrium since the internal energy provided by nuclear burning balances the gravitational contraction. However, there are objects that are not massive enough to maintain hydrogen-burning in their cores and these objects will cool down as they evolve.

Theories that first suggested the existence of such objects go back to the work of Kumar (1963). In a study of the structure of stars from 0.04 to $0.09\,M_\odot$, Kumar (1963) computed that there is a lower limit for normal stellar evolution. That is, would not reach the main sequence but could become a completely degenerate object. (This limit was estimated to be $0.07\,M_\odot$ for objects with a composition similar population I stars and $0.09\,M_\odot$ for that of composition similar to population II stars.) The existance of such objects was also predicted independently by Hayashi et al. (1963). The first calculation the lower limit of the main sequence was performed by Grossman (1970) where the mass obtained was $0.075\,M_\odot$. Today, it is known that this hydrogen-burning limit will depend on the chemical composition of the object : $0.07\,M_\odot$ assuming a solar composition or $0.08\,M_\odot$ for low metallicity ($Z/Z_\odot = 0.01$, Chabrier & Baraffe 2000). The term *brown dwarf* was first proposed by Tarter (1975) for objects below this limit.

However, the first *bona fide* discovery of a brown dwarf was only reported two decades later by Kulkarni & Golimowski (1995) with the observation of Gl 229B. Indeed, it was already pointed out by D'Antona & Mazzitelli (1985) that observations of brown dwarfs would be difficult since, although deuterium fusion can occur down to $\sim 0.011\,M_\odot$ (Saumon et al. 1996), nuclear burning in the core can't overcome the gravitational contraction. Therefore, these objects will contract and cool with time and, therefore, will become fainter with age.

D'Antona & Mazzitelli (1985) have reported that all objects from 0.04 to 0.07 $M_\odot$ reach the luminosity of $\log(L/L_\odot) = -5$ in a time equal or less that the age of local galactic disk (lower limit of 9.5 Gyr, Bergeron et al. 2001). We show, in Figure 1.1, the evolution of the central (*left panel*) and effective temperature (*right panel*) of stellar and substellar objects with time. We can see that stellar objects (with mass of 0.075 $M_\odot$ and higher) reach their main sequence phase with a constant temperature, both in the core and in the photosphere of the star.

The main goal of the thesis is to bring new constraints on insights into the possible formation mechanisms of brown dwarfs.
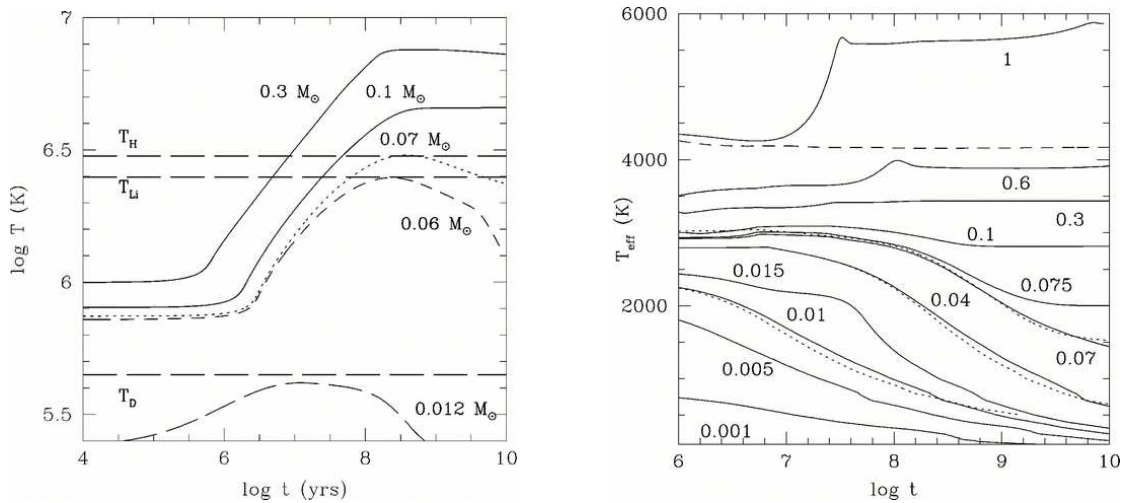
Figure 1.1 Central temperature (*left panel*) and effective temperature (*right panel*) versus time (in yr) for different masses. For stellar objects (i.e. for objects above the hydrogen-burning limit), we recognise that these objects reach the main sequence with a constant central and effective temperature. However, we observe that brown dwarfs, below the hydrogen-burning limit, will cool as they evolve in time. Figure from Chabrier & Baraffe (2000).

1.2   Possible formation mechanisms of brown dwarfs

Brown dwarfs have masses between those of mass hydrogen-burning stars (0.072 $M_\odot$, Basri 2000) and giant planets (13 M_J is a proposed lower mass limit for brown dwarfs, Basri 2000[1]). There is still no common agreement on a unique formation process for these objects.

---

[1]There is still some debate today about the definition of planets. However, in this thesis, we will use the definition presented by the *Working Group on Extrasolar Planets (WGESP) of the International As-*

Among the several formation mechanisms that have been proposed, brown dwarfs can be formed in a similar way to stars, which is from the **compression and fragmentation of a dense molecular cloud**. Otherwise, brown dwarfs can be **formed like planets** from accretion of gas by rocky cores in circumstellar disk. Finally, they can be formed like stars, but with the accretion process interrupted during the protostellar stage (by **photoevaporation** of the accretion envelope by radiation from a nearby massive star or by **dynamical ejection** of the brown dwarf from its accretion envelope).

In the following subsections, we will describe the four formation scenarios and give observational signatures, as well as arguments against each of them.

1.2.1   Star-like formation

Formation of stars will occur in cores of molecular clouds when they become gravitationally unstable due to disturbance (e.g. from shockwaves from supernovae). This disturbance will not propagate like a wave but will grow exponentially if its wavelength exceeds the Jeans wavelength λ_{Jeans},

$$\lambda_{Jeans} \; = \; c_s \left(\frac{\pi}{G \, \rho_0} \right)^{1/2} ,$$
(1.1)

where c_s is the sound speed and ρ_0 the mean density of the star-forming cloud while G is the gravitational constant ($6.67260 \times 10^{-8}\,\mathrm{cm^3\,g^{-1}\,s^{-2}}$). If the wavelengths of disturbance are shorter then the Jeans wavelength, they will propagate away at the speed of sound. Part of the gravitational energy lost will increase the temperature of the core while the rest will be radiated away by infrared emission. Deuterium fusion ignition occurs when the density and temperature are high enough. While material continues to be accreted onto the protostar, the hydrogen begins to fuse in the core of the star, and finally, the rest of the enveloping material is cleared away by emission and stellar winds. The Jeans mass M_{Jeans}, which is the mass enclosed in a sphere radius of $\lambda_{Jeans}/2$, is related to the sound speed c_s and mean density ρ_0 of the star-forming cloud with the following equation,

$$M_{Jeans} \; = \; \frac{\pi^{(5/2)} \, c_s^3}{6 \, G^{3/2} \, \rho_0^{1/2}} .$$
(1.2)

tronomical Union, which is that objects below the the limiting mass for thermonuclear fusion of deuterium (set at $13\,\mathrm{M_J}$) are *planets*, objects with masses above the hydrogen-burning lmit (set at $0.072\,\mathrm{M_\odot}$) are stars and objects with masss between $13\,\mathrm{M_J}$ and $0.072\,\mathrm{M_\odot}$ are brown dwarfs, where $1\,\mathrm{M_\odot} = 1047.56\,\mathrm{M_J}$.

This assumes that the collapsing region of the cloud is surrounded by an infinite and static medium.

Assuming that the Jeans mass gives the lower limit of an object formed by the compression and fragmentation of a dense molecular cloud and that the mean density and temperature of a star-forming cloud can give a Jeans mass of several $M_\odot$ (Padoan & Nordlund 2004), it can ruled out that brown dwarfs formed like stars. However, Elmegreen (1999) used analytic arguments to justify that, in a region of ultracool CO gas (such as in the inner disk of M31), the Jeans mass could be as low as $\sim 0.01\,M_\odot$. Numerical simulations of Padoan & Nordlund (2004) also result in objects with substellar masses in a very cold environment ($10\,K$). In the situation of a formation process similar to stars (from compression and fragmentation of molecular clouds), one would expect brown dwarfs to have similar proprieties to stars (e.g. presence of circumstellar disk, same kinematics and spatial distribution as stars at birth; Luhman et al. 2007a gives a review of other observational signatures of brown dwarf formation as star-like). For instance, circumstellar disks are observed around young stars ($\lesssim 10\,Myr$) and should be detected around young substellar objects as well. Such disks have indeed been observed around brown dwarfs (recently, Luhman et al. 2007a detected an edge-on circumstellar disk around a brown dwarf), and moreover, Luhman et al. (2005) have observed a similar ratio of low mass stars and substellar objects which exhibit excess emission indicative of circumstellar disks. Also, one could expect to observe similar kinematics and spatial distributions for stellar and substellar objects. This was observed by Joergens (2006) where radial velocities of brown dwarfs in Chamaeleon I and in Taurus were similar to low mass stars, while the spatial distribution of stars were observed to be similar to the spatial distribution of brown dwarfs in Taurus (Figure 1.2, Luhman et al. 2006). From these observations among others, Luhman et al. (2007a) concluded that there was a common formation mechanism for brown dwarfs and stars.

1.2.2   Formation by gravitational instability of a disk

On the other hand, numerical simulations have been able to produce substellar companions in protostellar disks from gravitational instabilities. Among them, Pickett et al. (2000) presented a simulation of a $0.133\,M_\odot$ disk around a $1\,M_\odot$ protostar, extending from 0.76 to 10 AU, where a *clump* of $0.034\,M_\odot$ was produced at 5.4 AU from its protostellar host. From analytic considerations, Whitworth & Stamatellos (2006) concluded that gravitational fragmentation in disks at small radii (distance from disk centre $\lesssim 30\,AU$) was difficult since the timescale on which a protofragment can cool down and condense is longer than the timescale on which that protofragment is sheared apart. This could explain the low frequency of brown dwarfs found around Sun-like stars at small radii (also known as the
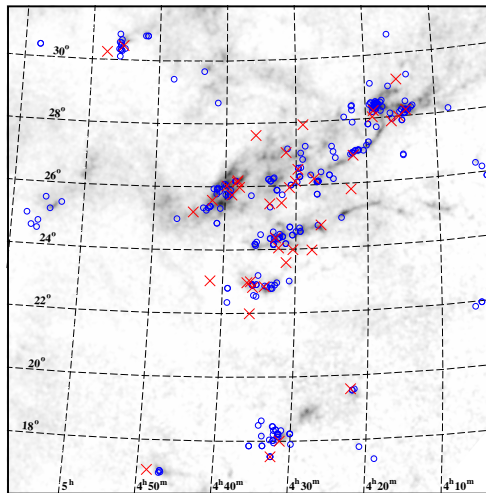
Figure 1.2 Spatial distribution of stars (*circles*) and brown dwarfs (*crosses*) in Taurus. We can observe a similar spatial distribution for stellar and substellar objects. Figure from Luhman et al. (2007c).

brown dwarf desert). However, Whitworth & Stamatellos (2006) obtained from their numerical simulation that fragmentation at larger radii ($\gtrsim 100\,\mathrm{AU}$) is possible (cooling and condensing time-scale shorter shearing) and that this could be the formation scenario for brown dwarfs observed in large orbits around Sun-like stars. This conclusion was also presented by Stamatellos et al. (2007) from the simulation of a massive ($0.5\,\mathrm{M_\odot}$) and extended disks (from 40 to $400\,\mathrm{AU}$), who also found that if released by interaction (among the objects formed in the disk), brown dwarfs would have a low velocity dispersion ($\lesssim 2\,\mathrm{km}$ $\mathrm{s^{-1}}$). Other works present brown dwarfs as objects initially accreting matter in circumstellar disks which are then ejected by gravitational instabilities due to disk–star encounters (Goodwin & Whitworth 2007) or disk–disk encounters (Watkins et al. 1998).

1.2.3 Ejection from accretion envelope

It was proposed by Reipurth (2000) and Reipurth & Clarke (2001) that brown dwarfs would be the results of protostars that would be ejected from its accretion envelope. In such scenario, brown dwarfs are first formed like stars or like planets in circumstellar disks. However, the hydrogen burning limit is not reached since the accretion is not completed, either by an encounter or by another object, or either the protosubstellar object is formed in an unstable multiple system and is ejected.

Some numerical simulations were performed and resulted in the formation of substellar

objects in such condition. Watkins et al. (1998) performed a numerical simulation of protostellar non-coplanar disk-disk encounters. From their simulation, objects as low as $0.03\,M_\odot$ were formed in massive ($0.5\,M_\odot$) and extended disk (1 000 AU). On the other hand, Bate et al. (2003, 2005) performed the hydrodynamic simulation of star formation in molecular cloud to produce a stellar cluster. They obtained that the substellar objects were formed from the molecular cloud but were ejected by dynamical interaction in unstable multiple systems. The lowest mass object they obtain was a substellar object with $0.005\,M_\odot$.

Among the observational consequences from this formation process, Reipurth & Clarke (2001) argue that the kinematics of brown dwarfs should differ from stellar objects since brown dwarf velocity would be higher than that of more massive objects (if the brown dwarfs are formed from dynamical interaction in unstable multiple systems). They point out, however, that if the velocity dispersion of stars in a cluster is high (such as in Orion or in the Pleiades), then there could be no clear distinction between stellar and substellar kinematics. This is also the conclusion of Bate et al. (2003), who present a numerical simulation of the collapse and fragmentation of a large-scale turbulent molecular cloud. From their simulations, the brown dwarfs formed have a similar velocity distribution as stellar objects (Figure 1.3).
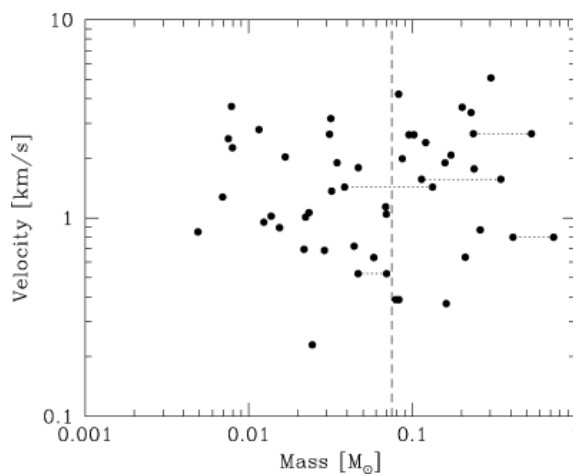
Figure 1.3 Velocities of brown dwarfs and stars produced by the numerical simulation of Bate et al. (2003). Figure from Bate et al. (2003).

However, some studies suggest instead that the ejection formation scenario would lead to a higher velocity dispersion for brown dwarfs than stellar objects. For example, with a dispersion velocity of $2\,\mathrm{km\,s^{-1}}$ for brown dwarfs (Kroupa & Bouvier 2003), there would be a larger spatial spread of the substellar population compared to the stellar population.

This could be observed as a variation between the mass function with radius on the stellar regime and the mass function at the substellar regime (Kroupa & Bouvier 2003; Luhman et al. 2007c). Considering suppositions like these, Muench et al. (2003) analyzed the mass function of the core and the halo of the open cluster IC 348 to measure the radial dependence of the stellar and substellar population. They observed a radial variation in the mass function measured over 0.5 to $0.08\,M_\odot$, but no variation for the brown dwarf regime. In a study of the spatial distribution of substellar objects in IC 348 as well as Trapezium in the Orion Nebula Cluster, Kumar & Schmeja (2007) observed stellar objects to be more clustered than substellar ones. They concluded that this observation was evidence in favour of the ejection scenario.

Considering the points mentioned above, the stellar and substellar mass function of an open cluster can be used to put constraints on the ejection scenario as a brown dwarf formation mechanism. We would conclude that the ejection scenario is the dominant process of brown dwarf formation/evolution and that they are formed with higher velocity dispersion than stars (Kroupa & Bouvier 2003), if a radial variation is observed in the mass function above the stellar–substellar limit (for masses $> 0.72\,M_\odot$), and no variation is observed below the stellar–substellar limit. However, if all brown dwarfs were formed by ejection, an absence of radial variation of the mass function on each side of the stellar–substellar boundery will be an indication that the velocity distribution of star and brown dwarf are similar (Bate et al. 2003).

1.2.4 Photoevaporation of the accretion envelope

Finally, as we have pointed out above, brown dwarfs could be formed by photoevaporation of their accretion envelopes by the radiation of a close-by massive star. From imaging of M16 using the *Hubble Space Telescope WFPC2* camera, Hester et al. (1996) observed little evidence of outflows from young stellar objects (such as winds or jets). These outflows (winds and jets) are an indication that star formation can no longer take place since they terminate infall in objects. Considering that these outflows are responsible for terminating infall in object formation and that objects in M16 are too young to have completed their formation, Hester et al. (1996) concluded that a different process is responsible for stopping the accretion in the young stellar objects of M16, such as the radiation of nearby massive stars. They also suggest that, when exposed to radiation from nearby massive stars, photoevaporation of the surroundings of the protostellar object can stop accretion and limit the objects to a lower mass than it would reach without photoevaporation. A schematic representation of the photoevaporation of the accretion envelope is given in Figure 1.4. Hester (1997) point out that if brown dwarfs were formed from interruption of accretion

by photoevaporation, isolated substellar objects should be in an area where massive stars are also found (or at least, in an area where massive stars are). Whitworth & Zinnecker (2004) analysed the formation and evolution of a protostellar core exposed to an ionization front. They concluded that photoevaporation can produce free-floating brown dwarfs and planetary-mass objects. However, it would need a massive initial core (the production of a $0.02\,\mathrm{M_\odot}$ brown dwarf would need an initial core mass of $45\,\mathrm{M_\odot}$ if surrounded by a $10\,\mathrm{pc}$ radius HII shell) and the formation process would need to have started well before the nearby massive stars began to produce their ionizing radiation.

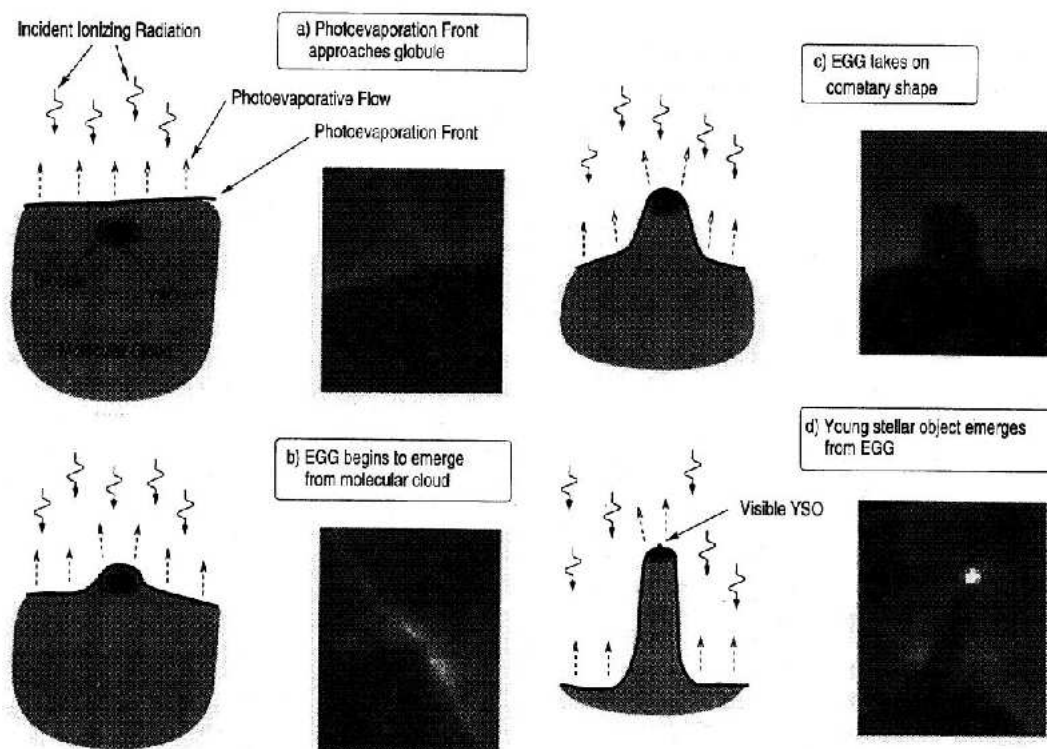Figure 1.4 Schematic representation of the photoevaporation of the accretion envelope presented by Hester et al. (1996). Figure from Hester et al. 1996.

1.3   Constraints on the formation mechanisms: survey of brown dwarfs in open clusters

Observations of these objects are an important and necessary tool to putting constraints on the various formation mechanisms of brown dwarfs. These objects can be found in the

galactic field, star formation regions, and in stellar clusters. Observing brown dwarfs is difficult. As we have seen in section 1.1, these objects have a very low luminosity when they reach an age similar to that of the Galactic disk (D'Antona & Mazzitelli 1985). If only photometry is available for an object the distance is not known, then a foreground young low-mass brown dwarf would give the same apparent magnitude and energy distribution as a background old higher-mass brown dwarf. Moreover, even with spectroscopy, estimating mass is a difficult task since the sensitivity of gravity measurement is relatively poor due to the absence of strong atomic lines with extended wings (Pavlenko et al. 2006).

Distance, age and metallicity can be fixed for an entire population of stars and brown dwarfs when looking at a stellar cluster. Stellar clusters are produced from the same material (we can assume that all members have same metallicity), are produced at the same time (same age[2]) and are formed in the same area (same distance from the Earth). Stellar clusters are therefore ideal locations to study homogeneous and coeval populations. As we have pointed out above, brown dwarfs get fainter with time, so one would look in the younger and closer open clusters (close to the Galactic disk, aged from $1\,\mathrm{Myr}$ to $1\,\mathrm{Gyr}$) rather than in aged and distant older globular clusters (situated mostly in the halo, and older then $1\,\mathrm{Gyr}$).

Work over the past ten years has seen considerable success in performing surveys of stellar and substellar populations in several open clusters, including σ Orionis (Caballero et al. 2007; Gonsález-García et al. 2006), the Orion Nebula Cluster (Slesnick et al. 2004; Hillenbrand & Carpenter 2000), Taurus (Luhman 2004, 2000a; Briceño et al. 2002), IC 2391 (Barrado y Navascués et al. 2004a), ρ Ophiuchi (Luhman & Rieke 1999) and the Pleiades (Lodieu et al. 2007; Moraux et al. 2003; Jameson et al. 2002; Hambly et al. 1999). Some surveys also brought information on the spatial distribution of substellar objects compared to stellar objects. For instance, Muench et al. (2003) observed a radial variation in the MF of IC 348 measured form 0.5 to $0.08\,\mathrm{M_\odot}$, but no variation was detected in the brown dwarf regime. In a study of the spatial distribution of substellar objects in IC 348 as well as in the Trapezium in the Orion Nebula Cluster, Kumar & Schmeja (2007) observed the stellar objects to be more clustered than the substellar ones, which they took as evidence for the ejection scenario.

Of course, one would be tempted to look for brown dwarfs in star-forming regions and very young open clusters since the advantage of studying a very young brown dwarf population is that stellar and substellar objects will be much brighter, for a fixed mass, then in older open clusters. For instance, Caballero et al. (2007) were able to perform a survey in the σ Orionis open cluster down to planetary-mass objects. However, uncertainties exist on

---

[2]Recent work has shown, however, that successive rounds of star formation might have occured in globular clusters (Piotto et al. 2007).

the evolutionary tracks of low-mass stars and brown dwarfs at very small ages (Baraffe et al. 2002) so physical determinations of these objects based on models might include large errors for studies of very young open clusters (as found by Caballero et al. 2007, Kumar & Schmeja 2007 and Muench et al. 2003). Moreover, extinction must be taken into account in surveys of very young open clusters since accretion and dissipation of material is not completed (Manzi et al. 2008). On the other hand, a survey of substellar objects in older open clusters ($\gtrsim 100\,\mathrm{Myr}$) is not an attractive option either since low-mass objects (low-mass stars and brown dwarfs) might start to evaporate from the cluster due to dynamical evolution (we will discuss this phenomenon further in §2.2) and brown dwarf also start to become fainter.

Therefore, in order to study the substellar population and to look at its spatial distribution compared to stars, one would have to chose an open cluster that is young enough to have bright objects (and not too much affected by dynamical evolution) and old enough that extinction and uncertaines regarding evolutionary tracks can be as low as possible.

1.4   Surveys of IC 2391

Among the open clusters that could be used for a radial study of stellar and substellar population, an interesting target, considering its characteristics, IC 2391. This cluster has an age of 50 Myr measured is lithium depletion (Barrado y Navascués et al. 2004a) or 40 Myr from main-sequence fitting (Platais et al. 2007). The Hipparcos distance is $146.0^{+4.8}_{-4.5}\,\mathrm{pc}$ (Robichon et al. 1999) and the metallicity and extinction are [Fe/H]$= -0.03 \pm 0.07$ and $E(B - V) = 0.01$ respectively (Randich et al. 2001). (There is a disagreement between the distance modulus obtained from main-sequence fitting from Platais et al. (2007), $V_0 - M_V = 6.01$, and the distance modulus inferred from the mean parallax via Hipparcos, $V_0 - M_V = 5.82$, by Robichon et al. (1999), but we use only the latter as the distance to IC 2391.) Such clusters in the age range of 5–50 Myr, also identified as pre-main sequence clusters, are very good tools for studying formation and evolution of the stellar and substellar populations. Indeed, they are old enough that observations of low-mass objects are less affected by extinction (since most of material from the original molecular cloud was accreted and dissipated) and that error on evolutionary models for low-mass stars and brown dwarfs are not as high as for very young objects at ages $\lesssim 1\,\mathrm{Myr}$ (Baraffe et al. 2002). On the other hand, IC 2391 is young enough that brown dwarfs and low-mass stars are still bright enough for an optical survey using reasonable amount of telescope time.

Since IC 2391 is not as young as IC 348 (age $\sim 2\,\mathrm{Myr}$ from Muench et al. 2003) or the Trapezium (age $\sim 0.8\,\mathrm{Myr}$ from Muench et al. 2002), one might expect that it has already

lost a significant fraction of its substellar population to evaporation by dynamical evolution. This can be verified with the crossing time and the relaxation time. Piskunov et al. (2007) estimated the tidal radius and mass of IC 2391 as 7.4 pc and 175 $M_\odot$ respectively. This is compared to other nearby (<1 kPc) open clusters, such as Praesepe (5.3 pc and 600 $M_\odot$, Adams et al. 2002b), Blanco 1 (20.0 pc and 3000 $M_\odot$, Piskunov et al. 2007), NGC 2547 (3.2 pc and 450 $M_\odot$, Jeffries et al. 2004), Pismis (6.9 pc and 120 $M_\odot$, Piskunov et al. 2007), NGC 2264 (15.0 pc and 1072 $M_\odot$, Piskunov et al. 2007), the Pleiades (20.5 pc and 3105 $M_\odot$, Piskunov et al. 2007) and IC 4665 (7.1 pc and 140 $M_\odot$, Piskunov et al. 2007). Using the tidal radius and mass of IC 2391 as estimated by Piskunov et al. (2007), we computed the escape velocity as $v_e =$ 0.4 km/s and the crossing time as $t_{cross} =$ 17 Myr. Assuming a minimum value for the number of cluster members from the number of objects reported by Dodd (2004) and Barrado y Navascués et al. (2004a) (125 and 33 respectively, together a total lower limit for 158 objects), we estimate that the lower limit of the relaxation time for this cluster is $t_{relax} \sim$ 105 Myr. Therefore, IC 2391 is still young enough for a radial study of its very low-mass star and brown dwarf population since evaporation by dynamical evolution should not play a significant role in the shape and variation of the mass function (as it does for the $\sim$625 Myr old open clusters Hyades, as reported by Bouvier et al. 2008). Considering the fact that mass segregation occurs on a timescale of the order of one relaxation time (Bonnell & Davies 1998), we can expect that any radial variation of the substellar population would be due to initial conditions. Moreover, since the velocity dispersion of brown dwarfs formed via ejection ($\sim$2 km/s, Kroupa & Bouvier 2003) would be five times that of the escape velocity of IC 2391 (0.4 km/s), one would expect to see a discontinuity in the mass function when crossing the substellar boundary if *all* brown dwarfs had formed via the ejection scenario *and* formed with a higher velocity dispersion than stars.

IC 2391 was first reported in the *Second Index Catalogue of Nebulae and Cluster of Stars* (Dreyer 1895). Since then, because of its proximity and youth, this cluster has been subject of several studies. Photometric and proper-motion surveys already reported low reddening towards the cluster and its small distance from the Earth ($E(B - V) \sim 0.00$ and distance $\sim$ 150 pc, both from Hogg 1960 and Perry & Hill 1969). Later, McNamara & Ianna (1986) performed a proper-motion survey of the low-mass star population (mass range from 0.4 to 0.7 $M_\odot$). They concluded that dynamical evaporation was responsible for the reduced population in this mass range. Other proper-motion surveys performed were too shallow to detect very low-mass stars or brown dwarfs in IC 2391 ($12 < V < 16$, Stauffer et al. 1989).

Other surveys were also performed at shorter wavelengths. Considering that in the pre-main sequence phase a star's angular momentum is dominated by gravitational contraction and interaction with its circumstellar disk, coronal activities are expected in stellar objects

of this age. Therefore, it is expected that objects that belong to pre-main sequence clusters (within an age range of 5–50 Myr, such as IC 2391) should be detected by their coronal X-ray emission (Patten & Simons 1996). An X-ray survey of IC 2391 was performed with the *ROSAT* spacecraft using its *Position Sensitive Proportional Counter* and *High Resolution Imager* (Simon & Patten 1998; Patten & Simons 1993, 1996). However, an X-ray survey might not be efficient in detecting very low-mass stars and brown dwarfs in IC 2391 since (1) objects with mass $< 0.3 \, M_\odot$ are dominated by small-scale turbulent dynamos compared to large-scale zone dynamos in higher-mass stars and (2) late-type members of young open clusters have a maximum emission flux of $\log{(L_X/L_{BOL})} = \text{-}3.0$ (Patten & Pavlovsky 1999). Considering that the bolometric magnitude at the lithium depletion boundary for IC 2391, which is at $0.12 \, M_\odot$, is $M_{BOL} = 10.24$, this would be equivalent to a bolometric luminosity of $L_{BOL} = 2.4 \times 10^{31} \, \mathrm{ergs \, s^{-1}}$ (Barrado y Navascués et al. 2004a). This corresponds to $L_X \sim 2.4 \times 10^{28} \, \mathrm{ergs \, s^{-1}}$ for late-type members of young open clusters, which is below than the 3σ detection level of $L_X \sim 4 \times 10^{28} \, \mathrm{ergs \, s^{-1}}$ from Simon & Patten (1998). Optical survey have followed (Rolleston & Byrne 1997; Patten & Pavlovsky 1999) but none reach the lithium depletion boundary of $Ic \sim 16.1$ (Barrado y Navascués et al. 2004a). The faintest candidate in Patten & Pavlovsky (1999) is at $Ic = 15.93$. Based on the NextGen model of Hauschildt et al. (1999a) and the evolutionary track of Baraffe et al. (1998), this should be an object of mass $\sim 0.1 \, M_\odot$.

The substellar limit was reached by the study of the low-mass stars and brown dwarf population of IC 2391 presented by Barrado y Navascués et al. (2001a). Although the survey presented is not homogeneous (optical photometry was collected from different observatories with different exposure times and magnitude limits for the various fields observed), they reach a maximum completeness limit of $Ic \sim 20$ mag. Since the list of cluster candidates was now approaching the low-mass end of the stellar population, work was also performed in order to obtain the lithium abundances of IC 2391 members (Barrado y Navascués et al. 1999; Randich et al. 2001). A mass function of IC 2391 down to the lithium depletion limit was presented by Dodd (2004), for a mass range from 0.1 to $1.0 \, M_\odot$, while in Barrado y Navascués et al. (2004a) the mass function goes down to $0.03 \, M_\odot$, although their completeness is at $\sim 0.072 \, M_\odot$ (which is the stellar to substellar boundary). These two mass functions are presented in Figure 1.5.

Further work was subsequently done on this cluster (Marino et al. 2005, Stütz et al. 2006, Koen & Ishihara 2006, Siegler et al. 2007 and Platais et al. 2007), but none of these studies aimed to characterise the substellar population of IC 2391. Therefore, so far, no radial study of the low-mass star population (in the mass range from 0.072 to $1.0 \, M_\odot$) and substellar population (mass below $0.072 \, M_\odot$) has been performed for this cluster. Moreover, no survey or mass function determination of IC 2391 has been performed with
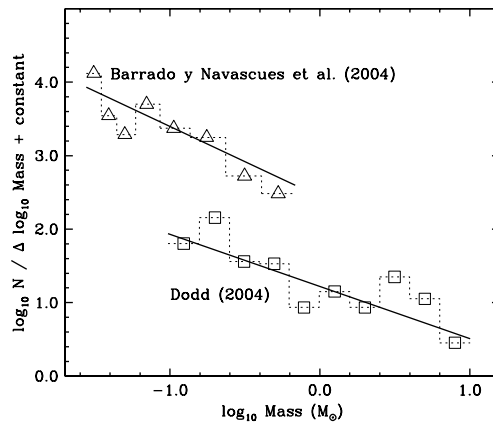
Figure 1.5 Mass functions for the open cluster IC 2391 presented by Barrado y Navascués et al. (2004a) (*empty triangles*) and from Dodd (2004) (*empty squares*). We also present the power law fit of the form $\xi(M) \sim M^{\alpha}$, were $\alpha = $ -0.96 for the mass function from Barrado y Navascués et al. (2004a) and $\alpha = $ -0.71 from Dodd (2004).

a completeness limit in the brown dwarf regime.

1.5 Outline of this work

Here we propose to obtain the mass function of the open cluster IC 2391, down to the substellar limit, and to look for any radial variation between the stellar and substellar populations. This will allow us to put constraints on possible brown dwarf formation scenarios, especially formation via ejection of proto-brown dwarfs from their accretion envelopes. We will also compare the mass function computed with mass functions of other open clusters from the literature, to see whether there is any dependence of the brown dwarf mass function with age or with environment.

The thesis presented here will be structured as follows. First, in Chapter 2, we will present the physical concepts used in our analysis, including the determination of the mass function of a population and the different functions used to represent it, a brief introduction to stellar cluster dynamics and the atmosphere and evolutionary track used to estimate the mass and effective temperature of brown dwarfs and low-mass stars. In Chapter 3, we present the data we have obtained from our survey of IC 2391 and the reduction process performed. We will also present in that chapter the method used to estimate the mass and the effective temperature. The procedure for determining membership based on photometry and spectroscopy will be presented in Chapter 4. Next, we present and discuss in

Chapter 5 the photometric and spectroscopic results of our survey of IC 2391, followed by the comparisons of the mass function of IC 2391 with those of other open clusters, in order to look for variations with age and environment (Chapter 6). Finally, we will present our main conclusions and discussion of possible brown dwarf formation scenarios based on our survey of IC 2391 and the mass functions of other open clusters in Chapter 7.

Chapter 2

Physical concepts used in the analysis

We have shown in the previous chapter that there is no current agreement on a unique formation process of brown dwarfs (different formation scenarios and observational signature were presented). In this chapter, we focus on the use of the mass function, spatial distribution, and kinematics, in order to verify the formation of brown dwarfs via the ejection scenario.

In order to study the stellar and substellar population of IC 2391, we use optical/infrared photometry and optical spectra. We therefore need an appropriate modeling of the emerging flux from these objects in order to estimate their physical properties such as their effective temperatures and their masses. Since all objects reside in a single stellar cluster, we can assume that (1) the population has the same chemical composition (i.e. same metallicity) and (2) has the same age. However, these systems dynamically evolve over time resulting in mass segregation of the system and evaporation of low-mass objects. As we will show below, these effects have consequences on the shape of the mass function.

In this chapter, we present a general introduction to cluster evolution and modeling of brown dwarf atmospheres and evolution. We first present the determination of the mass function of a population. We next present how stellar clusters evolve and how this dynamical evolution influences the spatial distribution and mass function of the stellar and substellar cluster populations. Finally, we present the atmosphere model and the evolutionary track that we used to obtain the effective temperature and masses of the stellar and substellar population.

2.1 Mass function determination of a population

The mass function of a stellar population, $\xi(\log_{10}M)$, is generally defined as the number of stars per cubic parsec (pc^3) in the logarithmic mass interval $\log_{10}M$ to $\log_{10}M + d\log_{10}M$. (The term *initial* mass function will rather define the mass function of a system when it is formed.) This tool is used to study a system population as a whole (e.g. stellar cluster or galactic thin disk population), from massive stars to low-mass brown dwarfs. It can be used to obtain the total mass of such systems, the surface brightness, the chemical enrichment, and to observe system evolution (Chabrier 2003).

Salpeter (1955) first used the mass function to study the main-sequence solar-neighborhood stellar population. Salpeter (1955) observed that the mass function could be well approximated by a power law function,

$$\xi(M) \approx 0.03 \left(\frac{M}{M_\odot} \right)^{-1.35}, \tag{2.1}$$

where the choice of this function was based on the fact that it was a reasonably well approximation between $\log_{10}M=-0.4$ to $+1.0$ (Salpeter 1955). Other functions were used to represent the general shape of the mass function, including a combination of three power laws (above $0.5\,M_\odot$, from $0.08\,M_\odot$ to $0.5\,M_\odot$, and below $0.08\,M_\odot$, Kroupa 2001) of a generalized Rosin-Rammler function,

$$\xi(\log M) \approx A\,M^{-x} \exp\left[-\left(\frac{B}{M} \right)^{\beta} \right], \beta < 0, \tag{2.2}$$

where x, A, B and β are constants. Another representation of the mass function is given by a lognormal (or Gaussian) function, such as presented by Miller & Scalo (1979),

$$\xi(\log M) = k \exp\left[-\frac{(\log M - \log M_0^2)}{2\sigma^2} \right], \tag{2.3}$$

where M_0 and σ^2 represent, respectively, the mean mass (or also known as the characteristic mass) and the variance of the mass distribution in $\log M$ and k is a normalization constant. Again, this function was used by Miller & Scalo (1979) not on a physical basis but because the best fit for their determination of the initial mass function of the solar neighborhood was a parabola of $\log_{10}\xi(\log_{10}M)$, and thus a Gaussian function for $\xi(\log_{10}M)$. Such shape of the mass function subsequently was observed and used for the analysis of stellar populations

(Chabrier 2003; Deacon & Hambl 2004; Jeffries et al. 2004; Bouvier et al. 2008). This lognormal function was also the best fit for stellar cluster population formed from molecular clouds, as shown in numerical simulation by Padoan & Nordlund (2004), Bate et al. (2005) and Clark et al. (2008). The simple power law function is valid for populations with masses higher then $1\,M_\odot$ (Chabrier 2003). However, our study covers a mass range from brown dwarfs to low-mass stars (as we will see in Chapter 5, up to $0.9\,M_\odot$). Therefore, we will use a lognormal function such as the one presented in eq. 2.2 in this work.

It is important to point out here that the mass functions presented in this work are all system mass functions since there is no corrections done for binarity. (For a discussion on the observed modifications on the mass function by taking into account binarity, please see Kroupa 2001 and Thies & Kroupa 2007.)

The dependance of the initial mass function on environmental factors, such as the density and temperature of the molecular gas where the stellar objects were formed, was obtained from numerical simulations (Klessen & Burkert 2001; Kroupa 2001; Bate et al. 2005; Clark et al. 2008). Variation in the mass function with the environment has also been shown via observational evidence. For instance, Briceño et al. (2002) observed two times fewer brown dwarf in the mass range 0.02–$0.08 M_\odot$ than in the Trapezium Cluster (mass function for these two clusters presented in Figure 2.1, left). They attributed this situation to the fact that, since Taurus is embedded in a molecular cloud (star forming region) with a lower density then for the Trapezium Cluster, the minimum Jean mass would be larger. Furthermore, the mass function of a population, such as an open cluster, has a dependance with age. Indeed, numerical simulations of cluster evolution have demonstrated mass function evolution through dynamical interaction (de la Fuente Marcos & de La Fuente Marcos 2000; Adams et al. 2002a). These interactions result in a diminution of the open cluster brown dwarf (and also low mass object) population. This was also observed by Bouvier et al. (2008) with the mass function of the Pleiades ($\sim$120 Myr) and of the Hyades ($\sim$625 Myr). We present the mass functions for these two clusters in Figure 2.1 (right).

2.2 Dynamical evolution of stellar clusters

Open stellar clusters are formed from large unstable molecular clouds. Since the formation of all objects in a single cluster results from the collapse of the same molecular cloud, we can assume that the population formed is homogeneous (i.e. has the same metallicity and the same age). However, these systems evolve in time, by dynamical interaction with own cluster members, interaction with other clusters and molecular gas, and tidal forces from the galactic plane. Two effects from dynamical evolution influence the spatial distributions
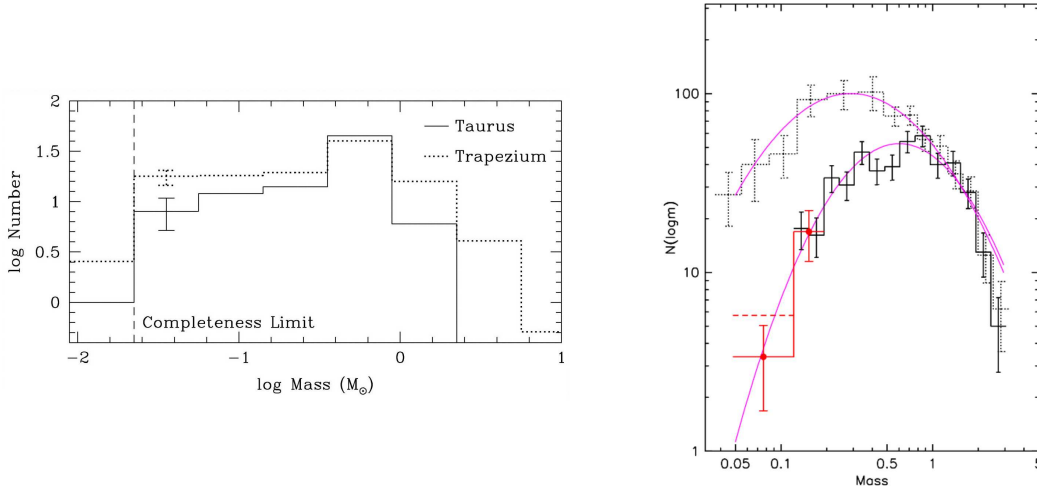
Figure 2.1 *Left.* Mass function from the Trapezium and Taurus open clusters; Figure from Briceño et al. (2002). *Right.* Mass function from the Hyades and the Pleiades open clusters; Figure from Bouvier et al. (2008)

of the stellar members and the mass function of the system : dynamical mass segregation and dynamical evaporation of lower mass members. (Stellar evolution also influences the shape of the mass function. However, we assume that it does not affect it in the mass range of interest for open cluster younger than 1 Gyr.)

The Dynamical mass segregation is the process where massive stars tend to move toward the cluster center while lighter objects move away from the cluster center. Through encounters with lower mass objects, more massive objects loose kinetic energy and sink toward the center of the cluster. This occures until uniform thermal velocity distribution (equipartition of energy) is achieved. This is observed in old and dense globular cluster (Elson et al. 1987), but also in younger and less massive open clusters. (Schilbach et al. 2006 observed clear evidence for mass segregation for stars with masses $> 1 \, M_\odot$ for the majority of the 600 open clusters in their sample, which covered an age range from 5 Myr to more then 1 Gyr.) This segregation is reflected by a higher population of massive stars in the mass function of the central part of a cluster compared to the halo mass function.

Mass segregation can also be due to the initial conditions of the cluster. Indeed, it is possible that star formation is not uniform in a molecular cloud : due to higher gas density, star formation near the center would have a higher accretion rate, resulting in the formation of more massive stars (Sirianni et al. 2002). This is also defined as primordial mass segregation. Sirianni et al. (2002) observed mass segregation in NGC 330 (age∼30 Myr) and concluded it was of a primordial nature rather than from dynamical evolution. Their

conclusion was based on the fact that NGC 330 is 10 time younger than its relaxation time. Primordial mass segregation has also been reported for other open clusters (SL 666, Kontizas et al. 1998; NGC 2157, Fischer et al. 1998; NGC 6231, Raboud & Mermilliod 1998).

Another consequence of cluster dynamical evolution is that the rise of kinetic energy of lower mass objects leads to a rise in their velocity. The velocity of some low-mass members can be greater than the escape velocity of the cluster, resulting in these members being lost from the cluster. This process, also known as dynamical evaporation, has been demonstrated in numerical simulations (Adams et al. 2002a; de la Fuente Marcos & de La Fuente Marcos 2000). Evaporation of low-mass stars and brown dwarfs has also been observed in the Hyades (625 Myr, Bouvier et al. 2008). Bouvier et al. (2008) have estimated that, based on the differences in mass function between the Pleiades and the Hyades, the Hyades which currently host 10–15 brown dwarfs, could have originally had 150–200 substellar members. The effect of dynamical evaporation is observed on the mass function as a diminution of the low-mass population (stellar and substellar) with time. This is shown in comparisons between the Hyades and Pleiades mass functions (see Figure 2.1, right, from (Bouvier et al. 2008)). It has also been shown in N-body simulations of clusters in tidal fields (Baumgardt & Makino 2003).

Evaporation of the low-mass members of the cluster doesn't occur only because of interactions among the stellar and substellar objects, but also by tidal stripping from the Galactic gravitational field, as mentioned above. Furthermore, the loss of gas, which reduce the binding energy of the cluster, will also be responsible for the evaporation of the low-mass members.

Therefore, in order to study the spatial distribution of the low-mass stars and brown dwarfs in an open cluster, one would need to study young clusters in order to avoid effects due to dynamical evolution (such as mass segregation and evaporation of low-mass stars and brown dwarfs). As we have seen in the previous chapter, such studies have been performed on young open clusters such as IC 348 (by Muench et al. 2003 and Kumar & Schmeja 2007; age ~ 2 Myr from Muench et al. 2003), the Orion Trapezium Cluster (by Kumar & Schmeja 2007; age ~ 0.8 Myr from Muench et al. 2002) and σ Orionis (by Caballero 2008; age ~ 3 Myr from Caballero et al. 2007). Since IC 2391 is not as young as those clusters, one may expect it has already lost a significant fraction of its substellar population from evaporation by dynamical evolution.

We can estimate how much IC 2391 has been affected by evaporation and dynamical evolution by considering the crossing time and relaxation time respectively. Using the tidal radius and mass of IC 2391 estimated by Piskunov et al. (2007) (7.4 pc and 175 $M_\odot$),

we first compute the escape velocity of the cluster using the following equation, and the fact that this velocity is obtained when the kinetic energy is higher than the cluster gravitational potentiel,

$$\frac{1}{2} m \, v_e + \frac{-G \, M \, m}{r} = 0 \Rightarrow v_e = \sqrt{\frac{2 \, G \, M}{R}}, \qquad (2.4)$$

where G is the gravitational constant, M the mass of the cluster and R is the tidial radius. (The tidal radius is defined as the distance from cluster center at which gravitational potential of the cluster equals the gravitational potential of the galactic field.) For IC 2391 we obtain an ejection velocity of v_e =0.4 km/s. The crossing time of the cluster, t_{cross}, is given by the ratio of the tidal radius and the escape velocity v_e. For IC 2391, we estimate t_{cross} =17 Myr. Considering the age of IC 2391 ($\sim$50 Myr), this would mean that more then 95% of the brown dwarf population is still contained within the cluster (Adams et al. 2002a).

Considering the fact that mass segregation, which is the time needed to reach energy equipartition, occurs on a timescale of the order of one relaxation time (Bonnell & Davies 1998), it is possible to estimate if any radial variation of the substallar population in IC 2391 would be due to initial conditions or by dynamical mass segregation. An approximation of the relaxation time t_{relax} can be given by the following equation,

$$t_{relax} \sim t_{cross} \frac{N}{8 \, ln(N/2)}, \qquad (2.5)$$

where N is the number of cluster members. Assuming a minimum value for the number of cluster members as the objects reported by Dodd (2004) and Barrado y Navascués et al. (2004a) (125 and 33 respectively, together a total lower limit of 158 objects), we estimate that the lower limit of the relaxation time for this cluster is t_{relax} $\sim$105 Myr. Therefore, IC 2391 is still young enough for a radial study of its very low-mass star and brown dwarf population.

2.3   Atmosphere model and evolutionary track used

The goal of an atmosphere model is to quantify thermodynamic conditions as a function of optical depth in a stellar atmosphere. The atmosphere structure is obtained by solving the fundamental equations of stellar physics. These equations describe the temperature,

pressure, electric density, specific density and chemical population as a function of optical depth, for a given effective temperature T_{eff}, surface gravity log g, and chemical composition. When the thermodynamic structure has been determined, we can obtain, by solving the equation of radiative transfer, the emerging flux H_ν, also known as the Eddington flux and presented as the synthetic spectrum of the atmosphere.

Calculations of atmosphere models take into account important molecular absorbers observed in M–dwarfs, such as H_2O, TiO, CN and CO. However, as the effective temperature goes down with lower masses, grain formation occurs, and therefore needs to be taken into account in the calculation of opacities and the equations of state. Such grains, like ZrO_2 which appears at gas temperatures of 2000 K, corundum (Al_2O_3) at 1 800 K and iron, VO, and enstatite ($MgSiO_3$) at 1600 K, affect the spectral distribution of M–dwarfs and brown dwarfs (Allard et al. 1997). As the atmosphere gets even colder, grains settle down by gravity and fall below the photosphere. We can therefore treat the atmosphere of low-mass stars and brown dwarfs in three different ways, depending on their effective temperatures.
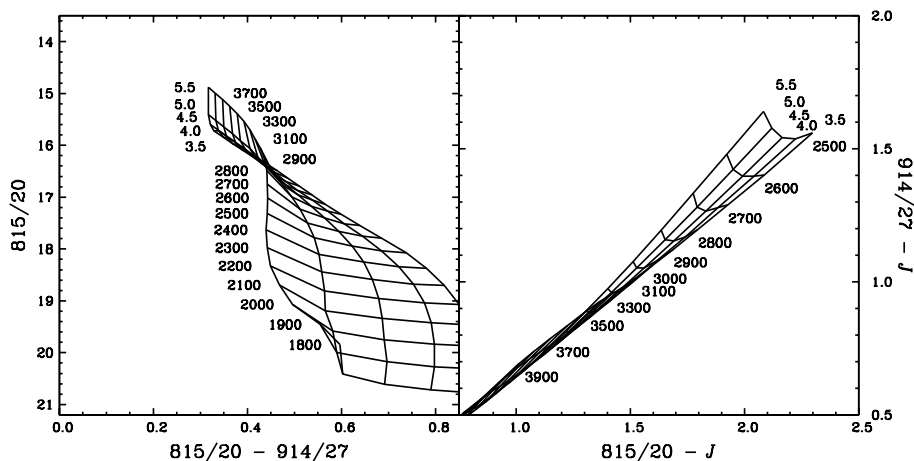
Figure 2.2 Color-magnitude and colour-colour diagram showing a grid of magnitudes and colours for several filters. Each point in the grid represents a unique value of log g and T_{eff}. (These filters correspond to some filters used in our study.) We give values of log g and T_{eff} for each grid level. However, for clarity, not all T_{eff} values are shown.

Objects with $T_{eff} \geqslant 3000$ K have grainless atmospheres. Such atmospheres have been modeled by Hauschildt et al. (1999a) and are presented with the **NextGen** model. Objects with 3000 K $\geqslant T_{eff} \geqslant 1800$ K have dust in equilibrium with the gas phase. Modeling of such atmospheres is presented by Allard et al. (2001) and is identified as the **AMES-dusty** model. Atmospheres where dust has disappeared because of gravitational settling

is described by the atmosphere model **AMES-cond** (Allard et al. 2001). This applies best for objects with $T_{\rm eff} \leqslant 1300\,{\rm K}$.
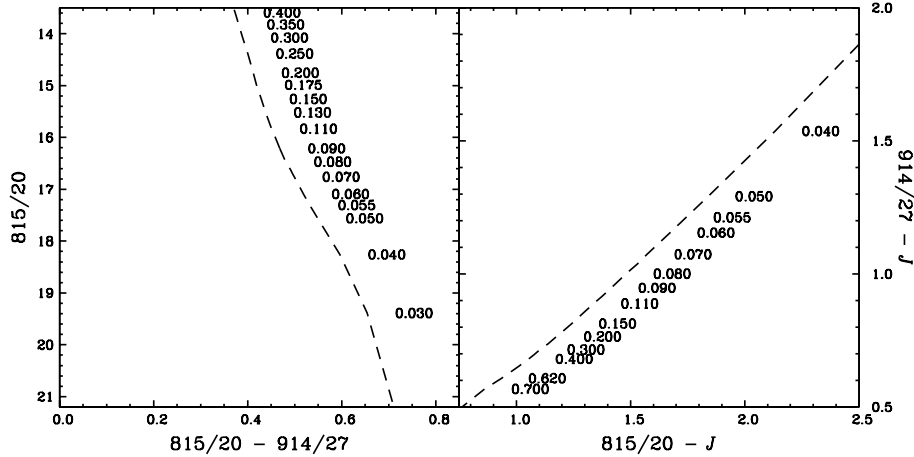
Figure 2.3 Color-magnitude and colour-colour diagram showing the isochrones of the open cluster IC 2391 for the same filters presented in Figure 2.2. The masses corresponding to the isochrones are shown and are shifted horizontally for clarity.

Considering that the coolest object in our sample presents a $T_{\rm eff} \gtrsim 2500\,{\rm K}$ and that we prefer to use a unique model to avoid discontinuity in the selection procedure and mass determination, we use only the NextGen models for our analysis. From these models, we have synthetic spectra H_λ for values of $\log g$ from 3.5 to 5.5 with steps of 0.5, and for values of $T_{\rm eff}$ from 1700 K to 4000 K by steps of 100 K, and from 4000 K to 9800 K by steps of 200 K. We use a metallicity of [M/H]=0.0 (solar metallicity) for our analysis. The grid of $T_{\rm eff}$ and $\log g$ is represented in a color-magnitude and a color-color diagram in Figure 2.2.

As we have shown in the previous chapter, brown dwarfs are objects that are not massive enough to maintain hydrogen-burning in their cores. These objects therefore cool down as they evolve in time. In addition, for young objects (age $\lesssim 100\,{\rm Myr}$), including very low-mass stars, effective temperature and radius change as they start to reach the main sequence. Therefore, it is imperative to appropriately model the evolution of objects with time in order to know their effective temperature and radius for a given mass at a given age. Moreover, the atmosphere assumed for a given object can influence its expected evolution (Chabrier et al. 2000; Baraffe et al. 2002). Evolution of the effective temperature as a function of time for NextGen, AMES-dusty and AMES-cond is presented in Figure 2.4.

Using evolutionary tracks, for a grainless atmosphere by Baraffe et al. (1998, 2002), and the NextGen atmosphere model of Hauschildt et al. (1999a), we can now compute an isochrone
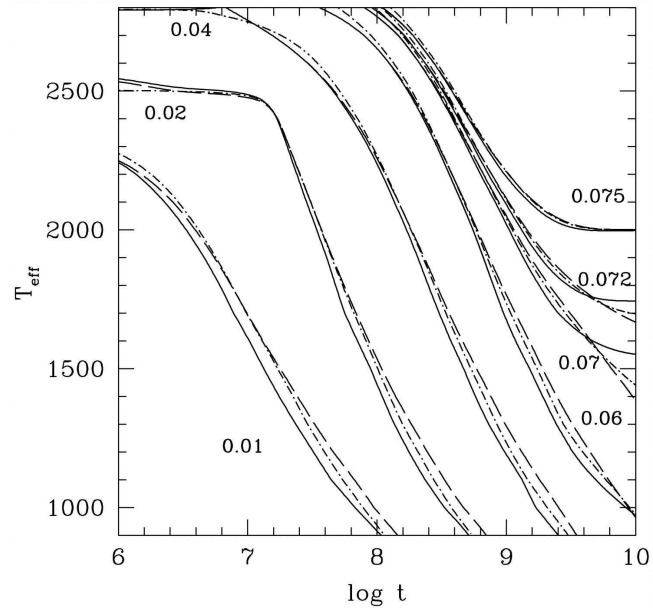
Figure 2.4 Evolution of the effective temperature T_{eff} with time (in log yr) for each atmosphere models discussed and for different masses (in $M_\odot$). Solid lines are from AMES-dusty, long-dashed lines are from AMES-cond, and dash-dotted lines are from NextGen models. Figure from Chabrier et al. (2000).

for a stellar population such as the open cluster IC 2391 with its known age (50 ± 5 Myr, Barrado y Navascués et al. 2004a), its distance (146 ± 5 pc, Robichon et al. 1999) and its solar metallicity ([Fe/H]=-0.03, Randich et al. 2001). Using the same filters as the color-magnitude and color-color diagrams of Figure 2.2, we present the isochrones of IC 2391 in Figure 2.3. This isochrone will be used to identify members of this open cluster based on photometry. It will also be used to estimate physical parameters of these members, such as their effective temperature and their mass. The isochrones effective temperature range goes from 1904 K to 6626 K. and his mass range goes from 0.02 to 0.1 $M_\odot$ by step of 0.01 $M_\odot$ (including 0.055, 0.072 and 0.075 $M_\odot$), from 0.1 to 0.95 $M_\odot$ by step of 0.05 $M_\odot$ (including 0.11, 0.13, 0.175, 0.57 and 0.62 $M_\odot$ but excluding 0.55 and 0.65 $M_\odot$), and finally from 1.0 to 1.4 $M_\odot$ (including 1.05 and 1.15 $M_\odot$).

We have defined the atmosphere models and evolutionary tracks used to obtain correct isochrones for open cluster. This will allows us to extract the physical properties of stars and brown dwarfs. In the next chapter we present the photometry and spectroscopy used in our project as well as the data reduction processes.

Chapter 3

Observations, data reduction and mass estimations

In the previous chapters, we have shown that in order to put constraints on the brown dwarf formation scenario by ejection of the protostar from its accretion envelope, we can study the radial variation of the stellar and substellar mass function of the young open cluster IC 2391. To obtain the mass function of those two populations, we need to perform a photometric survey. From the isochrone presented in §2.3, we have concluded that such a survey should cover the energy distribution of stars and brown dwarfs from $\sim$650 nm to $\sim$1.2 μm. However, in addition to the photometric data, we will need to obtain optical spectroscopy in order to know if objects detected, assumed to be members based on photometry, are indeed members of IC 2391. In addition to membership determination, spectroscopic follow-up gives us additional information that cannot be determined with photometry, such as radial velocity and spectral type. However, in both cases the data obtained at the telescope can't be used immediately: one needs to perform *data reduction*, the process in which we take the original images from the telescope and obtain data which can be used for analysis. It is the goal of this chapter to present now the data were obtained and how the data reduction was performed.

First, we will present the instrument and telescope used, including the filter used for photometry and the setup of the spectrograph used for the spectroscopic follow-up. We will continue with the presentation of the data reduction procedure for our photometric data, including the calibration performed. In the next section, we will present the data reduction and calibration performed on our spectroscopic data. The end of this chapter will be used to present how the effective temperature and masses were computed based on photometry and on spectroscopy (which include the spectral type determination for the latter).

3.1   Photometric and spectroscopic data available

3.1.1   Choice of fields, instruments and filters for photometric observations and data obtained

With the goal of studying the behaviour of the stellar and substellar population of IC 2391, we needed to observe a large area of the cluster. The tidal radius was estimated to be 7.4 pc which, assuming a distance of 146 pc, corresponds to an angular distance of 2.9° from cluster centre, which is at RA=08:40:36 DEC=-53:02:00 (FK5 coordinates, epoch J2000.0). This implies that we need to cover an area of several square degrees. This is accomplished with our survey which consists of thirty-five 34×33 arcmin fields extending to 3° from the centre of the cluster (Figure 3.1). The fields were chosen to extend preferentially along lines of constant galactic latitude – the cluster is centred at l=270.4° b=-6.9° – in an attempt to reduce systematic errors in any established cluster mass function gradient which could arise from contamination by a Galactic disk population gradient. The total coverage of our survey is 10.9 square degrees. This compares to 2.5 deg^2 in the survey of Barrado y Navascués et al. (2001a).

In Figure 3.2 we present the synthetic spectra using the NextGen atmosphere model of three objects with effective temperatures of 4200 K, 3000 K and 1700 K (all assuming log $g = 4.5$ and solar metallicity). From this we can observe that the red part of the optical region of the energy distribution (at ~600 nm, with a R band filter) to the near-infrared (at ~1.2 μm, with a J band filter) would be a good region to cover in order to easily identify cool (and low-mass) objects from background–foreground hotter contaminant. We can also observe that the use of near-infrared filters alone, such as J, H (at ~1.65 μm) or K_s (at ~2.15 μm) would be insufficient to make a distinction between cooler and hotter objects.

The optical observations were carried out in four runs with the Wide Field Imager (WFI) on the MPG 2.2m telescope at La Silla (Baade et al. 1999) on 24 January - 9 February 1999, 20 - 24 January 2000, 10 - 23 March 2007 and 15 - 18 May 2007. The WFI is a mosaic camera comprising 4×2 CCDs each with 2k×4k pixels delivering a total field of view of 34×33 arcmin at 0.238 arcsec per pixel. The optical filters used for our survey are the broad band R_c and the four medium bands 770/19, 815/20, 856/14 and 914/27 (where the filter name notation is central wavelength on the full width at half maximum, FWHM, in nm). In addition to the broad band R_c, we also used medium band filters to better sample the energy distribution over R_c and I_c. Due to time available at the telescope and weather constraints, it was not possible to obtain a homogeneous data set. Therefore, the fields presented in Figure 3.1 will be separated and analysed in three different groups: the
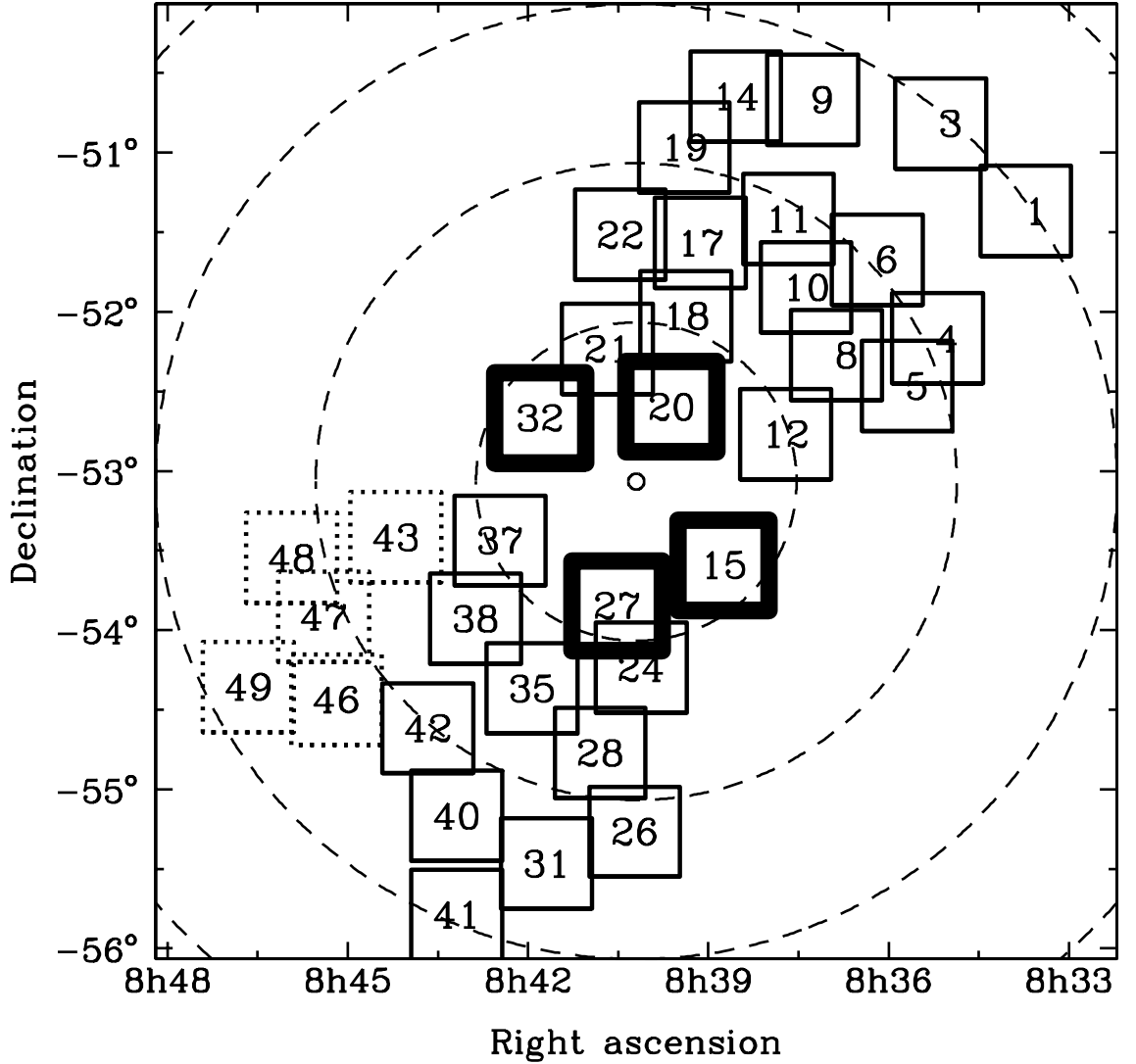
Figure 3.1 Area covered by our survey of IC 2391. The four thick squares are the deep fields, the dotted squares are the outward fields and the others are the radial fields. The circles have radii of 1°, 2° and 3° from the cluster center.

deep fields, the *outward* fields and the *radial* fields.

The deep fields in our survey were observed in four medium band filters, namely 770/19, 815/20, 856/14 and 914/27 and one broad band filter, R_c. The radial fields were observed in R_c, 815/20 and 914/27 while the outward fields were not observed in R_c, but rather only with 815/20 and 914/27. The pass band function for all filters is shown in Figure 3.3. The choice of these medium bands was made in order to minimize the Earth-sky background (see Figure 3.4 for passband function of the optical filter used and Earth-sky background)

plus any nebular emission. For all radial fields, we have used exposure times of 15, 10 and 25 minutes for the 815/20, 914/27 and R_c filters respectively. For each deep field we obtained an integration time of 65 minutes for each of the 770/19 and R_c filters and 135, 160 and 65 minutes for the 815/20, 856/14 and 914/27 filters respectively. We additionally obtained short exposures for all fields to extend the dynamic range to brighter objects.

In order to improve the determination of the low-mass status (via a better determination of spectral type and luminosity), we also observed all radial and outward fields in the J band using the *Caméra PAnoramique Proche-InfraRouge* (CPAPIR) on the 1.5 m telescope at Cerro Tololo, Chile (runs on 28 February - 3 March 2007 and 10 March 2007). CPAPIR consists of one Hawaii II detector with 2k×2k pixels for a field of view of 35×35 arcmin with a pixel scale of 1.03 arcsec per pixel. All fields were observed with a total exposure time of 30 minutes. The J filter of CPAPIR is centred at 1250 nm with a FWHM of 160 nm.

A detailed list of the fields observed with pointing, filter used, exposure time and 10σ detection limit, is given in Table 3.1 at the end of this chapter. The passband function of all filters used is also presented in Figure 3.3.

3.1.2 Choice of instrument for spectroscopic follow-up and data obtained

Since we have many objects in the same area of the sky for which we need to perform a spectroscopic follow-up, a multi-object spectrograph capability over a large field-of-view is essential. The spectroscopic observations were carried out with HYDRA, a multi-object, fiber-fed spectrograph on the 4m telescope at Cerro Tololo on the nights of 6 and 7 January 2007. We used the red fiber cable with the KPGLF grating (632 lines mm^{-1}) and a blaze angle of 14.7° (no blocking filter was used). This gives us coverage of 6429–8760 Å centred at 7593 Å and a spectral dispersion of 1.14 Å delivering a spectral resolution of 5757 Å at Hα. Since the number of fibers available with HYDRA is higher than the number of candidates per pointing, the remaining fibers were allocated for *non-photometric* member candidates. Moreover, fibre overlap is not possible with this instrument, thus not all candidates in a field could be observed.

We have obtained a total of 70 spectra in field 15 (35 for which the SNR is higher than 5) and 50 from field 20 (42 with a SNR higher than 5). Spectra with a SNR below 5 are not used in our analysis. At the end of this chapter we present in Figures 3.8 and 3.9 the spectra used for our analysis from fields 15 and 20 respectively. In Table 5.3, we provide the corresponding coordinates, signal-to-noise ratio (SNR) and observed magnitude in the medium band 815/20. Objects are given the notation IC 2391-HYDRA-ZZ-YY where ZZ

is the field number and YY a serial identification number (ID).

3.2 Photometric data reduction procedure

In this section we will discuss in detail the reduction steps (from raw images to calibrated photometry). The major steps are as follows. First, we subtract the overscan, bias and darks followed by the trimming of the images. Then, images are flat-fielded in order to correct pixel-to-pixel variation of the CCD and the non-uniform illumination of the detector. For WFI data, we reduced each of the 8 CCDs in the mosaic independently and in the final step scaled them to a common flux response level. Afterward, sky is subtracted and, in the case of medium band photometry, fringes are subtracted. The individual images of a given field were then registered and median combined. Following this step, detection of objects and aperture photometry were performed. Finally, the coordinates of each sources were obtained and were flux calibrated.

All data reduction steps were performed with IRAF (*Image Reduction and Analysis Facility*), a general purpose software system for the reduction and analysis of astronomical data.

3.2.1 Overscan, bias, darks and trimming

For the WFI data, we used [2097:2140,1:4128] as the overscan region for all chips, where the notation [X1:X2,Y1:Y2] is used with X1:X2 as the pixel range in X and Y1:Y2 the pixel range in Y. A one order polynomial fit was found for each image in the Y direction and then subtracted for each image. No bias was subtracted since, because it is an additive effect, it is removed with the sky subtraction. No dark subtraction was performed. However, dark exposures were taken in order to insure that there were no light leaks. Finally, the trim region for chip #50, #51, #52 and #53 was [51:2092,31:4127] while we used [51:2092,2:4098] for chip #54, #55, #56 and #57.

No overscan, bias or trimming corrections were necessary for the CPAPIR data. Dark subtraction was performed by simply taking the median of all dark images and subtracting from all sciences images.

3.2.2 Flat-fielding

For WFI data we used the dome flat for both pixel-to-pixel variation correction and to correct the global illumination. Dome flats were first combined, for each night and for each filter set, using the median of the counts. Then, we fitted a Legendre function of order 2 for each chip (in X and Y direction) and normalized these images with that fit. Although it was possible to perform a very good fit for the four central chip (#51, #52, #55 and #56), the normalization for the four chip on the corner of the WFI camera (#50, #53,#54 and #57) was not optimal due to fringing on the X and Y axis. In that step, we also set all subframes to a common zero point based on chip #54.

For CPAPIR data we used *superflat* (obtained by combining the science image frames for each night). For each superflat, images were normalized using the median of the counts and then each science frame was corrected with this normalized superflat. In Figure 3.6 we present a 357 x 357 pixel image from CPAPIR of field 9, before and after flat-field correction.

3.2.3 Sky and fringe subtraction

We made an initial sky subtraction via a low-order fit (Legendre function of order 2, both in X and Y) to the optical data from WFI. Afterwards, images were fringe subtracted when fringes were visible. This was the case for all medium band filters used, in a similar way as described by Bailer-Jones & Mundt (2001)[1]. In Figure 3.6 we present a 500 x 500 pixel image from chip #50 of field 15, before and after fringe subtraction. It was not necessary to perform fringe subtraction with images obtained with the broad band filter R_c.

For the infrared data from CPAPIR, sky subtraction was performed with a median combination of all (unregistered) images of the science frames (for a given field). No fringe subtraction was performed for the infrared data.

3.2.4 Registration and combination of images

The individual images of a given field were registered and median combined (this step was also done chip-by-chip for the WFI data). Instead of using a package that automatically

---

[1]A *fringe correction frame* was created, which is a median combination of all science frame with the same filter and same exposure time. This *fringe correction frame* was scaled by a factor – determined manually for each science frame – and subtracted from the science image.

detects the shifts and performs the registration, we obtain the X and Y position of a single object in all images to combine and register the images to the position in a reference image. This method allow us to perform a visual inspection of each image and reject, if necessary, images that are of poor quality. We used a bilinear interpolation in X and Y in order to compute the output shifted image.

Both for the optical data from WFI and for the infrared data from CPAPIR, combining was performed using the median at each pixel after having rescaled the images to a common flux scale, using the flux of more then 20 stars in each frame and in each chip for WFI data. Although a 3σ cliping was used, the median is prefered to the mean value in order to reject bad pixels and cosmic rays. For the outward and radial fields, 2 images with the 914/27 filter, 3 images with the 815/20 filter 28 images for each field in the J band were available for combination. We had 5 images in the R_c band for the radial fields and, as for the deep fields, we had 5 to 10 images available for combination in each filter.

3.2.5   Detection and aperture photometry of detected sources

For both the WFI and CPAPIR data we detected objects in the images using the IRAF task *daofind* and we performed aperture photometry using *wphot* in order to obtain magnitudes via aperture photometry together with an aperture correction following the technique used in Howell (1989). For WFI, we used apertures of 6 and 20 pixels in radius to perform aperture correction and photometry. With both, we used an annulus of 20 to 25 pixels around the objects and used the mode of the counts distribution as the sky level. For CPAPIR data, no aperture correction was performed (stars used for photometric calibration were in the same field and we used the same aperture to obtain the flux of these objects as well). For this instrument, we use an aperture of 4 pixels and a disk of 14 to 20 pixels for sky subtraction.

3.2.6   Coordinate determination and flux calibration

An astrometric solution was achieved using the IRAF package *imcoords* and the tasks *ccxymatch*, *ccmap* and *cctran*. For each field, a solution was computed for the 815/20 band image using the 2MASS catalogue as a reference. The RMS accuracy of our astrometric solution is within 0.15–0.20 arcsec for WFI data and within 0.3–0.4 arcsec for CPAPIR data. For WFI data, the astrometry was also performed on a CCD-by-CCD basis.

In order to transform our medium band instrumental magnitudes to the Johnson photo-

metric system, spectrophotometric standard stars were observed (Hiltner 600, HR 3454 and LTT 3864). The magnitude m_A is obtained from the average flux of a spectrophotometric standard star in specific band A using the equation,

$$m_A = -2.5 \log f_A \; + \; c_A, \qquad (3.1)$$

where m_A is the magnitude observed in a given passband, f_A the average flux received on Earth in this passband and c_A is a constant that must be determined. The average flux f_A will be given by,

$$f_A = \frac{\int_0^\infty f_\lambda S_A(\lambda) d\lambda}{\int_0^\infty S_A(\lambda) d\lambda}, \qquad (3.2)$$

where $S_A(\lambda)$ is the total transmission function of the passband for a given filter and f_λ is the source spectral energy distribution received at the Earth (in erg cm^{-2} s^{-1} Å^{-1}). The filter transmission function is convolved with the quantum efficiency of the CCDs (we assume the telescope and instrumental throughput is flat over each passband). The fluxes of each standard star, f_λ, were taken from Hamuy et al. (1992, 1994). The constant c_A for each passband is determined using the Vega flux from Colina et al. (1992), assuming m_A=0 in all passbands. The fitted values for these constants are $c_{770/19} = -22.2517$, $c_{815/20} = -22.4391$, $c_{856/14} = -22.6341$, $c_{914/27} = -22.8353$ and $c_{R_c} = -21.6607$.

To correct for Earth-atmospheric absorption on the photometry, we solved the equation by least squares fitting,

$$m_A = m_{A,raw} + Z_A + C_A(m_A - m_B) + \kappa_A X_A, \qquad (3.3)$$

for observations of the standard stars at a range of airmasses. The parameters m_A and m_B are the apparent magnitudes of our spectrophotometric standard in two particular bands (A and B), where $m_{A,raw}$ is the instrumental magnitude of our spectrophotometric standard stars, Z_A is the zero point offset, C_A is the colour correction, κ_A the extinction coefficient for band A and X is the airmass at which $m_{A,raw}$ was obtained.

We calibrated the CPAPIR infrared data using the J band values of 2MASS objects which were observed in the science fields. By determining a constant offset between the 2MASS magnitude and our instrumental magnitude, we obtained the zero point offset. Since this zero point offset was obtained with objects in the same field of view in each science frame, we did not perform a colour or airmass correction when reducing our NIR photometry.

3.3   Spectroscopic data reduction procedure

The standard CCD reductions (overscan subtraction and trimming) were performed on each image using the *ccdred* package under IRAF. We then used the IRAF package *dohydra* to perform flat-fielding (using dome flats), throughput correction (with the skyflats) and scattered light corrections. The spectra were wavelength calibrated using the PENRAY comparison lamp with 2 sec exposure time. Sky subtraction was performed in a similar manner as fringe subtraction in photometry: a *standard* sky spectrum (shown in Figure 3.7) was obtained from our sky spectra (more than 20 fibres were assigned for sky subtraction in each Hydra pointing) and scaled to optimize the sky subtraction for each science spectrum individually. However, this sometimes resulted in Hα appearing as absorption for some objects. We attribute this to Hα emission from the background itself. This is spatially variable and so subtracting the sky spectrum (which includes Hα) sometimes results in an over-subtraction of this feature. We discuss this contamination problem and the danger of determining membership status based on Hα in §5.2.2.

The radial velocity measurment was performed with the IRAF task *xcsao*. This task perform cross correlation against a spectrum with know radial velocity and also include barycentric correction. We used, as template, spectra of three M–dwarf from *The Indo-U.S. Library of Coudé Feed Stellar Spectra*: G 176-11 (M0), G 227-46 (M3) and HD204445 (M1). In the case of G 176-11 and HD204445 we used the area of 7500 to 8500 Å for the cross correlation while for G 227-46, only the region 7500 to 8000 Å was used.

The equivalent widith measurment was performed using the IRAF task *fitprofs* and a visual inspection of the measurments on each lines (such as Hα, the sodium doublet at 8200 Å and the lithium line at 6708 Å) was done using *fitprofs*.

Finally, flux calibration was performed with the spectrophotometric standard Hiltner 600, which was observed three times a night, at three different airmasses.

3.4   Effective temperature and mass determination

We used the spectral energy distribution as sampled by the multiple filters to derive the mass and effective temperature, T_{eff}, assuming that all our photometric candidates belong to IC 2391. We used evolutionary tracks from Baraffe et al. (1998) and atmospheric models from Hauschildt et al. (1999a) (assuming a grainless atmosphere; the NextGen model) to compute an isochrone for IC 2391 assuming an age of 50 Myr (Barrado y Navascués et al. 2004a) and distance of 146 pc. We assumed solar metallicity and we neglected reddening

for our near-infrared photometry reported here ([Fe/H]= -0.03 ± 0.07 and $E(B-V) = 0.01$; Randich et al. 2001). We estimated the mass and effective temperature via a least squares fit between the measured and model magnitudes. (We first normalized the energy distribution of each object to the energy distribution of the model using the 815/20 filter.)

There are different sources of error for the estimation of the mass and T_{eff}. These are from the photometry, the photometric calibration, the least squares fitting (imperfect model) and the uncertainties on the age and distance to IC 2391 (for which we use 5 Myr and 5 pc respectively). This last error gives $0.075\pm0.006\,\mathrm{M_\odot}$ and $2914\pm43\,\mathrm{K}$ for an object at the hydrogen burning limit and $1.000\pm0.027\,M_\odot$ and $5270\pm70\,\mathrm{K}$ for a solar type object. (The errors are obtained by adding in quadrature the difference in effective temperature and mass by using an age of 45 and 55 Myr and a distance of 141 and 151 pc compared to the adopted value of 50 Myr and 146 pc.)

We have now presented our complete sample of optical spectra and photometric data. However, objects observed in spectroscopy and objects detected in our images are not expected to be members of IC 2391. Therefore, a selection procedure is needed to reject the contaminants. In the next chapter, we will present the criterium to define if an object is a member of IC 2391 or not based on photometry and spectrcoscopy.
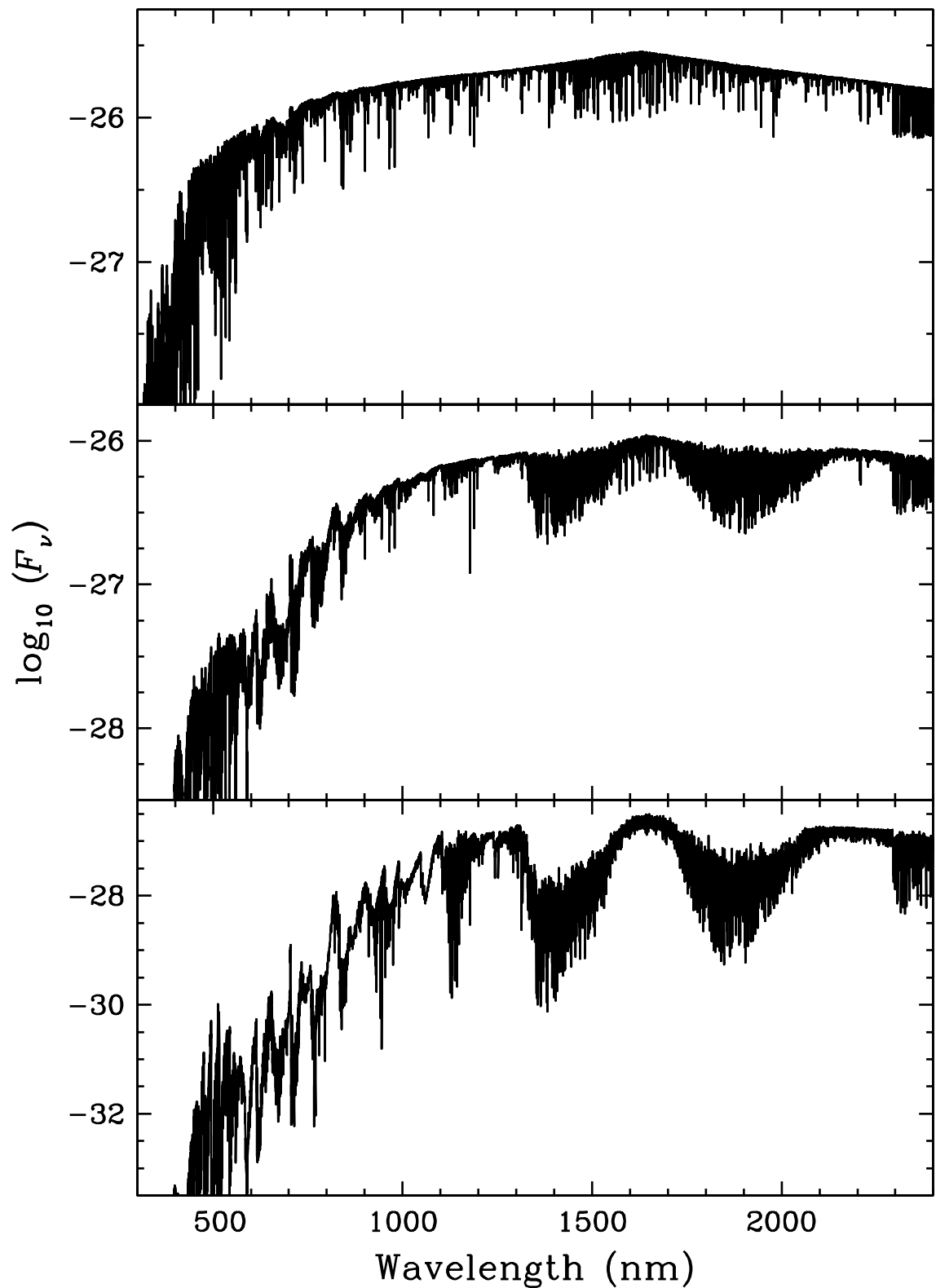
Figure 3.2 Three synthetic spectra with log $g = 4.5$ and solar metallicity (NextGen model). From top to bottom, the effective temperatures are 4200 K, 3000 K and 1700 K.
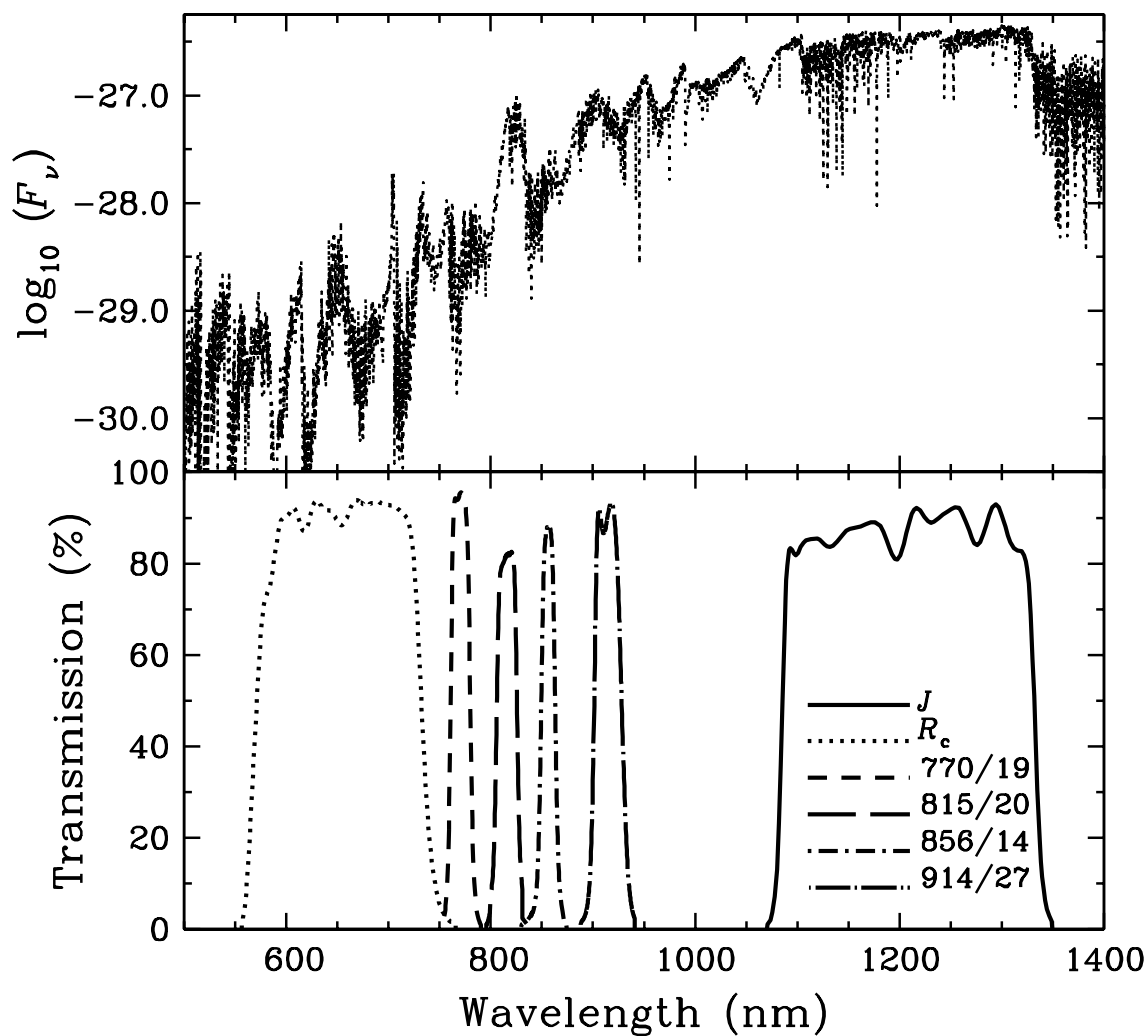
Figure 3.3 Transmission curve of the filters used in our survey compared to the synthetic spectrum of a brown dwarf with $T_{\mathrm{eff}} = 2300$ K, $\log g = 4.5$ and solar metallicity (NextGen model).
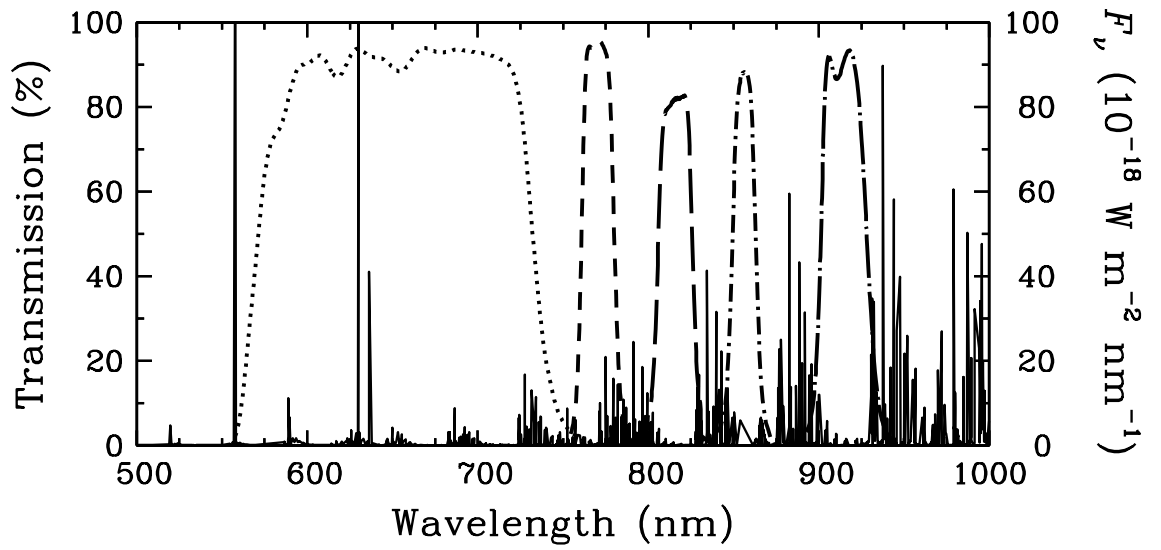
Figure 3.4 Passband function of the optical band used in our survey with the flux-calibrated, high-resolution spectra of optical sky emission from Hanuschik (2003).
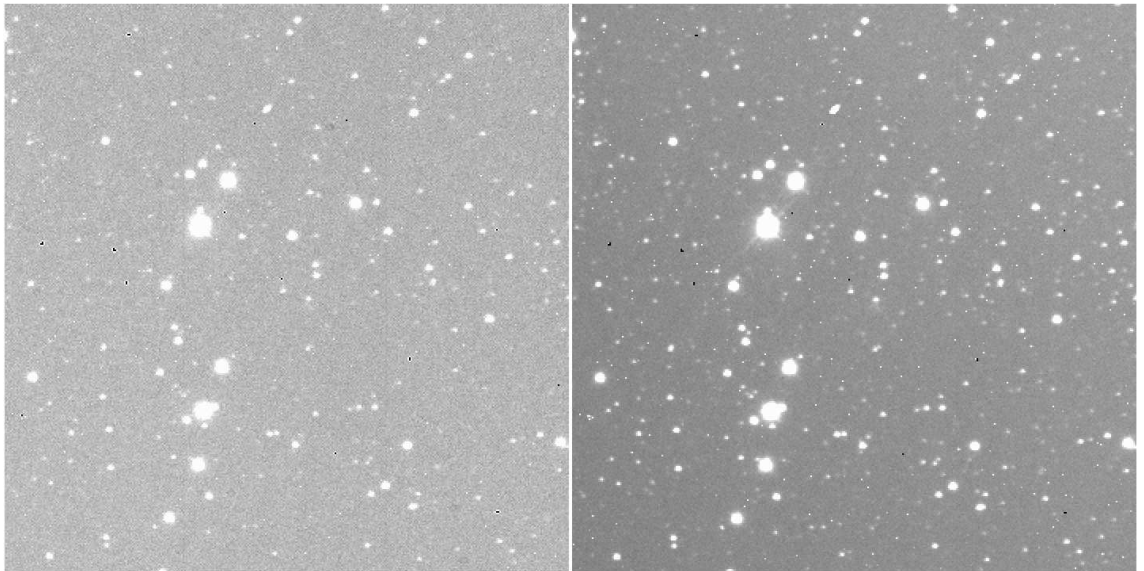
Figure 3.5 Image of 357 x 357 pixels from CPAPIR of field 9, before (left) and after (right) flat-field correction. This image was obtained with J band filter.
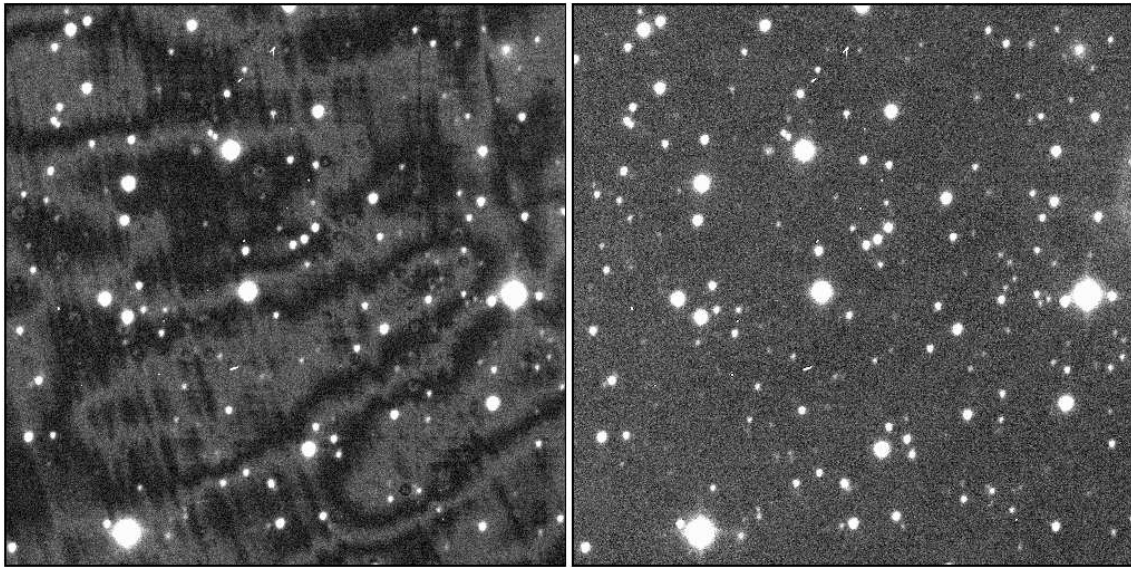
Figure 3.6 Image of 500 x 500 pixels from chip #50 of field 15, before (left) and after (right) fringe subtraction. This image was obtained with the filter 914/27.
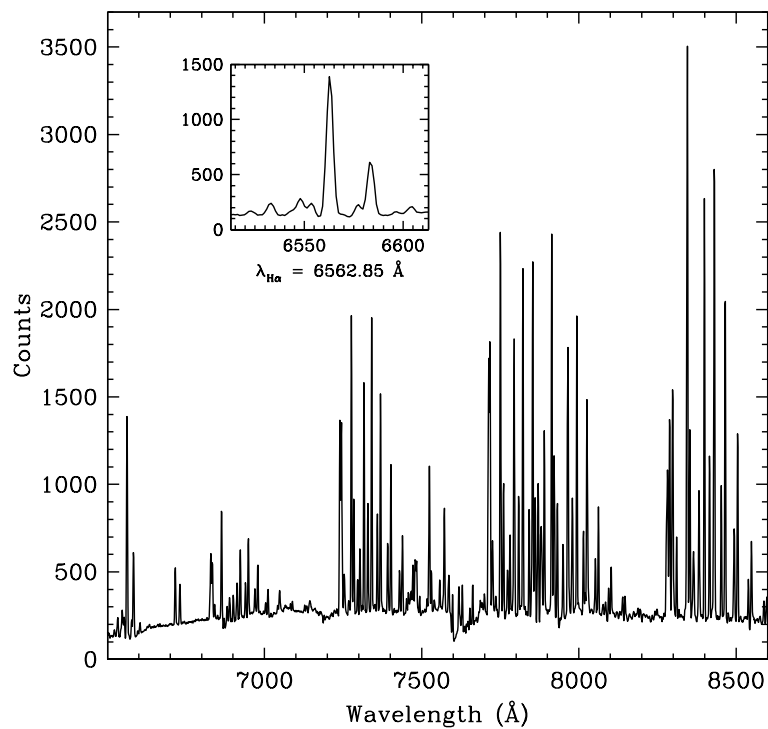
Figure 3.7 Spectrum used for sky subtraction of our spectroscopic data. Note the Hα (nebula) emission line with equivalent width of $W(\mathrm{H}\alpha) = 48\,\text{Å}$.

Table 3.1. Description of observations.

Field	RA	DEC	Distance (°)	Region name	R_c	770/19	815/20	856/14	914/27	J
01	8:24:38.8	-51:18:16.5	2.966	radial	1500/23.5	-	1800/20.8	-	600/19.7	1820/17.8
03	8:28:10.8	-50:46:50.0	2.945	radial	1500/23.8	-	1800/20.5	-	600/19.7	1820/17.7
04	8:27:56.8	-52:07:47.9	2.084	radial	1500/23.9	-	1800/20.5	-	600/19.5	1820/17.5
05	8:29:06.5	-52:26:14.6	1.793	radial	1500/23.7	-	1800/21.1	-	600/19.8	1820/17.5
06	8:30:30.6	-51:38:59.1	2.051	radial	1500/23.8	-	1800/21.1	-	600/19.7	1820/18.0
08	8:32:01.8	-52:15:26.1	1.481	radial	1500/23.9	-	1800/21.1	-	600/19.9	1820/17.9
09	8:33:15.7	-50:39:24.6	2.640	radial	1500/23.9	-	1800/20.8	-	600/19.8	1820/18.0
10	8:33:20.3	-51:50:14.6	1.616	radial	1500/24.0	-	1800/21.0	-	600/20.0	1820/18.0
11	8:34:06.5	-51:24:35.9	1.904	radial	1500/23.5	-	1800/20.7	-	600/19.8	1820/17.9
12	8:34:02.3	-52:45:43.2	0.978	radial	1500/23.7	-	1800/21.1	-	600/20.0	1820/17.9
14	8:36:17.4	-50:38:44.9	2.498	radial	1500/23.4	-	1800/20.8	-	600/19.7	1820/17.9
15	8:38:31.6	-53:35:29.4	0.757	deep	3900/22.7	3900/20.9	3000/20.7	1500/19.7	3000/20.3	-
17	8:37:37.6	-51:34:05.6	1.552	radial	1500/23.6	-	1800/20.9	-	600/19.7	1820/17.5
18	8:38:11.5	-52:01:44.1	1.085	radial	1500/22.7	-	1800/20.9	-	600/19.5	1820/17.6
19	8:38:17.7	-50:58:08.4	2.121	radial	1500/24.0	-	1800/20.6	-	600/19.6	1820/17.7
20	8:38:45.1	-52:35:58.0	0.519	deep	3900/22.4	3900/20.8	8400/21.3	15678/21.1	3000/20.3	-
21	8:41:22.5	-52:14:04.7	0.854	radial	1500/23.8	-	1800/21.2	-	600/19.9	1820/17.7
22	8:40:50.6	-51:31:11.6	1.553	radial	1500/23.7	-	1800/21.1	-	600/20.0	1820/17.8
24	8:39:59.7	-54:14:24.0	1.170	radial	1500/23.8	-	1800/20.5	-	600/19.7	1820/17.9
26	8:40:16.2	-55:16:12.0	2.200	radial	1500/23.7	-	1800/20.6	-	600/19.7	1820/17.7
27	8:41:01.5	-53:50:51.7	0.789	deep	3900/22.5	3900/20.7	9300/21.5	7800/20.4	4800/20.7	-
28	8:41:46.0	-54:46:27.8	1.720	radial	1500/23.8	-	1800/21.1	-	600/19.8	1820/17.5
31	8:44:09.0	-55:27:58.0	2.464	radial	1500/23.6	-	1800/20.5	-	600/19.5	1820/17.5
32	8:44:10.1	-52:39:49.0	0.721	deep	3900/22.3	3900/20.9	8450/21.4	10500/20.7	4800/20.5	-
35	8:44:39.7	-54:21:53.7	1.453	radial	1500/23.5	-	1800/21.0	-	600/19.9	1820/17.2
37	8:45:54.4	-53:25:53.5	0.927	radial	1500/23.5	-	1800/21.1	-	600/19.7	1820/17.5
38	8:47:00.8	-53:55:12.1	1.323	radial	1500/22.5	-	1800/20.9	-	600/19.6	1820/17.7
40	8:48:02.4	-55:09:16.4	2.380	radial	1500/22.8	-	1800/20.6	-	600/19.6	1820/17.7
41	8:48:09.8	-55:46:27.3	2.942	radial	1500/22.7	-	1800/20.4	-	600/19.4	1820/17.7
42	8:49:10.6	-54:35:58.2	2.023	radial	1500/22.7	-	1800/21.1	-	600/19.9	1820/17.5
43	8:50:15.8	-53:23:37.1	1.540	outward	-	-	1800/20.5	-	600/19.3	182017.5
46	8:53:03.1	-54:23:52.2	2.318	outward	-	-	1800/20.5	-	600/19.6	182017.3
47	8:53:26.1	-53:52:29.4	2.127	outward	-	-	1800/20.9	-	300/19.3	182017.3
48	8:54:39.8	-53:29:44.4	2.203	outward	-	-	1800/20.5	-	600/19.7	182018.2
49	8:56:47.5	-54:17:22.5	2.742	outward	-	-	1800/20.7	-	600/19.6	182017.8
c1	9:04:33.1	-57:17:06.6	7.407	control	1500/23.4	-	1800/21.1	-	600/20.5	1820/17.3

Table 3.1 (cont'd)

Field	RA	DEC	Distance (°)	Region name	R_{c}	770/19	815/20	856/14	914/27	J
c2	8:20:13.7	-48:36:26.0	6.694	control	1500/23.4	-	1800/20.5	-	600/19.7	1820/17.6
c3	9:10:00.0	-56:24:38.0	8.166	control	1500/23.5	-	1800/20.6	-	600/19.6	1820/17.6
c4	8:23:37.0	-49:25:48.0	5.515	control	1500/23.6	-	1800/19.4	-	600/18.9	1820/17.9

Note. — System notation is *exposure time in seconds / 10σ detection limit* while a – symbol indicates that no observations were performed for that field in that filter. *Distance* (°) gives the distance of the field from the cluster center (in degrees).

Table 3.2.   Objects for which spectra are available.

Field	ID	RA	DEC	SNR	815/20
15	02	8:38:27.108	-53:25:10.55	9.8	15.567
15	04	8:35:53.166	-53:22:11.77	4.	19.204
15	05	8:36:06.221	-53:28:06.48	5.1	18.967
15	07	8:35:00.736	-53:23:54.88	1.6	18.952
15	08	8:38:23.477	-53:24:29.07	0.5	18.843
15	09	8:37:24.833	-53:27:03.76	0.6	18.834
15	10	8:38:08.497	-53:36:34.38	1.4	18.838
15	12	8:37:47.255	-53:23:38.06	0.5	18.713
15	13	8:36:32.803	-53:48:27.41	11.9	18.712
15	15	8:34:54.776	-53:24:23.45	4.3	18.651
15	16	8:37:24.632	-53:19:48.37	5.5	18.656
15	17	8:35:06.758	-53:19:30.38	1.1	19.764
15	19	8:37:57.798	-53:43:54.69	6.9	18.547
15	20	8:36:26.653	-53:46:29.29	5.6	18.522
15	23	8:38:25.315	-53:36:16.38	0.5	18.506
15	25	8:36:12.232	-53:28:43.31	3.2	18.385
15	26	8:38:15.220	-53:27:55.13	0.8	18.334
15	27	8:37:26.524	-53:49:33.99	0.5	18.297
15	28	8:37:10.350	-53:38:43.22	6.	18.280
15	30	8:34:46.931	-53:27:11.37	2.2	18.278
15	31	8:36:54.229	-53:41:27.08	13.1	18.235
15	32	8:35:29.945	-53:36:49.00	5.4	18.187
15	33	8:36:25.082	-53:33:41.88	9.	18.078
15	34	8:37:20.901	-53:34:49.06	11.8	17.986
15	36	8:36:43.525	-53:29:42.28	19.4	17.892
15	37	8:36:18.241	-53:25:57.60	8.3	17.803
15	38	8:35:31.946	-53:37:15.48	7.	17.752
15	39	8:35:16.877	-53:50:25.75	4.3	17.709
15	40	8:37:21.423	-53:22:21.01	4.5	17.683
15	41	8:38:14.371	-53:37:57.85	0.7	17.591
15	42	8:36:26.818	-53:50:14.08	4.8	20.866
15	44	8:36:32.268	-53:33:55.23	9.7	17.440
15	48	8:37:22.883	-53:23:38.94	6.3	17.313
15	49	8:36:25.252	-53:39:54.53	16.4	17.237
15	50	8:34:58.773	-53:45:30.20	6.5	17.182
15	51	8:38:18.367	-53:46:53.79	15.2	23.580
15	53	8:37:41.091	-53:44:00.31	12.7	16.877
15	54	8:37:12.839	-53:46:09.43	6.8	16.643
15	55	8:36:05.866	-53:24:58.91	10.4	16.646
15	56	8:38:06.120	-53:38:10.55	9.	16.651
15	57	8:35:21.606	-53:42:05.12	8.	16.473
15	58	8:37:46.333	-53:20:22.54	4.	16.447
15	59	8:36:04.075	-53:29:25.00	20.7	16.306
15	60	8:36:40.363	-53:21:30.00	6.1	16.201
15	62	8:36:46.966	-53:38:31.22	23.5	15.891
15	63	8:36:54.586	-53:45:39.81	35.2	15.487
15	64	8:37:40.590	-53:45:57.99	13.4	15.435
15	65	8:38:22.952	-53:42:29.99	28.6	15.120
15	68	8:38:17.429	-53:24:41.36	5.2	19.178
15	69	8:37:54.086	-53:27:24.41	1.5	19.088

Table 3.2 (cont'd)

Field	ID	RA	DEC	SNR	815/20
15	70	8:36:34.643	-53:22:05.17	0.8	19.034
15	72	8:36:24.215	-53:20:12.91	2.8	19.115
15	75	8:37:52.713	-53:42:51.22	3.6	18.873
15	76	8:35:45.205	-53:50:04.22	3.5	18.899
15	78	8:38:26.031	-53:37:33.79	2.1	18.848
15	79	8:37:46.877	-53:30:41.54	1.4	19.114
15	80	8:36:30.984	-53:28:34.95	2.2	18.702
15	81	8:35:58.081	-53:40:27.05	2.	18.715
15	84	8:36:09.958	-53:48:52.69	1.5	18.701
15	85	8:35:10.572	-53:47:30.67	0.8	18.604
15	86	8:35:52.682	-53:38:10.53	3.4	18.587
15	87	8:38:04.168	-53:33:41.70	0.6	18.365
15	88	8:36:23.512	-53:42:25.37	5.3	18.370
15	90	8:36:28.072	-53:20:45.97	3.3	18.257
15	91	8:35:30.057	-53:44:56.58	0.9	18.234
15	93	8:36:20.262	-53:23:40.58	3.4	18.100
15	95	8:36:01.356	-53:39:24.50	9.1	20.261
15	96	8:36:46.246	-53:31:32.49	10.5	17.988
15	98	8:35:21.003	-53:28:04.39	2.9	17.607
15	99	8:36:51.793	-53:34:13.60	16.7	17.189
20	02	8:38:47.281	-52:44:32.61	17.	16.662
20	03	8:38:11.866	-52:22:51.09	26.1	16.633
20	05	8:39:24.080	-52:48:06.34	7.2	19.133
20	06	8:40:13.947	-52:51:23.34	1.1	19.166
20	07	8:38:13.504	-52:19:38.64	5.4	18.904
20	08	8:40:12.207	-52:25:55.52	7.6	19.801
20	10	8:37:25.510	-52:40:07.74	4.8	18.921
20	11	8:38:39.264	-52:43:37.10	5.9	18.849
20	12	8:37:56.884	-52:50:02.53	1.2	18.874
20	15	8:40:24.736	-52:44:31.08	5.1	18.706
20	17	8:38:42.432	-52:26:29.34	4.3	19.557
20	19	8:39:40.773	-52:49:11.77	0.5	18.573
20	20	8:40:07.148	-52:21:33.61	6.	18.608
20	23	8:40:48.947	-52:25:39.73	11.3	18.517
20	24	8:39:22.024	-52:36:56.51	7.	18.469
20	26	8:40:25.201	-52:20:50.98	6.6	18.494
20	27	8:39:12.127	-52:42:08.56	8.8	18.459
20	28	8:38:35.241	-52:36:50.93	10.9	18.474
20	29	8:40:33.271	-52:48:24.64	7.1	18.426
20	32	8:39:13.160	-52:50:56.79	2.5	18.272
20	34	8:39:50.948	-52:21:05.58	11.3	18.209
20	35	8:38:24.703	-52:44:18.77	10.2	17.995
20	38	8:39:29.612	-52:32:59.31	13.1	17.861
20	39	8:39:46.855	-52:21:27.85	12.1	17.849
20	40	8:37:28.753	-52:40:36.93	6.8	17.814
20	42	8:37:33.367	-52:44:57.58	10.5	17.658
20	43	8:37:33.974	-52:30:16.38	8.6	17.558
20	44	8:38:18.227	-52:36:45.94	12.7	19.657
20	45	8:40:16.671	-52:36:58.32	21.4	17.571
20	46	8:37:32.709	-52:23:36.72	7.6	17.500

Table 3.2 (cont'd)

Field	ID	RA	DEC	SNR	815/20
20	50	8:40:39.638	-52:50:42.80	13.4	17.210
20	51	8:40:45.126	-52:39:02.16	15.	17.200
20	52	8:40:26.611	-52:26:43.82	21.2	17.160
20	54	8:37:58.411	-52:20:30.69	22.	16.907
20	55	8:38:01.879	-52:29:56.00	19.6	16.847
20	56	8:38:36.649	-52:27:47.16	20.2	16.873
20	57	8:37:54.197	-52:21:26.33	22.	20.323
20	58	8:40:34.407	-52:30:38.65	32.	16.681
20	59	8:37:38.539	-52:29:35.37	9.2	16.645
20	60	8:39:33.260	-52:47:10.40	21.8	16.520
20	61	8:40:15.153	-52:40:24.56	26.5	16.494
20	62	8:39:22.724	-52:50:34.42	20.	16.433
20	63	8:37:34.755	-52:27:02.90	27.6	16.307
20	65	8:40:51.831	-52:34:48.35	50.7	19.010
20	69	8:40:47.048	-52:48:30.99	22.5	15.496
20	71	8:39:24.874	-52:21:45.52	4.1	19.163
20	74	8:39:17.189	-52:26:55.11	12.5	18.742
20	75	8:40:16.277	-52:26:27.39	8.1	18.625
20	77	8:39:29.183	-52:38:58.86	1.8	18.398
20	78	8:37:50.558	-52:33:04.66	6.	18.351
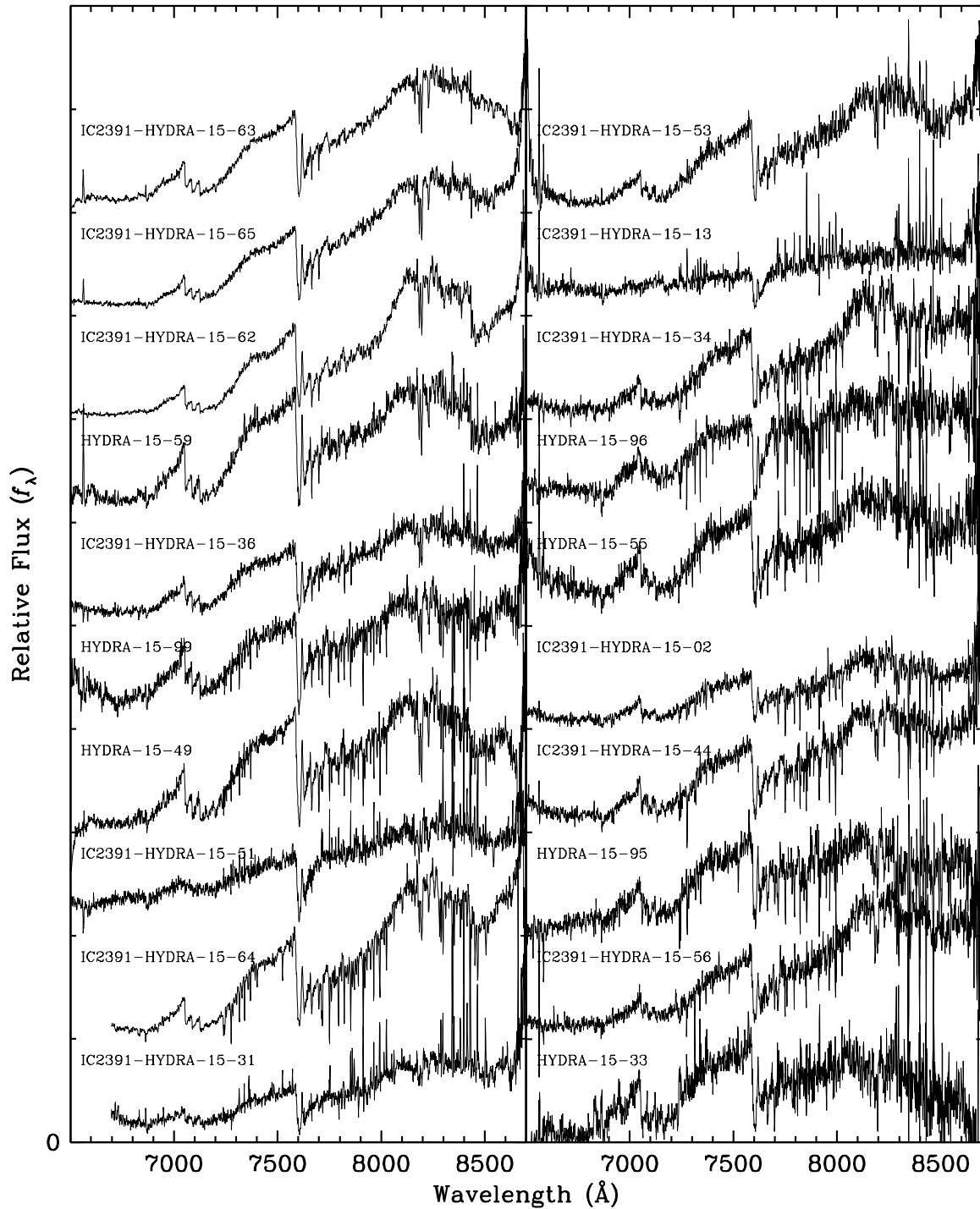
Figure 3.8 Spectra from field 15 with a SNR higher than 5 (highest top-left and lowest bottom-right). The notation is IC 2391-HYDRA-ZZ-YY (where ZZ is the field number and YY a serial identification number) but in some cases we present only the shortened version HYDRA-ZZ-YY.
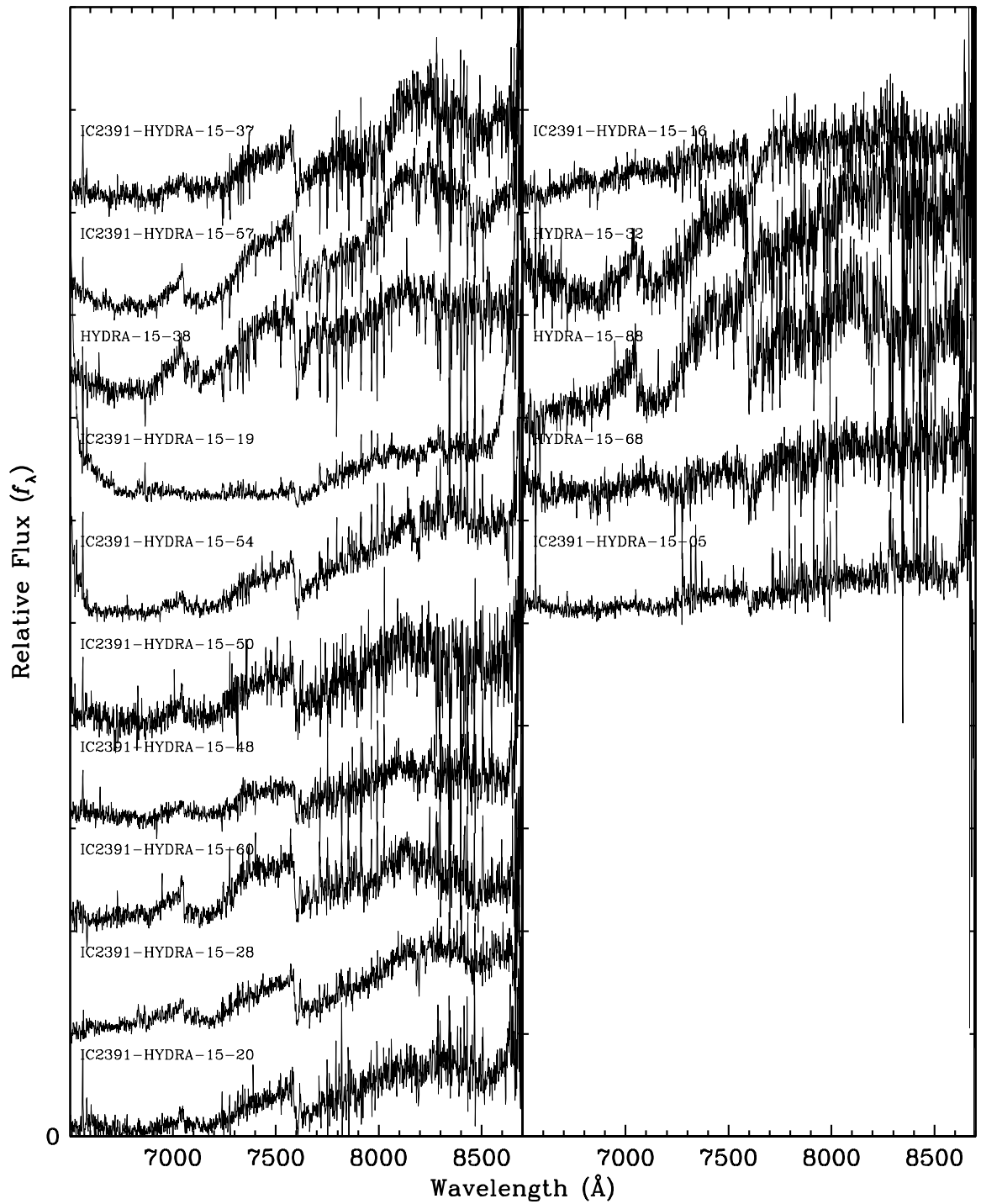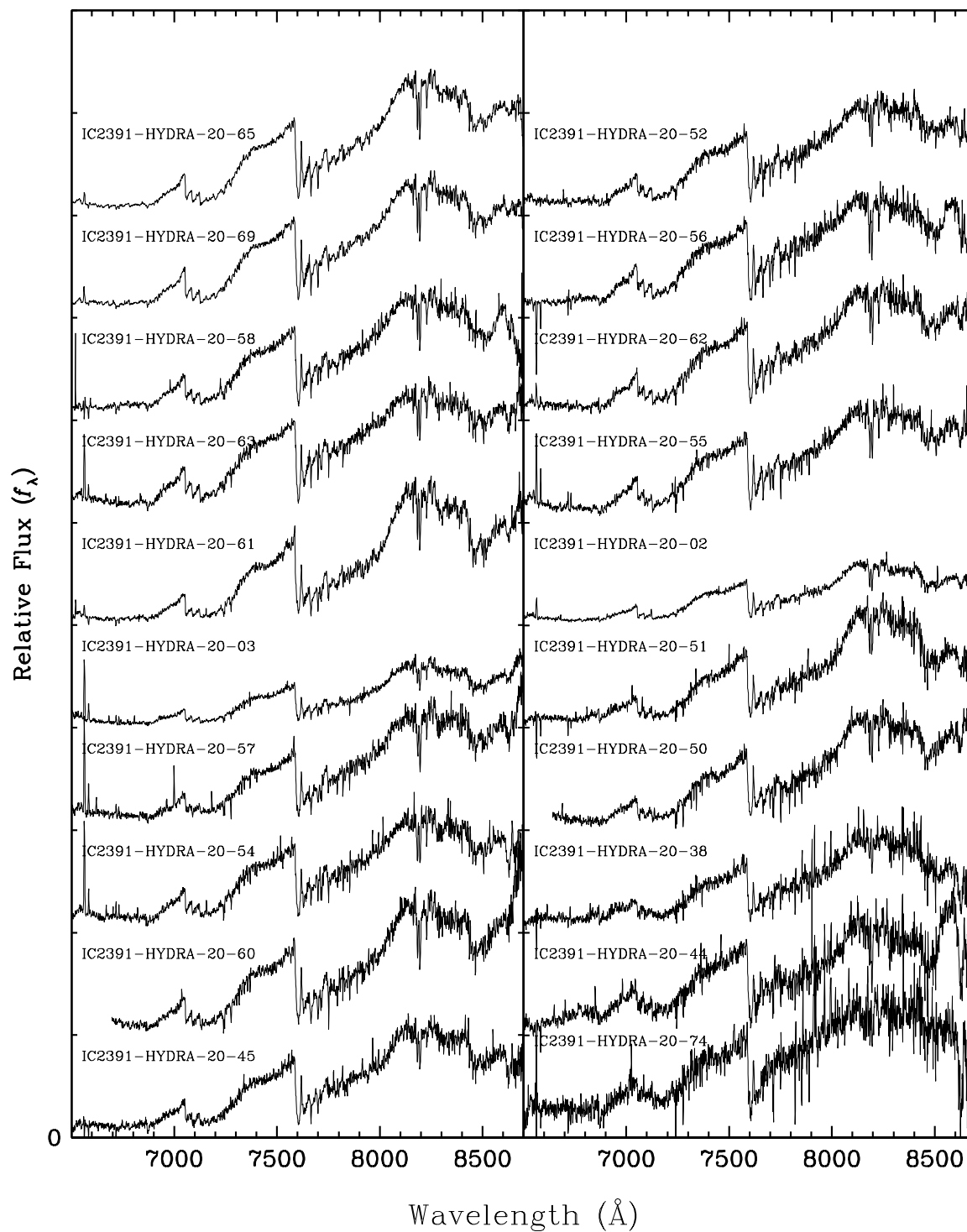
Figure 3.9 Same as Figure 3.8, but spectra from field 20.
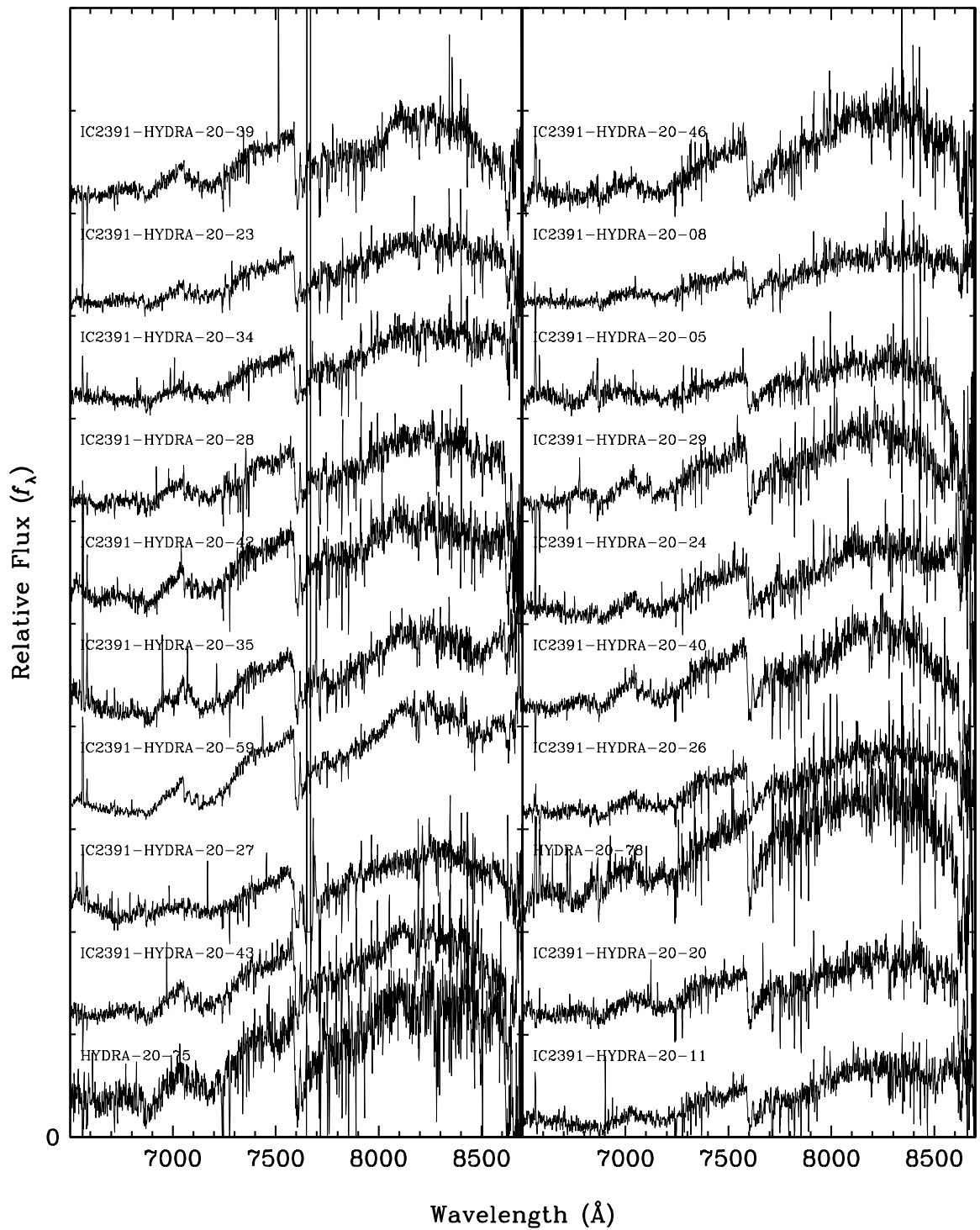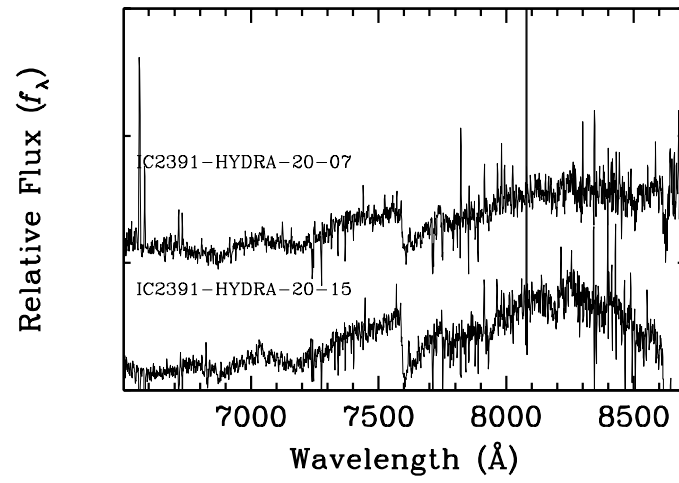
Chapter 4

Candidate selection procedure

From all our WFI fields, we have a total of 20 million objects detected above the 10σ detection limit ($\sim$510 objects per arcmin^2). The vast majority are not expected to be members of the cluster. Therefore, we need to perform an efficient selection using the magnitudes, colours, astrometry of each object and models available. Most of the selection procedures for IC 2391 in the previous work, presented in §1.4, rely on astrometry or a combination of colour-magnitude and colour-colour diagrams (the first method being too shallow while the second can have significant amount of contaminants).

This chapter is divided in two parts. We will first present the selection process based on photometry, which includes the use of colour-magnitude diagrams, colour-colour diagrams, the use of astrometry and the rejection of objects based on observed magnitude and predicted magnitude discrepancy. In the second part of the chapter, we will present the membership determination based on our optical spectra, which includes the use of equivalent widths of some lines (lithium line and sodium doublet), their positions (radial velocity measurements) and the spectral type of the objects observed. We will not used the Hα emission line and this issue will be discussed in more detail in the next Chapter (§5.2.1).

4.1 Photometric selection

The candidate selection process comrise of four main steps (and explained in more detail in the remainder of this section). Candidates were first selected based on colour-magnitude diagrams. A second selection was performed using colour-colour diagrams. Third, astrometry was used to remove objects with high proper motion. Finally, non-candidates were rejected based on a discrepancy between the observed magnitude in 815/20 and the magnitude in this band computed with the NextGen model and our estimation of the effective temperature.

4.1.1 First candidate selection: colour-magnitude diagrams

Candidates were first selected from our colour-magnitude diagrams by keeping all objects which are no more than 0.15 mags redder or bluer than the isochrones in all colour-magnitude diagrams. This number accommodates errors in the magnitudes and uncertainties in the model isochrones, plus errors from age estimation and distance to IC 2391 reflected on the isochrones. We additionally include objects brighter than $0.753\,\mathrm{mag}$ from the isochrones in order to include unresolved binaries. In Figure 4.1 we show two colour-magnitude diagrams for field 01 where candidates were selected based on 815/20 vs. 815/20–914/27 and R_c vs. R_c–J (*top 2 panels*). We also present two colour-magnitude diagrams from the deep field 32 using the medium band 770/19, 856/14 and 914/27 (*lower 2 panels*). From a total of $20\,008\,114$ objects detected, $174\,511$ are kept (99.2% are rejected).

4.1.2 Second candidate selection: colour-colour diagrams

The second stage of candidate selection was achieved by taking all objects within 0.15 mag of the isochrone of the NextGen model in selected colour-colour diagrams. In Figure 4.2, we present two colour-colour diagrams where only the objects from the first selection are plotted. Since one source of contamination is background red giants, we show theoretical colours for such objects using the atmosphere models of Hauschildt et al. (1999b), assuming that all objects have a mass of $5\,\mathrm{M_\odot}$, $0.5 < \log g < 2.5$ and $2000\,\mathrm{K} < T_\mathrm{eff} < 6000\,\mathrm{K}$. We can see that R_c–J vs. R_c–815/20 is not best suited for selecting candidates since the isochrone is overlapped by red giant contaminants. However, in 815/20–J vs. 914/27–J, we see a clear distinction between the isochrone and the red giant contaminant in the brown dwarf regime (by more than 0.2 mag). This procedure definitely helps to remove red giant contaminants, and is further discussed in subsection 5.2.2. Also, the variation of colour as a function of

T_{eff} was used to reject colours for which the NextGen model shows small variation in the M and L dwarf regime (this is illustrated in Figure 4.3 with the 815/20–914/27 colours). From a total of 174 511 objects, 33 794 are kept (80.6% are rejected).

4.1.3   Rejection of contaminants based on proper motion

Although the RMS error of our astrometry is 0.15-0.20 arcsec (WFI) and 0.3-0.4 arcsec (CPAPIR), we nonetheless estimated proper motions using the motion between the 1999/2000 WFI data and the 2007 CPAPIR data in an attempt to reject objects which deviate significantly from the mean cluster proper motion in the literature. The values of proper motion from the literature are (-25.04±1.53,+23.19±1.23), (-25.05±0.34,+22.65±0.28), (-24.64±1.13,+23.25±1.23) and (-25.06±0.25,+22.73±0.22) from Dodd (2004), Loktin & Beshenov (2003), Sanner & Geffert (2001) and Robichon et al. (1999) respectively, where $(\mu_\alpha\cos\delta,\mu_\delta)$ stand for the proper motion in right ascension ($\mu_\alpha\cos\delta$) and in declination (μ_δ) in units of milliarcsec per year (mas yr^{-1}). For our selection procedure we use the average of these, (-25.0±2.0,+23.0±1.7).

First, we investigated whether the cluster itself could be identified in a proper motion diagram (such as presented in Figure 4.4). To do this, we retained only those objects detected from our observation runs with WFI (1999, 2000 and 2007) and CPAPIR (2007) which have a match within 72 mas. We then examined the distribution in the $(\mu_\alpha\cos\delta{:}\mu_\delta)$ plane for any feature at (-24.95:+22.96). However, we see no clump in the distribution of the proper motion (Figure 4.4). Considering the large errors and the absence of any structure at the expected location, we decided not to perform any selection using the proper motion of IC 2391. However, astrometry is used to remove all objects with a proper motion higher than 72 mas yr^{-1}.

4.1.4   Rejection of objects based on observed magnitude vs. predicted magnitude discrepancy

As indicated in §3.4, our determination of T_{eff} is based on the energy distribution of each object and is independent of distance. The membership status is determined by comparing the observed magnitude of a given object in a band with the magnitude predicted based on its derived T_{eff} and IC 2391's isochrone [1] In order to avoid removing unresolved binaries that are real members of the cluster, we keep all objects with a computed magnitude of up

---

[1]The premise is that the predicted magnitude of a background contaminant would be lower (brighter) than its observed magnitude and higher (fainter) for a foreground contaminant.

to 0.753 mag brighter than the observed magnitude. In this procedure, we are also taking into account photometric errors and uncertainties in the age and distance determinations of IC 2391. This is represented in Figure 4.5. Combined with the rejection of contaminants based on proper motion, this selection step rejects 89.2% of the 33 794 candidates obtained from the CMD and color-color diagrams, which gives us a final list of 3187 candidates. Table give a summary of the four selection procedure and the fraction of objects rejected at each step.

4.2   Spectroscopic selection

We use the Li I line at 6708 Å to help confirm the substellar status of photometric candidates and to establish membership of IC 2391. Lithium can be observed in young, more massive stars with radiative interiors because of less efficient mixing than in fully convective low-mass stars (e.g. Manzi et al. 2008). For young, fully convective, low-mass stellar objects, lithium may still be present in the atmosphere, as not all lithium has been "burned" (Manzi et al. 2008). For older lower mass brown dwarfs ($\lesssim 0.065 \, M_\odot$), objects preserve their initial lithium content (Rebolo et al. 1996). Here we assume that stellar objects (with $M \gtrsim 0.072 \, M_\odot$) are too old to have preserved lithium in their atmosphere, and since the spectroscopic follow-up was performed in order to obtain spectra of objects with $M \lesssim 0.2 \, M_\odot$, the presence of the LiI line is a direct membership criteria for brown dwarfs in IC 2391.

The sodium doublet at 8200 Å is sometimes used to exclude field M–dwarf contaminants because it is a gravity indicator (its equivalent width is proportional to log g; Martín et al. 1996). Brown dwarfs contract as they age, increasing the surface gravity. Since field late M–dwarfs near the cluster will generally be much older, and thus more massive for a given spectral type, a larger equivalent width indicates a more evolved object (for a common chemical composition). We use the equivalent width measurement of CTIO-046 from the Barrado y Navascués et al. (2004a) survey (W(NaI)=7.3±0.2 Å) as a limit for IC 2391 members and field stars.

As for the radial velocity criteria, we exclude candidates which differ significantly ($\pm 3\sigma$) from a recent determination of the cluster's radial velocity (16±3 km/s, Kharchenko et al. 2005, where σ is the the error of the radial veolicty of IC 2391 added in quadrature with the error of our candidates). We didn't used radial velocity measurment for which errors exceed 30 km/s, which is ten time the error on the radial velocity of IC 2391.

Finally, we use the SpT determination to obtain T_{eff} and masses for each spectrum. In order to be confirmed as a (spectroscopic) cluster member, the spectroscopic T_{eff} and mass

must agree with the photometric T_{eff} and mass to within $200\,\text{K}$ and $0.02\,\text{M}_\odot$ respectively.

We present in Figure 4.6 8 spectra of our sample. For these objects, we present a close-up view of the area of the Li absorption line and the Na doublet. We also present on Table a summary of the spectroscopic selection procedure and the number of objects rejected.

In the following chapter we will present the members based on our photometric and spectroscopic membership determination and we will proceed with the analysis of our data.

Table 4.1. Selection procedure used in photometry with the number of object
before/after selection and the fraction rejected.

Selection procedure	Initial number of objects	% rejected	Number of objects keept
Colour-magnitude diagrams	20 008 114	99.2%	174 511
Colour-colour diamgrams	174 511	80.6%	33 794
Astrometry	-	-	-
Observed 815/20 vs. Predicted 815/20	33 794	89.2%	3187

Note. — Since the astrometry was used when combining the data from various filter and not as a rejection criteria, no number or fractions of objects rejected is presented.

Table 4.2. Selection procedure used in spectroscopy with the number of object rejected.

Selection procedure	Number of objects rejected
Radial velocity	12
$W(\mathrm{NaI}) > 7.3 \pm 0.2\,\text{Å}$	0
$T_{\mathrm{eff}[SPEC]} \neq T_{\mathrm{eff}[PHOT]}$	32
$\mathrm{M}_{[SPEC]} \neq \mathrm{M}_{[PHOT]}$	37

Note. — The number of object given is the number of objects that does not satisfy the criteria, and not the number of objects rejected only by this criteria.
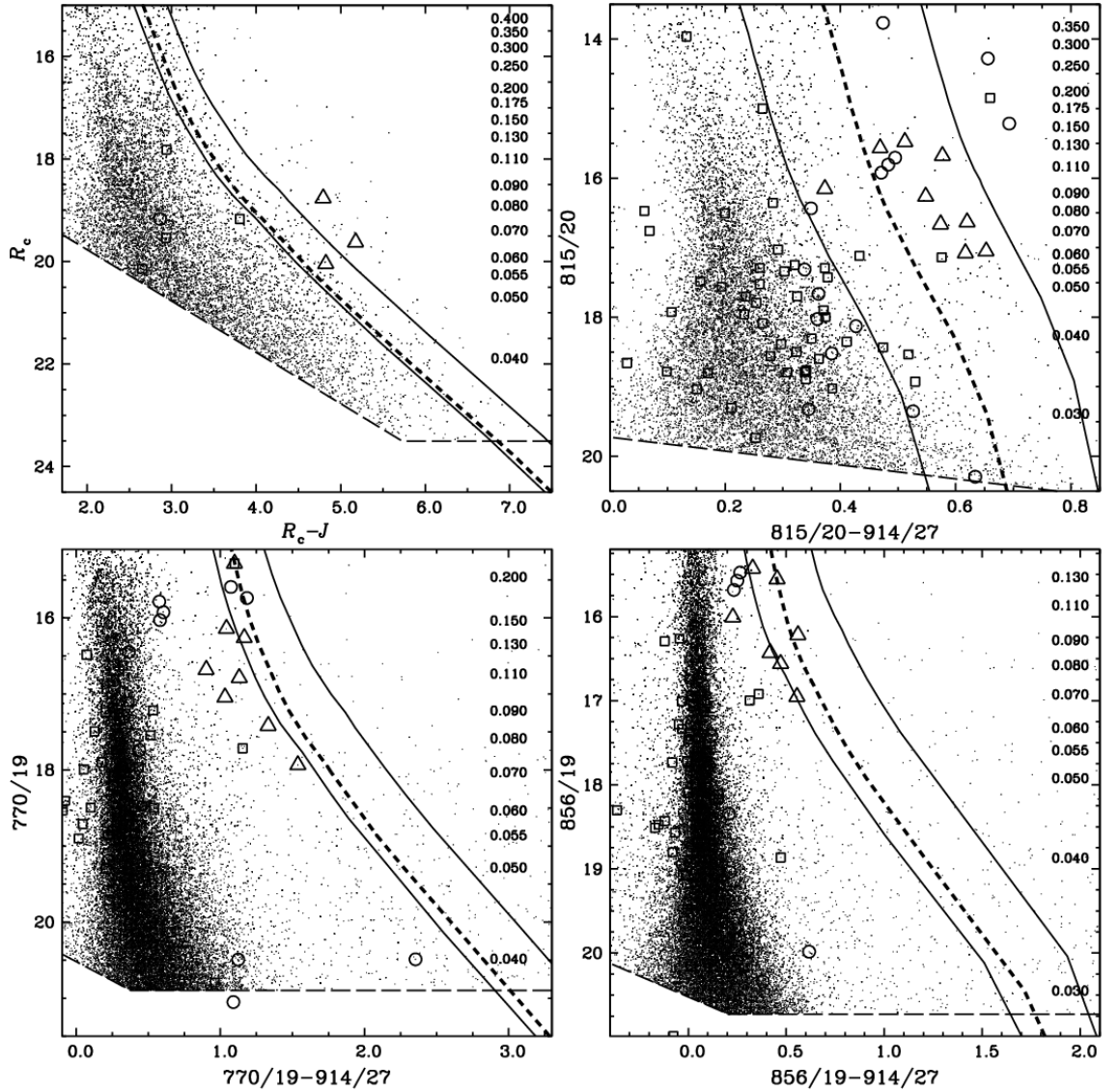
Figure 4.1 *Top.* Two Colour-magnitude diagrams from the radial field 01. Dotted lines show the isochrone computed from an evolutionary model with a grainless atmosphere (NextGen model, the masses for each R_c are shown in the right panel). The thin dashed line is the 10σ detection limit. We also show candidate low-mass cluster members from Barrado y Navascués et al. (2004a) (*triangles*) and Dodd (2004) (*squares*) and X-ray sources detected by XMM-Newton (*circles*), which we detected in our survey. Some of these objects are not present in the left panel since the deep fields, where most of these objects are detected, don't have *J*-band photometry. *Bottom.* Two Colour-magnitude diagrams from the deep field 32 with medium bands. Isochrones, 10σ detection limit and cluster members from previous studies are the same as for the top two panels. In each panel, the thin solid line represents the selection curve.
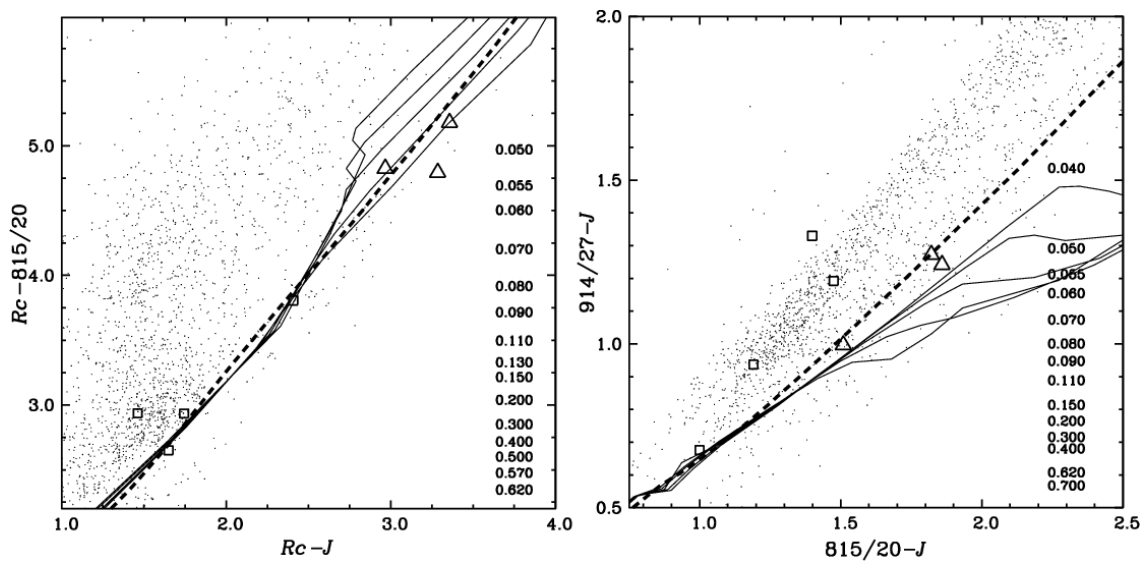
Figure 4.2 Two colour-colour diagrams of objects that are candidates based on our first selection (from field 01). Isochrones and objects from Barrado y Navascués et al. (2004a) (*triangles*), Dodd (2004) (*squares*) and XMM-Newton (*circle*) are as shown in Figure 4.1. The thin lines represent the colour of possible background red giant contaminants. The colour-colour diagram on the left is therefore not suited for further candidate selection since the isochrone is spanned by the colour grid of the red giants (which is not the case for the colour-colour diagram on the right).
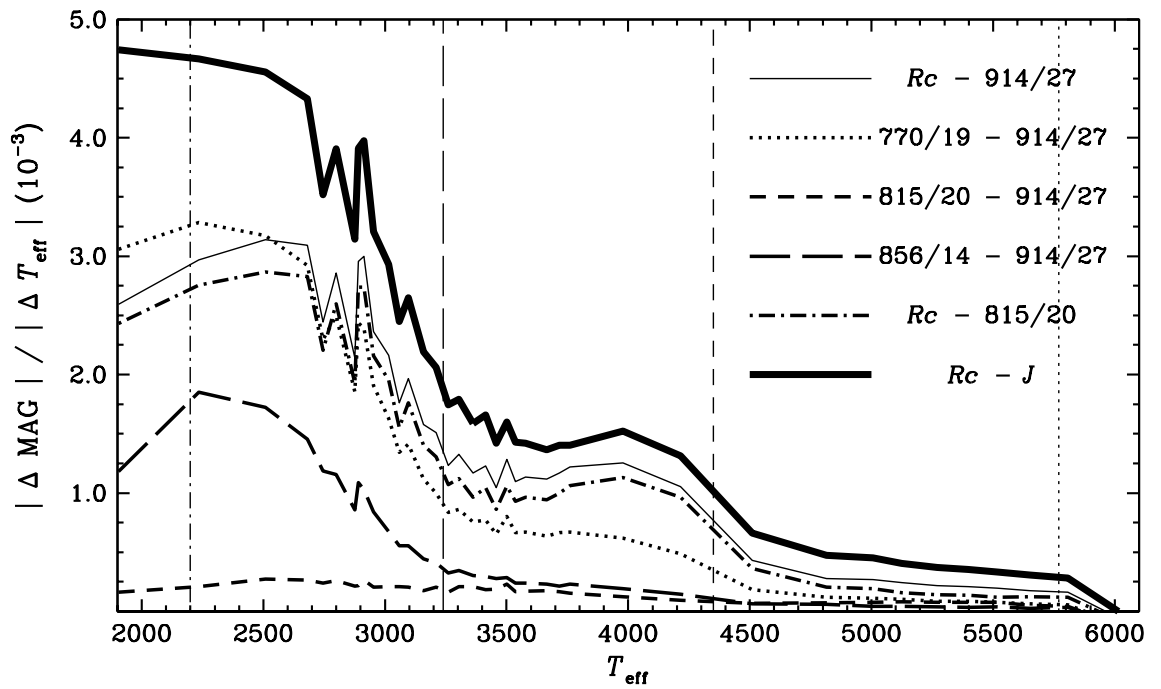
Figure 4.3 Colour sensitivity against the effective temperature for the medium band filter 914/27. The vertical lines represent the approximate effective temperatures for spectral classes L0V (dash-dotted line), M5V (long-dash line), K5V (short-dash line) and G5V (dotted line). We can see that there is no variation at all for 815/20-914/27 compared to other colours at the L0V and M5V regime.
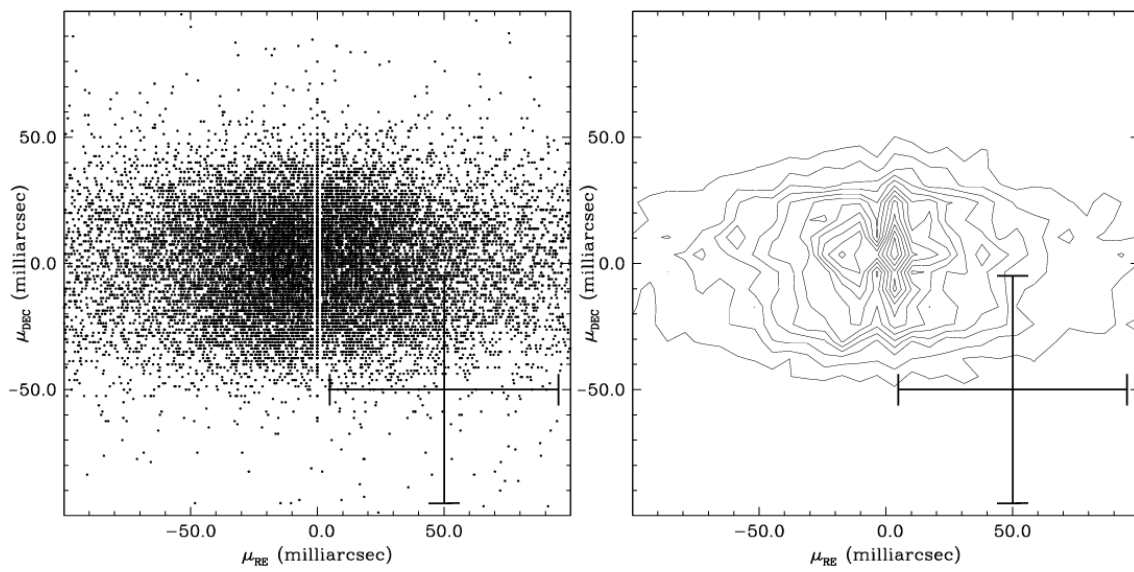
Figure 4.4 *Left.* Proper-motion diagram from our survey using our 8 years baseline. IC 2391 is at (-25.0,+23.0). The typicaly error bar of individual objects in our survey is shown. For clarity, only one object out of five is shown. *Right.* Contour plot of the same data.
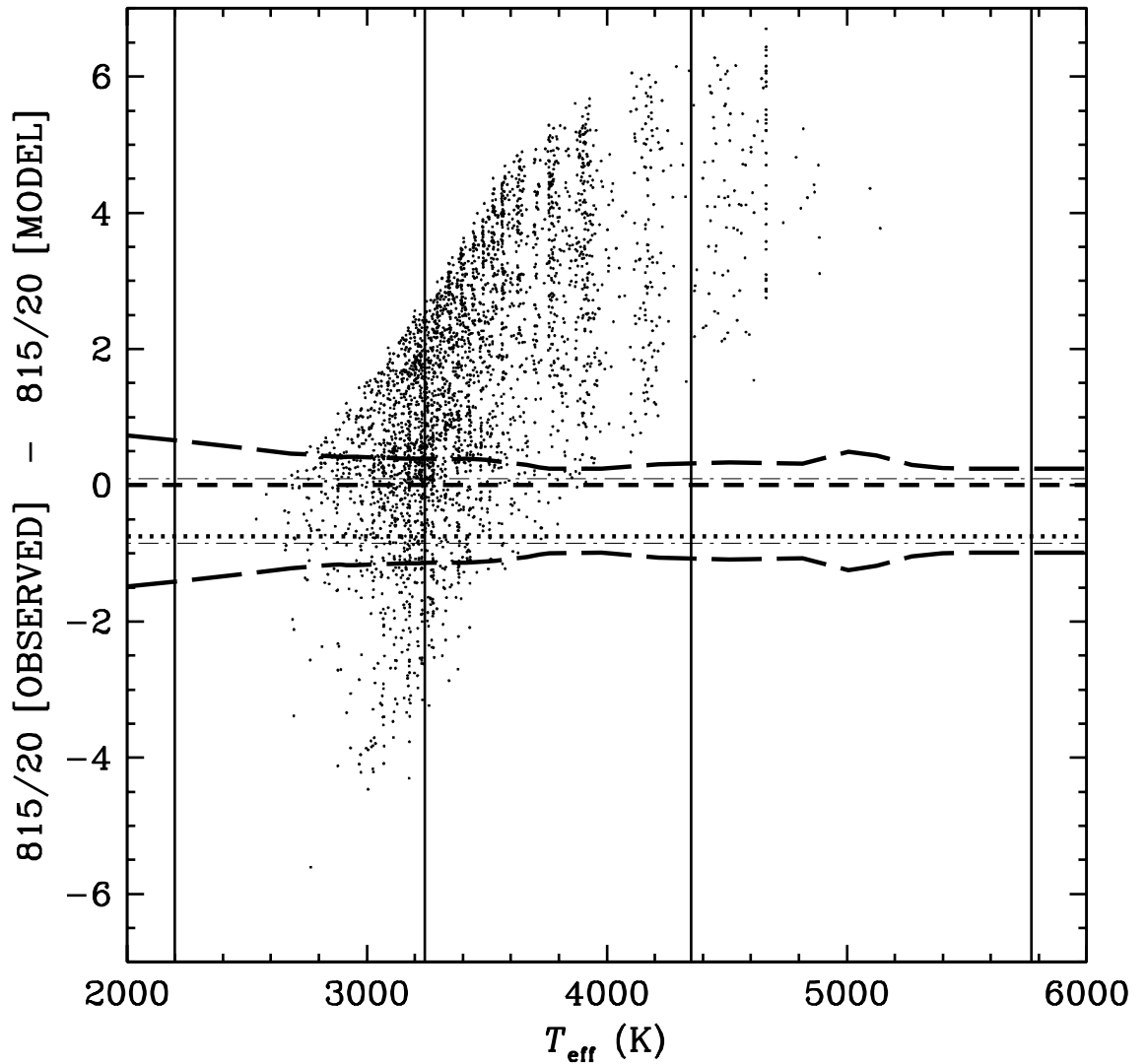
Figure 4.5 Difference between the observed 815/20 magnitude and that computed from the derived mass and effective temperature, as a function of effective temperature. The four vertical lines are at the positions of L0, M5, K5 and G5 dwarfs (left to right). The dotted line (at -0.753) represents the error due to the possible presence of unresolved binaries, the dashed-dotted lines represent the error on the magnitude determination and the long dashed lines represent the uncertainties on the age and distance of IC 2391. (The short-dashed line just traces zero). For clarity, only one object out of three is shown.
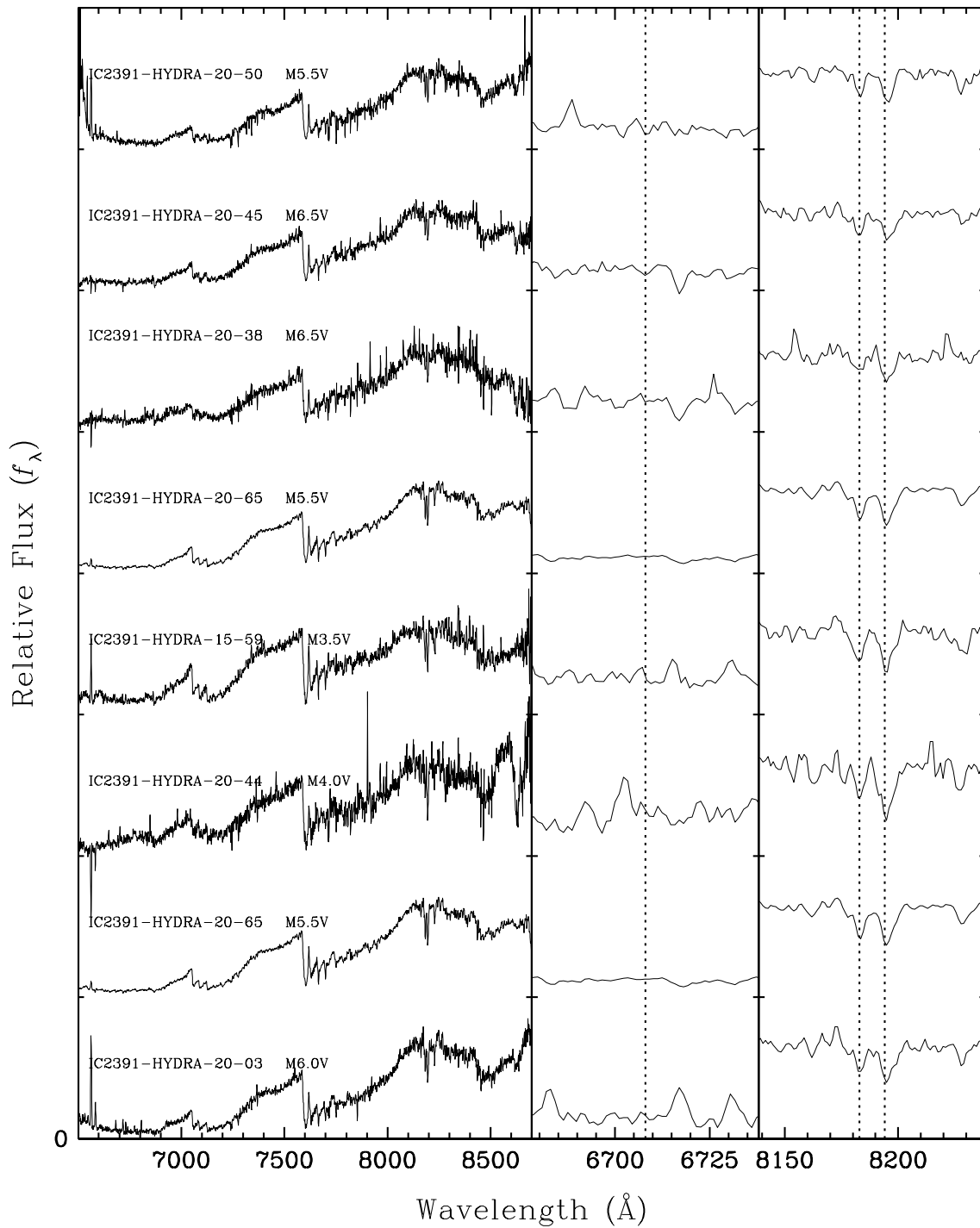
Figure 4.6 Spectra of eight objects, all defined as members of IC 2391 based on our criteria. On the two rights panel we present, for each spectra, a close-up on the Li absorption line and the Na doublet. We can observe the Li absorption line at 6708 Å for the top two objects IC2391-20-45 and -50.

Chapter 5

Results of our survey on IC 2391

We have seen in Chapter 2, §2.1, that the mass function can be used to study a population of a system e.g. stellar cluster or galactic thin disk population), from massive stars to low-mass brown dwarfs. Now that we have a list of possible members of IC 2391 with estimations of their masses based on photometry, we can compute the mass function in order to study the stellar and substellar population of this open cluster. We also have a list of spectra of photometric candidates available. With this, it will be possible to estimate the contamination rate of our photometric selection and to compute a spectroscopic mass function.

Here we will present our analysis of our photometric and spectroscopic data on IC 2391. In the first part of this chapter we present the results based on our photometry. We report on a discovery based on the shift in the colours of the bulk of the field stars from field to field, apparently due to variable extinction in the background field star population. Then, the subsections that follow will be used to discuss the mass function derived from the deep fields and from outward fields only. The other fields are used to study the radial variation of the stellar and substellar mass function and are the subject of a further discussion in the subsequent two subsections. In the second part of this chapter, we will present our spectroscopic results. Namely, we will present the discovery of the high spatial variation of the background Hα contaminations. We will discuss the results acquired by the spectroscopic data (including the contamination rate and the presentation of a spectroscopic mass function) and we will conclude this chapter by presenting the finding charts and the spectra of new brown dwarf members of IC 2391. Finally, we will again obtain the stellar and substellar mass function of IC 2391, but using only public data available from the *Two Micron All Sky Survey* (2MASS). We will compute the mass function based on J, H and K_s photometry from 2MASS and confirm or refute our results, using data obtained with different telescope/instrument configurations and processed differently and independently of our current work.

5.1   Photometric results

The final selection gives us 954 photometric candidates for the five radial fields for which photometry is available in 815/20, 914/27 and J (namely fields 43, 46, 47, 48 and 49, also named the outward fields), 499 photometric candidates for the four deep fields (15, 20, 27 and 32, with filters R_c, 770/19, 815/20, 856/14 and 914/27) and 1 734 for all other radial fields (observed with filters R_c, 815/20, 914/27 and J). All our photometric candidates are presented in Table 5.1 at the end of this chapter. Objects are given the notation IC 2391-WFI-ZZ-YYY where ZZ is the field number and YYY a serial identification number (ID). Only the first 10 rows of the tables are shown as the remainder are available online (Boudreault & Bailer-Jones 2001). We also compare in Table 5.2 (at the end of this chapter) all objects in our sample which are also confirmed as cluster members from Barrado y Navascués et al. (2004a) and Dodd (2004) which were detected by the X-ray Multi-Mirror Mission (XMM-Newton). We see good agreement between T_{eff} from our photometric data and from Barrado y Navascués et al. (2004a), where only the colour $(R - I)c$ was used to compute T_{eff}.

Our 10σ detection limit is J=17.7 and 914/27=19.2 for the radial and deep fields respectively (which correspond to $\sim 0.03\,\mathrm{M_\odot}$ for both cases). The brightest objects without saturation in the short exposures in our survey are at $J \sim 10$ ($\mathrm{M_\odot} \sim 0.9\,\mathrm{M_\odot}$) for outwards and radial fields and at $914/27 \sim 12.5$ or ($\mathrm{M_\odot} \sim 0.6\,\mathrm{M_\odot}$) for deep fields. However, we can't expect to detect *all* objects down to these magnitudes. The completeness from brightest objects without saturation down to the 10σ detection limit is estimated by taking the ratio of the number of objects detected over the predicted detections. This prediction is obtained with the histogram of the number of detection as a function of magnitude (Figure 5.1) and by using the fit of the best line up to the decrease in detection. (Assuming that a power law relation between the number of object detected with the magnitude limit). The completeness of the radial part of the survey is 91.8% while for the deep part it is 82.7%.

We consider the mass function of all radial fields within 2.1° of the cluster center as the mass function obtained for IC 2391. Fitting the lognormal mass function (as presented in eq. 2.4) to our data for all fields within 2.1° of the cluster center, we obtain k=10.7, m_0=0.13$\mathrm{M_\odot}$ and σ=0.46. The figures used for the analysis of the mass functions for the deep, radial and outward fields, show this result.
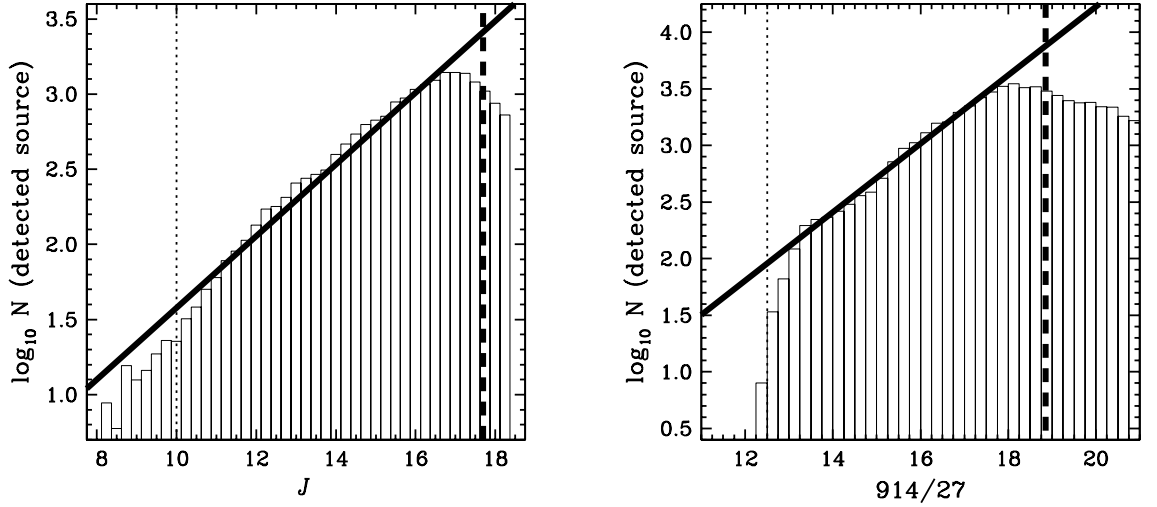
Figure 5.1 Estimation of the completeness limit for the radial and outward fields of our survey using the J band (*left*) and of the deep fields using 914/27 (*right*). The thick lines give the best linear fit before the turn off; the vertical thick dotted line is the $10\,\sigma$ detection limit and the vertical thin line is the magnitude at which saturation started to occur in the short exposures.

5.1.1 $E\,(\,B\,\text{-}\,V\,)$

In comparing the colour-magnitude diagrams for different fields, we discovered something peculiar (Figure 5.2, top 3 panels). We see a shift in the colours of the bulk of the (field) stars from field to field, something we also observe in other colours. The comparison of the amplitude of this shift (for a given magnitude interval) with observational parameters such as nights, airmass, seeing and 10σ detection limit shows no correlation and there is no other indication of reduction problems. We did, however, find a week correlation of the colour shift with the galactic longitude b. However, in order to verify that these shifts were real, we obtained DENIS photometry (*Deep Near Infrared Survey of the Southern Sky*) in I and J band for the same fields presented in Figure 5.2, which are fields 01, 09 and 40. We can see that the shift in the colours of the bulk of the (field) stars is also observed in the DENIS data (Figure 5.2, lower 3 panels).

Although reddening is negligible for objects in IC 2391, this is not the case for background objects, and these constitute most of the stars in our sample. Due to the high variation of the background extinction in this direction of the Galactic disk (Schlegel et al. 1998) – the cluster is centered at l=270.4 b=-6.9 – some variation in the colour-magnitude diagram locus could be extinction-induced variations in the background stars. In Figure 5.3 (*left*),

we plot the reddening $E(B-V)$ in our fields against the median of the colour 815/20-914/27 (in a bin of magnitude of $15 < 815/20 < 16$) for all our fields. The colours vary by as much as 0.25 mag. To better illustrate the spatial variation of the background extinction, Figure 5.3 (*right*) shows the position of the fields of our survey overplotted with the $E(B\text{-}V)$ extinction map of Schlegel et al. (1998).
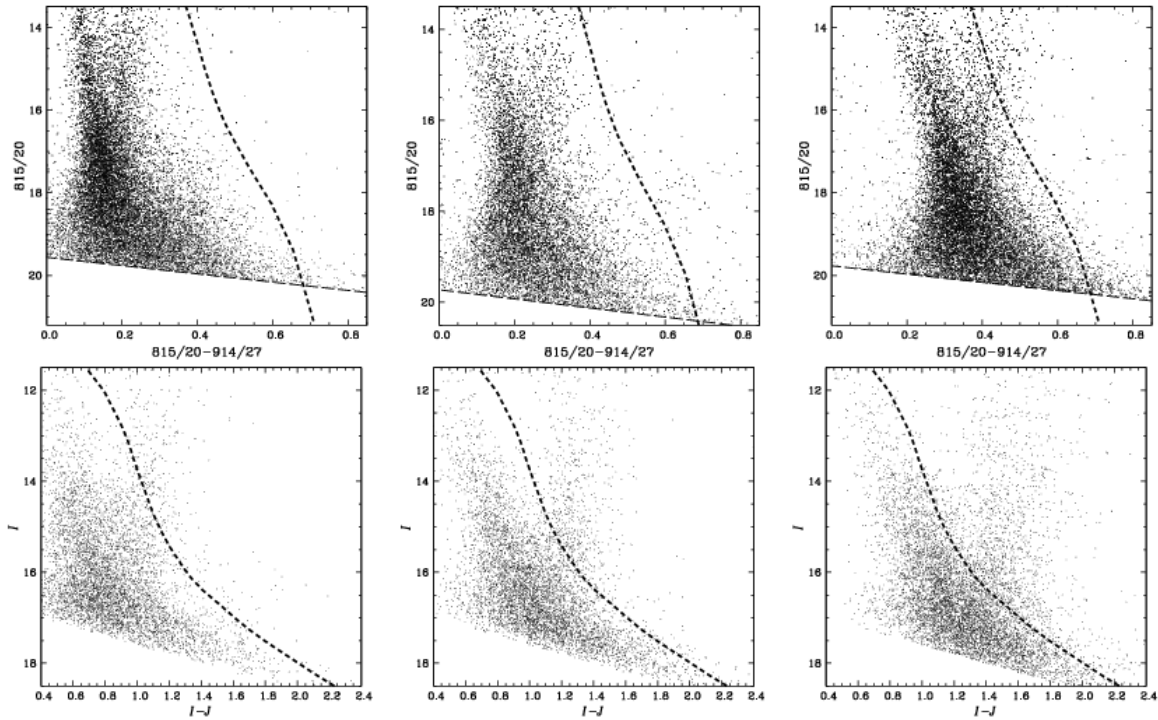
Figure 5.2 Colour-magnitude diagrams of 3 fields from our survey (*top*, from left to right, fields 40, 01 and 09) and 3 colour-magnitude diagrams from the same fields using DENIS data (*bottom*, *I* versus *I-J*). The IC 2391 isochrone is also shown. We clearly see a colour shift of the (field star) locus between these fields in our data, as well in the DENIS data.

We have computed the number of background red giants and M-dwarfs in the direction of IC 2391 to verify if all these objects could indeed explain the shift in colour we see. We assume that the space density of objects (ρ) drops exponentially with vertical distance from the disk (r) such that,

$$\rho(r) = \rho_0 e^{\frac{r}{r_0}}, \qquad (5.1)$$

assuming a scale height of $r_0 = 500\,\text{pc}$. We use the local space density (ρ_0) for late type giants of $2.5 \times 10^{-5}\,\text{pc}^{-3}$ (Loibl 1978) and for M dwarfs of $5.7 \times 10^{-2}\,\text{pc}^{-3}$ (from the *Research*
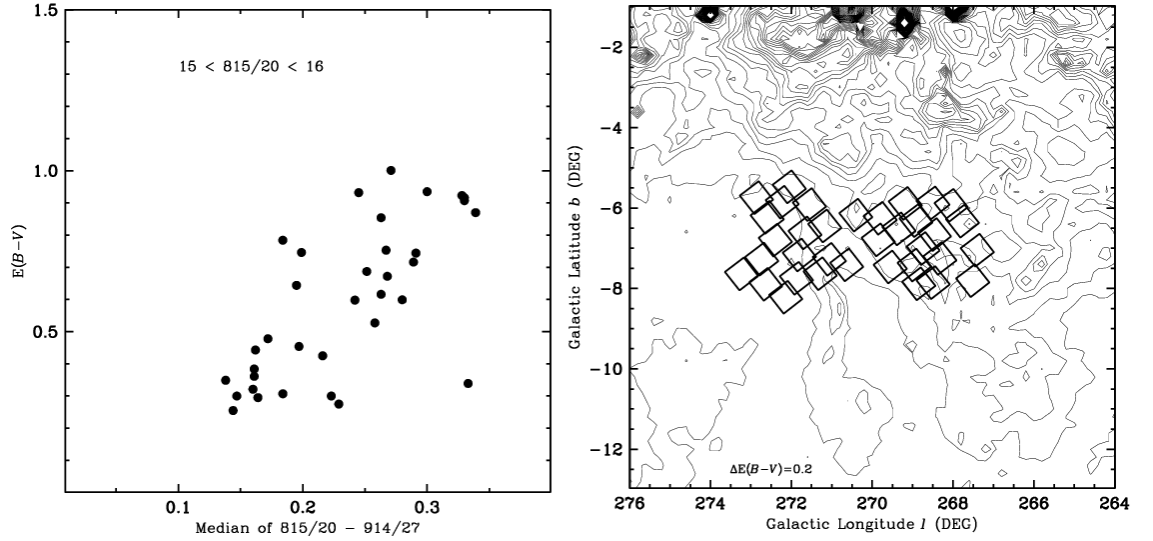
Figure 5.3 *Left.* $E(B - V)$ towards all our fields (from the Schlegel et al. 1998 extinction map) plotted against the median 815/20-914/27 stellar colour in those fields. *Right.* Position of the fields of our survey overplotted by the $E(B–V)$ extinction map of Schlegel et al. (1998). The contour separation is 0.2 mag.

Consortium on Nearby Stars, Henry et al. 2006). Using the 10σ detection limit in 815/20, we computed the maximum distance for which a M5V star and a red giant (using $\log g$ of 2.5, T_{eff} of 2000 K and a mass of $5.0\,M_\odot$, Hauschildt et al. 1999b) could be detected. From this we estimate that 2.4×10^6 M dwarfs and 3 120 red giants constitute the background of IC 2391 in our 10.9 sq. deg. survey (in the foreground of IC 2391, we estimate that there could be ~ 200 M-dwarf), which is on the same order of the number of all the objects we detected (1.7×10^6). Therefore, background red giants and M-dwarfs can explain the shift in colour we observe. This colour gradient of the background stars has not been reported in previous surveys of IC 2391 (Dodd 2004; Barrado y Navascués et al. 2001a; Patten & Pavlovsky 1999). It can be expected that Barrado y Navascués et al. (2001a) and Patten & Pavlovsky (1999) didn't observed such shift in color since their survey cover a smaller area (2.5 and 0.8 sq. deg. respectively) of the sky compaired to our 10.9 sq. deg. coverage.

5.1.2   Mass function for the outward fields and of the deep fields

Considering the fact that only three bands were used for the outward fields, and thus fewer constraints imposed, we expect that the number of photometric candidates would be larger per unit area than the other fields. The mass function (Figure 5.4) is similar to that of

the Galactic field (Chabrier 2003), however there is an overpopulation of low-mass objects (masses $\lesssim 0.05\,M_\odot$), a deficiency of objects in the mass range of 0.05 to $0.08\,M_\odot$, and again a clear overpopulation of stellar objects in the mass range of 0.5 to $0.8\,M_\odot$.
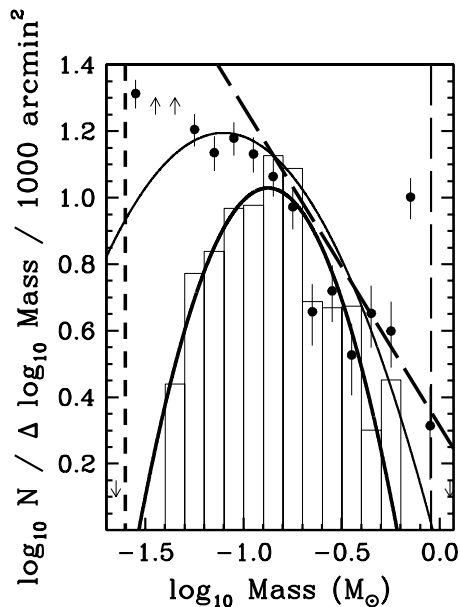
Figure 5.4 Mass function based on photometry for the outward fields. The mass function fit for IC 2391 from Barrado y Navascués et al. (2004a) and for the galactic field stars are shown as thick dashed and thin solid lines respectively. (Although the mass function from Barrado y Navascués et al. 2004a goes from 0.5 down to $0.03\,M_\odot$, the power law fit is valid only from 0.5 to $0.072\,M_\odot$.) The thick solid line is the fitted lognormal function of the mass function of IC 2391 (within 2.1°, see §5.1.3). Dots represent the mass function of the outwards field. Error bars are Poissonian arising from the number of objects observed in each bin. The histogram is the mass function for all fields within 2.1° of the cluster center (see §5.1.3). The vertical thin dotted line is the mass for which saturation start to occur in the short exposures and the 10σ detection limit is shown as a vertical dashed line. The total area covered by these 5 fields is $4\,767\,\mathrm{arcmin}^2$.

The mass function from the deep fields (Figure 5.5) agrees with the mass function of the radial fields within 2.1° from the cluster center in the mass range 0.05 to $0.1\,M_\odot$ and above $0.2\,M_\odot$. However, there is a clear overpopulation of substellar objects below $0.05\,M_\odot$.

The deficiency of objects in the mass range of 0.05 to $0.08\,M_\odot$ was also observed by Barrado y Navascués et al. (2004a), while the drop in the mass function is also reported for other clusters by Dobbie et al. (2002). They argue that the dust grains Al_2O_3, Fe and $MgSiO_4$ start to condense in the outermost layers of objects with $T_{\mathrm{eff}} \sim 1800\,\mathrm{K}$. The opacity
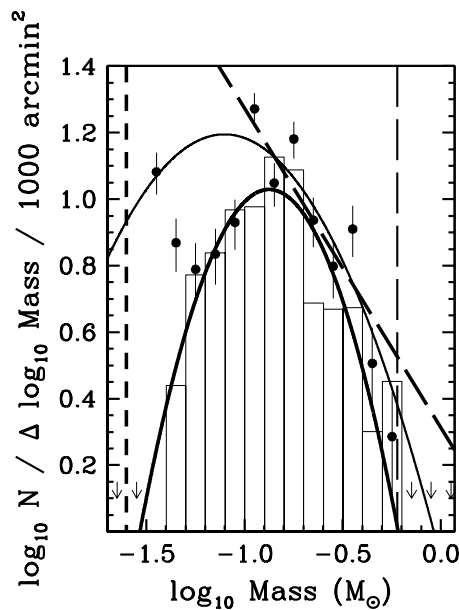
Figure 5.5 Same as Figure 5.4 but for the four deep fields. The total area covered by the 4 deep fields is 3 990 arcmin^2. The vertical thin dashed line is the mass range where saturation start to occur in the short exposures.

provided by dust would be enhanced and would be reflected in a drop of the luminosity function in the M7-M8 dwarf interval, and thus, in a dip in the derived mass function (because an incorrect Mass–Luminosity relation has been used). However, based on our isochrones, this phenomena would manifest itself in low-mass brown dwarfs with masses of $\sim 0.02\,\mathrm{M_\odot}$ while the deficiency we observe is at $0.05\,\mathrm{M_\odot}$ (corresponding to $T_{\mathrm{eff}}\sim 2700\,\mathrm{K}$). It is unlikely that this discrepancy is due to the uncertainties in the mass estimation since, at $\sim 0.02\,\mathrm{M_\odot}$ (1849 K), the error on the mass and effective temperature are $0.002\,\mathrm{M_\odot}$ and 77 K respectively (errors based on the uncertainties from the distance to IC 2391 and its ages), and $0.004\,\mathrm{M_\odot}$ and 46 K at $0.05\,\mathrm{M_\odot}$ (2682 K). Furthermore we only observe this effect in the mass function of the outward fields. We conclude that this drop is probably due to the selection procedure using only 815/20, 914/27 and J.

The rise of the mass function for objects below $0.05\,\mathrm{M_\odot}$ was also observed in IC 2391 by Barrado y Navascués et al. (2004a). In their work, the mass function was computed with objects that were selected as cluster members based on R_c, I_c, J, H and K photometry. Since their NIR photometry was from 2MASS, no data is available for objects fainter than $I_c \lesssim 19$ (10σ detection limit of 2MASS is at $J\sim 15.8$). As a result, their selection for fainter objects was based on R_c and I_c photometry only. In our case, although J band photometry is available for the outward fields, no R_c photometry is available. Like Barrado y Navascués

et al. (2004a), a shorter baseline is used for our membership determination in the outward fields. This situation is also observed in the mass function of the deep fields (where R_c band photometry is available, but no J band photometry). Only the fields observed with R_c and J (i.e. a longer baseline) show no significant rise of the mass function below $0.05\,\mathrm{M_\odot}$ (Figure 5.6). Since red giants were not observed in our spectroscopic follow-up of the two deep fields 15 and 20 (§5.2), we conclude that this increase is an artefact due to contamination by M-dwarfs. In this low-mass regime (for objects with mass $\lesssim 0.05\,\mathrm{M_\odot}$), a long spectral baseline (including, for instance, R_c and J) is needed to efficiently remove contaminations, as it allows a better determination of the energy distribution.
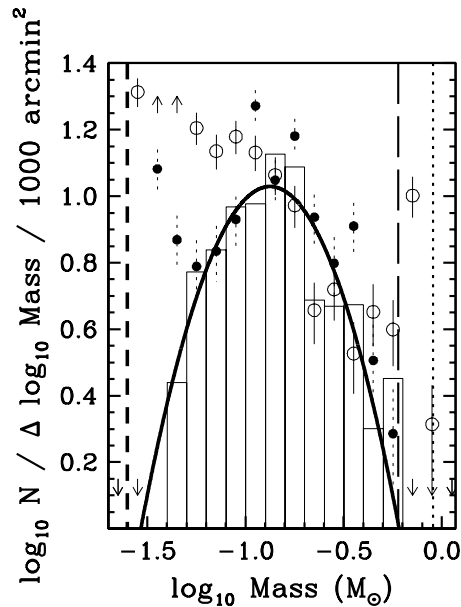
Figure 5.6 Filled dots represent the mass function based on the four deep fields (observed with the wide bands R_c and the medium band 770/19, 815/20, 856/14 and 914/27) and open dots represent the mass function based on the outward fields (observed with the wide band J and the medium bands 815/20 and 914/27). Also, we present again the 10σ detection limit, the mass function of all fields observed in R_c, 815/20, 914/27 and J within 2.1° from the cluster center and its lognormal fit. The vertical thin dotted and thin dashed line lines are the mass at which saturation started to occur in the short exposures for outward and deep field respectively.

The rise in the mass function over 0.5–$1.0\,\mathrm{M_\odot}$ is observed in all the radial fields but not in the deep fields (Figure 5.6). It is not possible to make a comparison of the previous determination of the mass function of IC 2391 from Barrado y Navascués et al. (2004a), since their mass function only extends up to $0.5\,\mathrm{M_\odot}$. However, other studies examined the stellar population of IC 2391 at higher masses. Dodd (2004) has computed the mass

function of this cluster from 0.1 to $10\,\mathrm{M_\odot}$, while Patten & Pavlovsky (1999) have obtained the luminosity function of IC 2391 from M_V=-2 to M_V=14 (which correspond to a mass range from 10 to $0.085\,\mathrm{M_\odot}$ in IC 2391). From Dodd (2004), the number of objects detected at $\sim$$0.5\,\mathrm{M_\odot}$ (M_V=9.68 based on our isochrones) is higher than the power law mass function, while for Patten & Pavlovsky (1999), no significant rise is observed at that mass range. The rise of the mass function over 0.5–$1.0\,\mathrm{M_\odot}$ is also observed in other open clusters. In a study of the stellar populations of the Praesepe and Coma Berencies clusters, Kraus & Hillebrand (2007) present a mass function for Coma Berencies with more objects in the mass bin 0.6–$0.9\,\mathrm{M_\odot}$ than in neighbouring bins. However, this is not observed in the mass function they derive for Praesepe. Deacon & Hambl (2004) present the mass function of two other open clusters, α Per and the Pleiades. The number of objects from $0.5\,\mathrm{M_\odot}$ to $1.0\,\mathrm{M_\odot}$ for the Pleiades and at $0.8\,\mathrm{M_\odot}$ for α Per is also larger than the fitted mass function (lognormal and power law fit respectively).

Jeffries et al. (2004) present the mass function of the open cluster NGC 2547 and also noticed a rise in the 0.7–$1.0\,\mathrm{M_\odot}$ interval. This rise, also observed in the luminosity function as a large peak at $12 \lesssim I_c \lesssim 14.5$, is attributed to contaminating background giants by Jeffries et al. (2004). This would be consistent with the fact that this bump is also observed in the other radial fields (see Figure 5.7) but not in the deep fields (Figure 5.5, where the use of medium bands were successful in removing red giant contaminants, as we will see in the spectroscopic follow-up in §5.2). Indeed, as we discuss later in §5.2, red giants were not found in our spectroscopic follow-up, confirming that the use of medium bands such as 770/19, 815/20, 856/14 and 914/27, and theoretical colours (Hauschildt et al. 1999b) are effective when removing background red giants. However, from the mass function of the radial fields (including the outwards fields), the medium filters 815/20 and 914/27 alone, combined with wide band R_c and/or J, are less efficient at removing background giants.

5.1.3 Radial variation of the mass function at the stellar and very low-mass star regime

At first glance, we can see in Figure 5.7 that the two mass functions within 2.1° are similar to each other. Although they present a number of objects different in the mass range below $0.15\,\mathrm{M_\odot}$ and above $0.3\,\mathrm{M_\odot}$, we consider those differences (between the two mass functions within 2.1°) not significant compared to the difference observed with the mass function computed from the fields at the edge of IC 2391 (out of 2.1°). Indeed, the mass function for θ>2.1° shows a significant deficiency of stellar objects from 0.1 to $0.3\,\mathrm{M_\odot}$ compared to the mass function from the inner part of the cluster, whereas outside of this mass range there is no change with radius. In Figure 5.8 we present the cumulative function from the same

three areas of the cluster presented in Figure 5.7. A Kolmogorov-Smirnov test performed on the distributions indicates that there is a $1.1 \cdot 10^{-5}\,\%$ probability that the population at $\theta > 2.1°$ is the same as that at $\theta < 2.1°$. We can see from Figure 5.8 (*left*) the absence of objects at $\sim 0.15\,M_\odot$ and the slow increase of the cumulative fraction until 0.3–$0.4\,M_\odot$ for the population at $\theta > 2.1°$. We also present in Figure 5.8 (*right*) the radial profile of IC 2391 based on our survey and its King profile fit (King 1962), where the fit gives us a maximal number density at the center of 112.7 members per 1 000 arcmin^2 and a full width at half maximum of $2.19°$ (or 1.9 pc). Although a King profile does not fit the radial profile of the cluster well, we use this profile because such an empirical law can reproduce the cluster population including globular clusters, galaxies clusters and dwarf elliptical galaxies (King 1962).
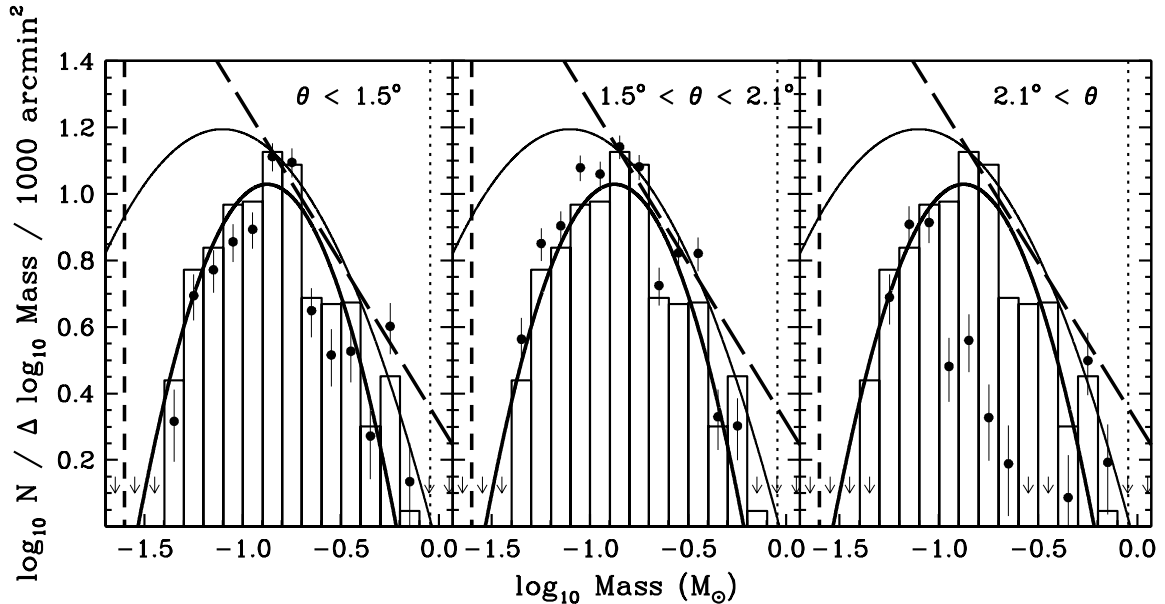
Figure 5.7 Same as Figure 5.4 but for all radial fields. Dots in each panel represent the mass function of (*left*) fields within $1.5°$ of the cluster center, (*center*) fields within the annulus from $1.5°$ to $2.1°$ and (*right*) the mass function of fields outside $2.1°$. Error bars are Poissonian arising from the number of objects observed in each bin. The histogram is the mass function for all fields within $2.1°$ of the cluster center and its best fit of a lognormal function is given by the thick solid line. (The total area covered for each panel, from left to right, is 6 637, 9 539 and 5 609 arcmin^2.) For reference, the ordinate value of 1.23 for the the bin at $\log_{10} M = -0.8$ ($0.14\,M_\odot$), the histogram peak, corresponds to 137 objects.

We observe a significant number of objects in the 0.5–$0.7\,M_\odot$ interval in the edge of the cluster ($\theta > 2.1°$). In §5.1.2, we also noted a rise in the number of objects in the mass range of 0.5–$1.0\,M_\odot$ in the fields observed only in the wide band J and in the medium
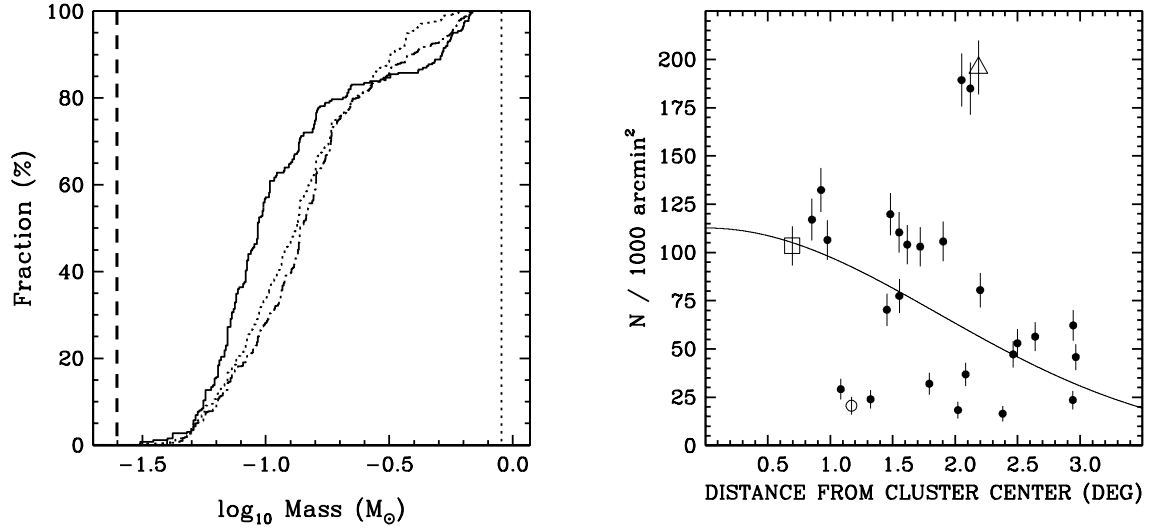
Figure 5.8 *Left.* Cumulative number of cluster members within 1.5° (dash-dotted line), within the annulus from 1.5° to 2.1° (dotted line) and outside of 2.1° (tick line). The 10σ detection limit is shown as an horizontal dash line. The vertical thin dotted line is the mass for which saturation start to occur. *Right.* Radial profile of IC 2391 with a King profile fit (King 1962). The deep fields are represented with *open square*, the outward fields are represented by *open triangle* and all radial fields are represented by *filled dots*. (The *open dot* represent the field 24, which is the only fields where short exposures are not available.)

bands 815/20 and 914/27. We have concluded that this range of masses is subject to significant contamination by red giants. Therefore, no conclusion should be made on the radial variation of the mass function in this mass interval.

A further interesting variation is the lower mass function over the mass range 0.15 to $0.3\,\mathrm{M_\odot}$ compared to lower masses, for the edge of the cluster ($\theta > 2.1°$). Our estimation of the relaxation time of IC 2391 is $t_{relax} \sim 105\,\mathrm{Myr}$, so for this 50 Myr cluster, mass segregation via dynamical interaction might have started to occur in IC 2391.

This situation is also observed in other clusters at a similar age of IC 2391. In a study of the low-mass stars and brown dwarfs mass functions in this cluster, Jeffries et al. (2004) have observed evidence for mass segregation in NGC 2547 (age$\sim$30 Myr). Sirianni et al. (2002) observed mass segregation in NGC 330 (age$\sim$30 Myr) and believed it would be of a primordial nature rather than from dynamical evolution. Their conclusion is based on the fact that NGC 330 is 10 times younger than its relaxation time. Our estimations of the lower limit of the relaxation time of IC 2391 is $t_{relax} \sim 105\,\mathrm{Myr}$. In this situation, the mass segregation could not be primordial, since the cluster would have to undergo significant

dynamical evolution. However, if we assume that *all* our photometric candidates are cluster members, we would then have a relaxation time of $t_{relax} \sim 1.6\,\mathrm{Gyr}$. Therefore, we can't draw any conclusions on the primordial status ot the mass segregation observed in IC 2391 based on the relaxation time.

Since we have few fields beyond the tidal radius of IC 2391 (7.38 pc, Piskunov et al. 2007, which correspond to 2.89° from the cluster center), we cannot directly address the issue of evaporation (already a difficult task in such a low latitude field without kinematics). However, the comparison of the distribution of the stellar population with masses of 0.08–0.15 $\mathrm{M}_\odot$ to the stellar population with masses of 0.15–0.3 $\mathrm{M}_\odot$ leads us to conclude that mass segregation has occured in IC 2391.

5.1.4   Radial variation of the mass function at the brown dwarf regime

For each panel in Figure 5.7, the lowest bins with detected objects are centered at 0.032 $\mathrm{M}_\odot$ (3 objects detected with $\theta<1.5°$), 0.020 $\mathrm{M}_\odot$ (2 objects detected within $1.5°<\theta<1.5°$) and 0.032 $\mathrm{M}_\odot$ (3 objects within $2.1°<\theta$).

We previously estimated that the escape velocity of IC 2391 was $v_e =0.4\,\mathrm{km/s}$ (with a crossing time of $t_{cross} =17.4\,\mathrm{Myr}$). If *all* brown dwarfs were systematically formed by the ejection scenario and stars formed from the fragmentation of a dense molecular cloud, with a high velocity dispersion of $\sim 2\,\mathrm{km/s}$ for brown dwarfs (Kroupa & Bouvier 2003), one would expect to see the mass function significantly dropped in the brown dwarfs regime compared to the very low-mass star regime, since the ejection of brown dwarfs would be more efficient then stars (very low-mass stars and more massive objects). In none of our mass functions do we observe a discontinuity at the stellar to substellar boundary (around 0.072 $\mathrm{M}_\odot$), suggesting that the ejection scenario alone is not a sufficient formation mechanism for brown dwarfs in IC 2391 if substellar objects have higher velocity dispersion than stars (Kroupa & Bouvier 2003). However, if all brown dwarfs were formed using this mechanism, then the velocity dispersion of stars and brown dwarfs should be similar, as suggested by Bate et al. (2003).

Just as the very low-mass star population, brown dwarfs are also observed in the area beyond 2.1° from the cluster center. Nonetheless, a comparison of the mass function of IC 2391 with that of the Galactic field shows a deficiency of brown dwarfs at this radius. In comparison with the fitted mass function of the Pleiades (age $\sim 120\,\mathrm{Myr}$) and the Hyades (age $\sim 625\,\mathrm{Myr}$), this deficiency increases proportionally with age, as one would expect due to dynamical evolution. Although this absence of radial variation of the brown

dwarf population is in agreement with the ejection scenario as a formation mechanism of brown dwarfs (Muench et al. 2003, Kumar & Schmeja 2007), the comparison of the mass function on each side of the stellar to substellar boundary and the increase of the brown dwarfs deficiency proportionally with age do not allow us to conclude that the ejection formation scenario is a dominant formation mechanism of brown dwarfs (if these objects have a high velocity dispersion). We rather conclude that, the fact that we do not observe a discontinuity in the mass function across the stellar/substellar boundary ($0.072\,\mathrm{M_\odot}$) implies that the ejection formation scenario is not a significant brown dwarf formation mechanism in this cluster, if this formation mechanism results in a higher velocity dispersion of brown dwarf compared to stars. On the other hand, if the ejection mechanism is a dominant brown dwarf formation path in this cluster, then both brown dwarfs and stars should have the same velocity dispersion. These observations also support our previous conclusion that mass segregation has started to occur in IC 2391 and that dynamical evolution is responsible for the distribution of the stellar and substellar objects in this cluster.

5.2 Spectroscopic results

Here we present the results of a preliminary spectroscopic follow-up of some photometric candidates. As explained in the previous section, the main sources of contamination in our photometric selection are background red giants and field M-dwarfs. We have also shown in §5.1.1 that, due to extinction, background contamination is non-uniform. We therefore need to refute or confirm membership status with optical spectra. For this task we used the fibre spectrograph HYDRA. Fibre overlap is not possible with this instrument, thus not all candidates in a field could be observed. However, it is our intention to eventually obtain spectra of all candidates. The data reduction, the spectral type and luminosity class determination were presented in §3.3. The spectroscopic effective temperature was obtained using the spectral type and the temperature scales of Luhman (1999) while each mass was derived from the effective temperature using our isochrone for IC 2391. We discuss membership determination based on optical spectra below in §4.2.

We have obtained a total of 70 spectra in field 15 (35 for which the SNR is higher than 5) and 50 from field 20 (42 with a SNR higher than 5). Spectra with a SNR below 5 are not used in the following analysis. Table 5.3 provides the derived parameters (spectral type, T_{eff} and mass) and the signal-to-noise ratio (SNR). Objects are given the notation IC 2391-HYDRA-ZZ-YY where ZZ is the field number and YY a serial identification number (ID). Table 5.4 gives details of the three objects confirmed as cluster members by Barrado y Navascués et al. (2004a) for which we also have spectra.

In Table 5.5 we again present all objects from Table 5.3, but with physical parameters and with membership status based on photometry and spectroscopy (i.e. which satisfy our spectroscopic criterium). We don't reject objects below which does not present a feature of LiI due to low SNR if the other criteria are satisfied (e.g. IC2391-HYDRA-15-19).

5.2.1   Hα contamination

We mentioned in §3.3 the presence of contamination at Hα in sky spectra. As these spectra are used for background subtraction (we have fibre spectra), there are potential difficulties in measuring the stellar Hα line. We now discuss this issue.

In producing a high-resolution atlas of night-sky emission lines with the Keck echelle spectrograph, Osterbrock et al. (1996) observed an Hα emission line at high Galactic latitudes which they concluded was due to diffuse interstellar gas emission (the closest atmospheric emission observed were two OH lines at 6553.617 Å and 6568.779 Å). From the AAO/UKST SuperCOSMOS Hα Survey (SHS, Parker et al. 2005), we have also noticed high variations of Hα emission at low galactic latitude. We used the SHS to estimate the Hα emission at each position of our sky fibers (by taking a median of the flux over a 200 x 200 arcsec window). The frames are flat-field corrected but not flux calibrated, so we retain the unit of (photon) counts. In Figure 5.9 we plot this against the flux (in counts) of the Hα emission line of our background spectra for field 20. While there is no strong evidence for a correlation, we nonetheless see a significant variation of the Hα emission. As this clearly prevents a reliable background subtraction of the Hα line, we choose not to draw any conclusions on membership status based on this line. We must therefore question its use by Barrado y Navascués et al. (2004a) for this purpose (who used the same instrument for the same cluster). For further observations of objects in the direction of IC 2391 using fiber-fed spectrograph, we recommend background subtraction to be performed in a similar way as the one done by Carpenter et al. (1997), where the same fibers for the science targets were also used for sky subtraction but shifted 6 arcsec away.

5.2.2   Discussion of the spectral data

Of the 61 photometric candidates observed with a SNR higher than 5, 19 are spectroscopic members of the cluster. Of these 19 objects, 12 have a derived spectroscopic mass $\lesssim 0.072\,M_\odot$ while for higher mass objects contamination is much larger, with just 7 out of 39 photometric candidates passing all of our spectroscopic criteria. We find no red giants in our spectral sample, which demonstrates that our choice of filters and selection proce-
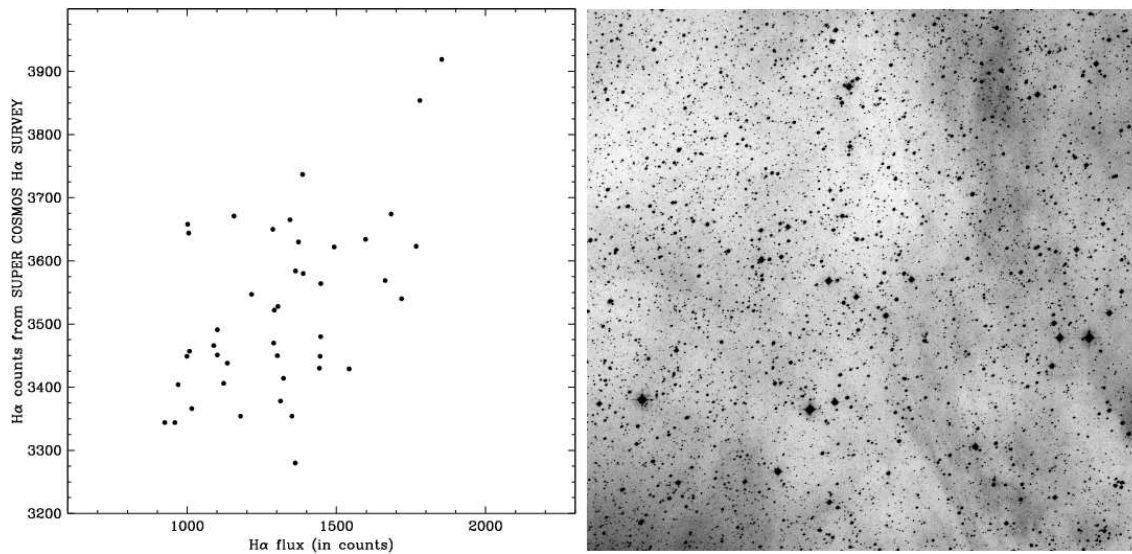
Figure 5.9 *Left.* Hα emission (median counts) in fields of size 200 x 200 arcsec from the SuperComsos Survey at the location of our sky fibres, plotted against the flux (in counts) of the Hα emission line we measured in our sky fibers in the HYDRA pointing of field 20. *Right.* Hα observations from SuperCOSMOS towards field 20 (images of 35×35 arcmin).

dure is highly efficient at minimizing this contamination. Since our spectroscopic follow-up covers only part of the mass range used for the mass function calculation in §5.1.2, it is not possible to compute a new mass function with corrections applied at each mass bin. It is expected that the contamination rate would be different for other mass range and fields (for different filter combinations). However, if we crudely assume that just 19 out of 61 photometric candidates are true cluster members and apply this correction to all fields and masses, we can rederive a mass function and refit a lognormal. The mass function of IC 2391 would then be reduced by $\log_{10}(19/61)$ to $k=3.33$ in eq. 2.4 (m_0 and σ are of course unchanged).

Three of our spectral targets were observed by Barrado y Navascués et al. (2004a) (CTIO-49, CTIO-62 and CTIO-41 are named in our survey as IC2391-HYDRA-15-02, IC2391-HYDRA-20-02 and IC2391-HYDRA-20-03). For IC2391-HYDRA-15-02 we do not assign spectroscopic membership since there is a large disagreement between the photometric T_{eff} and mass (3158 K and 0.13M$_\odot$) compared to those determined spectroscopically (2840 K and 0.065 M$_\odot$). However, we agree with Barrado y Navascués et al. (2004a) on the status (cluster membership) of the other two.

We present in Figure 5.10 the mass function based on the spectroscopic mass. There is no agreement with the photometric mass function of the deep fields, either with the lower
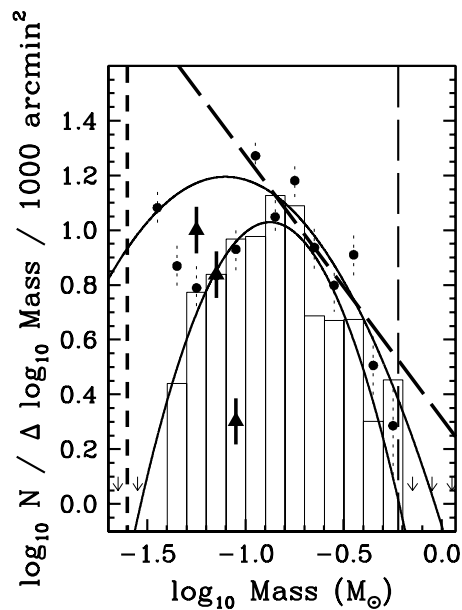
Figure 5.10 Same as Figure 5.5 but the triangles represent the mass function from our spectroscopic data. The spectroscopic mass function was normalized to the mass function of the deep field at the bin of $0.056\,M_\odot$. Only three mass interval have candidate member (in the other bins, there are no objects). There is no agreement between the photometric mass function of the deep fields with the spectroscopic mass function, but this is an artefact due to the spectroscopic selection.

or higher mass interval. However, it is not too surprising that both the photometric and spectroscopic mass function are not in agreement. Indeed, the spectroscopic follow-up with hydra was done for objects *only* below $0.2\,M_\odot$ (at -0.7 in logarithmic scale) and brighter then $815/20 = 19$, and we have shown that contamination is important at the low-mass end of the mass function because of field M-dwarf contaminants (smaller baseline for deep field and outward fields, §5.1.2). Moreover, since it was possible to give a priority on the fiber allocation with hydra, the fibers were allocated in priority to brown dwarf candidates. Therefore, no conclusions should be made from this spectroscopic mass function since this disagreement is an artefact of the spectroscopic selection. However, it is our future plan to obtain spectra for all our photometric candidates.

5.2.3   Discovery of new brown dwarf members of IC 2391

Of the 61 spectral targets, we assigned as seven brown dwarfs in IC 2391, on the basis of spectroscopic confirmation, and having both photometric and spectroscopic masses below
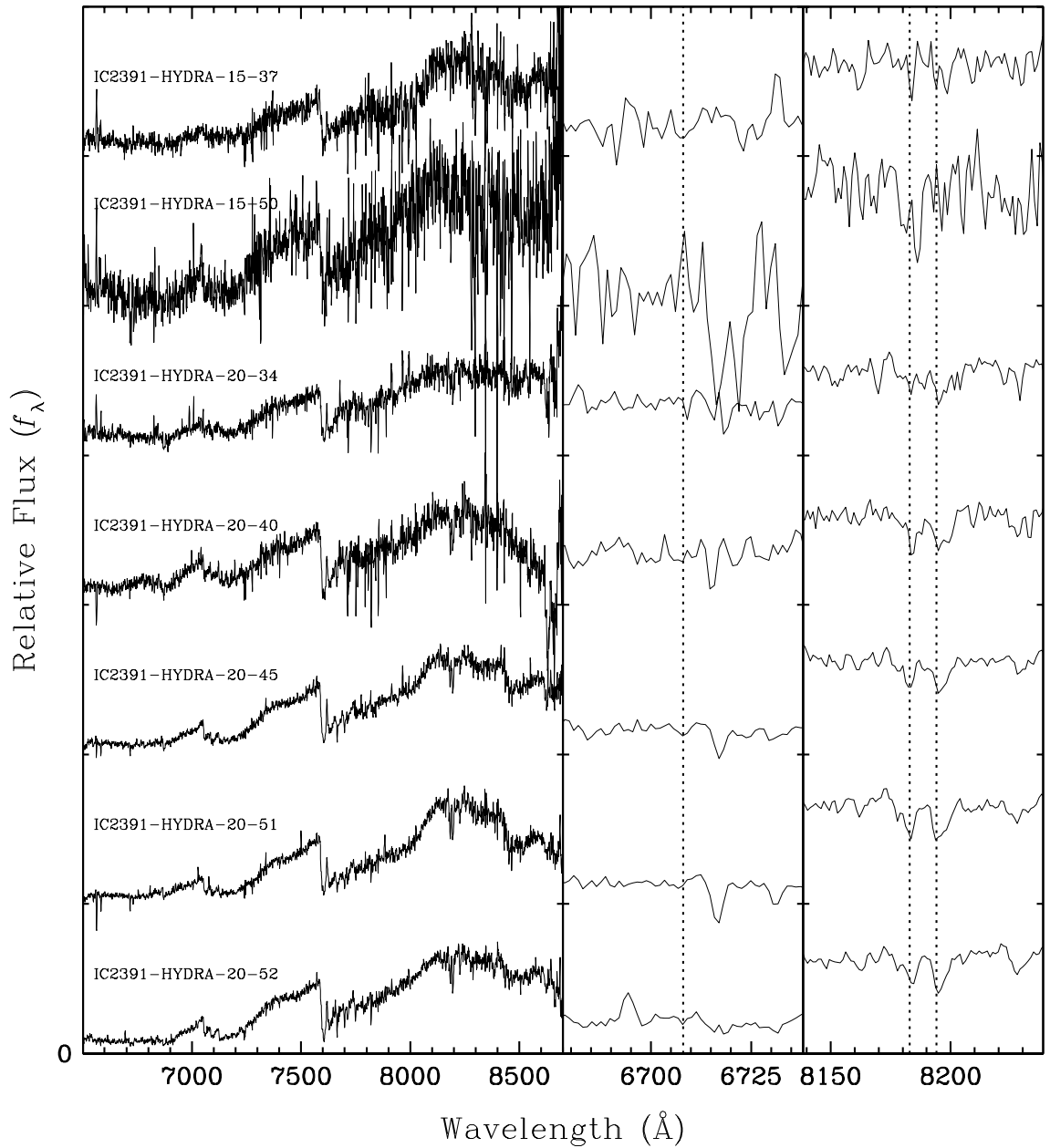
Figure 5.11 Spectra of the seven newly discovered brown dwarf members of the IC 2391 cluster found in our survey. For each spectra, we also present a new close-up on the Li and the NaI doublet.

0.072M$_\odot$. These are new discoveries. These objects are IC2391-HYDRA-15-37 and -50 in field 15 and IC2391-HYDRA-20-34, -40, -45, -51 and -52 in field 20. Table 5.6 lists their parameters, Figure 5.11 shows their spectra and Figure 5.12 contains the finding charts.
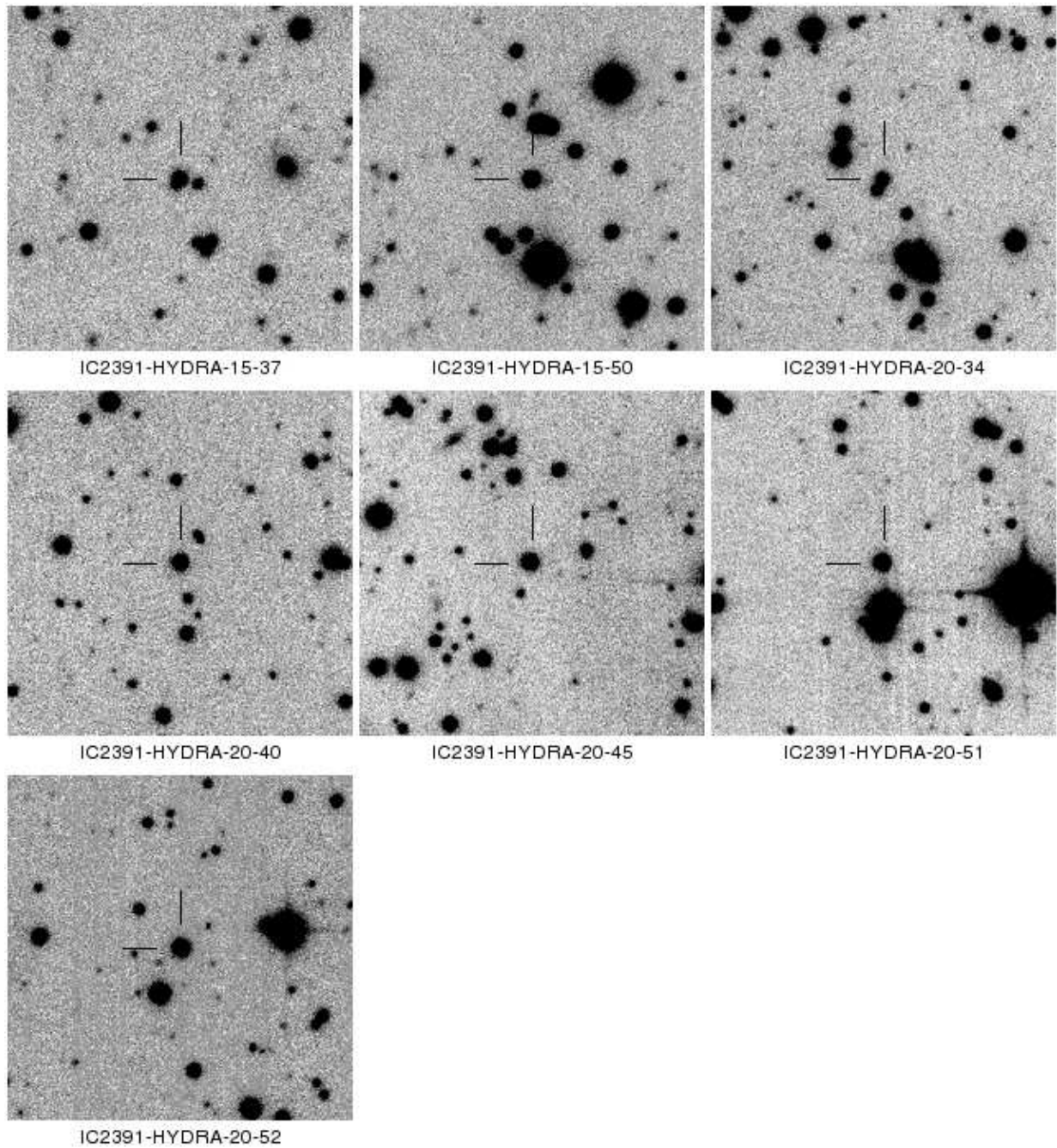
Figure 5.12 Finding charts of the seven new brown dwarf members of IC 2391 (from 815/20 images). The panels are 3.5×3.5 arcmin with north up and east to the left.

We can see in Figure 5.11 that Hα is only visible in IC2391-HYDRA-20-34 ($W = 7.5 \pm 0.5$), therefore all other objects would be designated as non-members by Barrado y Navascués et al. (2004a). Considering that the mass function from our radial fields is similar for the

deep fields in the mass range of these seven new objects (from 0.045 to $0.07\,\mathrm{M}_\odot$), we expect that seven brown dwarfs in the same mass range can be found in the other two fields and up to 38 in all the radial fields, using the same selection and fibre assignment.

5.3   2MASS data on IC 2391

Here, we want to analyse data from 2MASS in order to (1) have a uniform sample, where the same instrument and telescope setup is used, and (2) where the sample of data is obtained and reduced independently from our work. For these reasons, we will only use 2MASS data and will not combine it with our optical photometry or data from another public survey (such as DENIS). We use the online general catalog query engine *Gator* [1] from 2MASS to obtain the J, H and K_s band photometry for all point sources in a square of 6° x 6° centered on RA=08:40:36 DEC=-53:02:00, which gives us a total of about 1 million objects. The 10σ detection limit in the three bands are J=15.8, H=15.1 and K_s=14.3 (280 817 objects are brighter), which does not reach the same limit of our survey at $0.03\,\mathrm{M}_\odot$ (the 10σ detection limit of 2MASS at J=15.8 gives M∼$0.055\,\mathrm{M}_\odot$ based on our isochrones of IC 2391). Saturation in the 2MASS atlas images occurs at approximately J=9.0, H=8.5 and K_s=8.0, which corresponds to a mass of $1.2\,\mathrm{M}_\odot$. However, this detection limit will be sufficient in order to confirm (1) the absence of radial variations of the mass functions on each side of the stellar/substellar boundary and (2) the mass segregation observed with its signature on the mass function over the mass range 0.15 to $0.3\,\mathrm{M}_\odot$.

The selection procedure performed is similar to the selection procedure we presented in Chapter 4. First, candidates were selected based on colour-magnitude diagrams using the JHK_s band photometry. We present in Figure 5.13 the three colour-magnitude diagrams used for this selection step. A total of 16 955 objects pass this selection step (94% objects rejected). Here, we point out that the selection region will also yield many contaminants from the disk in the red clump of stellar evolution, as the right-hand structure in the top two colour-magnitudes diagrams in Figure 5.13 are stars at the red clump of stellar evolution (while the left-hand side structure are stellar objects from the Galactic thin disk). Afterwards, we used colour-colour diagrams as in §4.1.2. Among the objects from the first selection, 13 122 pass the second selection (23% rejected). It is not be possible to perform a rejection of contaminants based on proper motion such as we did in §4.1.3 since there is no proper motion data available with 2MASS. The final selection procedure was done with the rejection of objects based on observed magnitude vs. the predicted magnitude discrepancy (§4.1.3), where the normalization was done using the K_s band. We obtained a

---

[1]http://irsa.ipac.caltech.edu/cgi-bin/Gator/nph-scan?submit=Select&projshort=2MASS
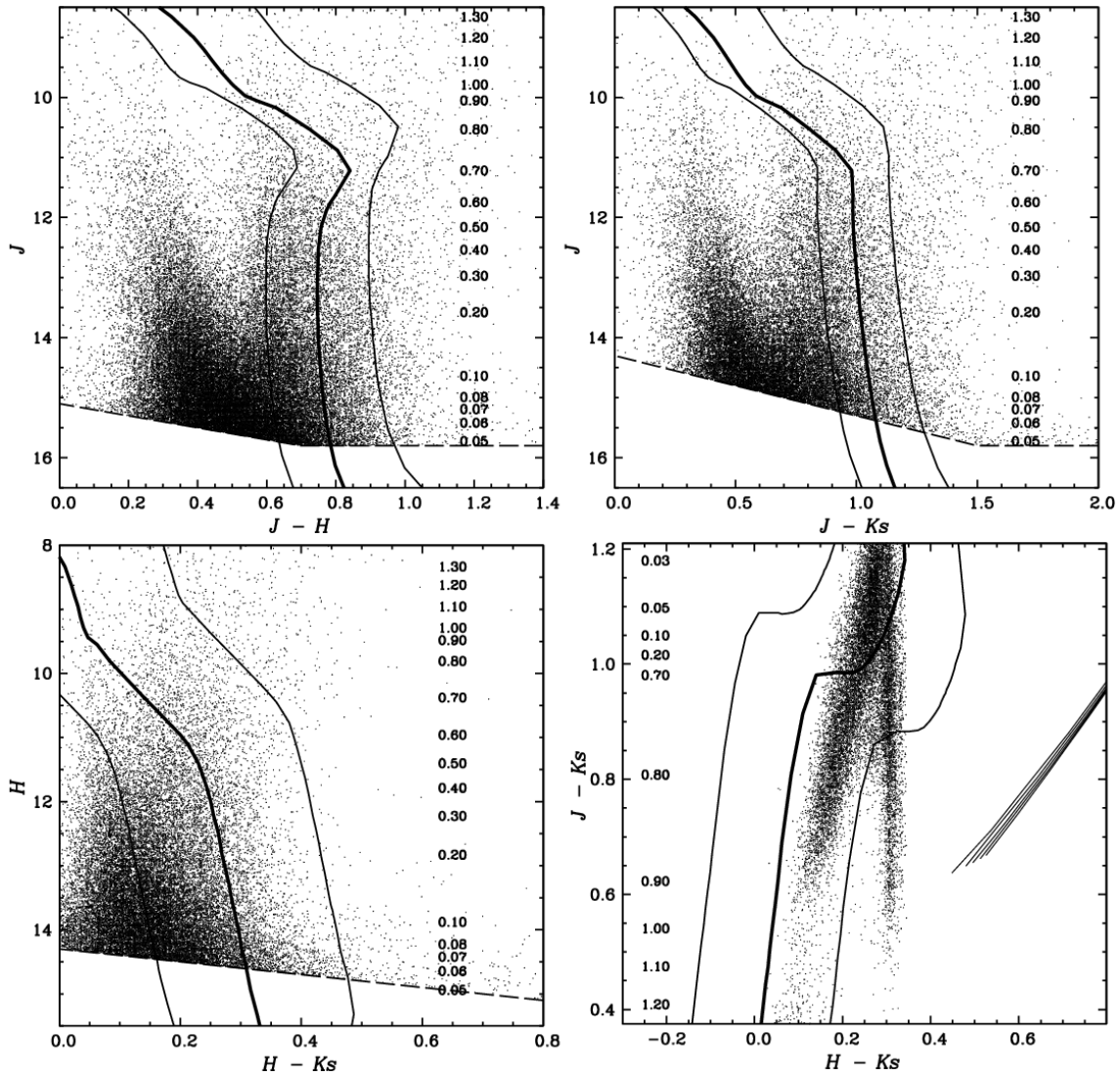
Figure 5.13 *Top two panels and lower left.* Colour-magnitude diagrams from 2MASS data. As thick lines we show the isochrone computed from an evolutionary model with a grainless atmosphere (NextGen model, the masses are shown on the right). The thin dashed line is the 10σ detection limit. In each panel, the thin solid line defines the selection region. (For clarity, only one object out of nine is shown.) *Lower right.* Colour-colour diagram from 2MASS data. The thick and thin line are the same as for the colour-magnitude diagrams and masses are shown of the left. The very thin grid on the right represents colours of red giants (such as presented in Figure 4.2 of §4.1.2). We can see that with JHK_s photometry there is no overlap between the red giant colour grid and the isochrones of IC 2391.

final list of 855 candidates from 2MASS based on our selection procedure using the JHK_s photometry.

In Figure 5.14 we present the mass function of IC 2391 based on our selection. This Figure is divided into the same areas as presented in our analysis in §5.1.3: within 1.5° of the cluster center, within the annulus of 1.5° to 2.1° and beyond 2.1°. Overplotted is the mass function we have obtained for IC 2391 from our data for the same radial distance with number of objects per 1000 arcmin². (The mass function of IC 2391 based on 2MASS data was normalized to the mass function based on our data, within 1.5°, in order compare more easily.) The mass function presented here has several disagreements with the mass function we have presented in Figure 5.7. First of all, the mass function derived with 2MASS data does not agree with the shape that we find for IC 2391 based on our data. Secondly, based on the selection procedure for 2MASS, there are no objects that belong to IC 2391 more than 2.1° away from the cluster center, which is in disagreement with our survey (there is 773 objects within 1.5° and 122 objects within the annulus from 1.5° to 2.1°). Finally, although we can observe a radial variation of the stellar population, we do not observe a clear indication of mass segregation.

The disagreement between the mass function obtained with our optical survey and with 2MASS data is further observed in the cumulative function and radial profile of IC 2391 (Figure 5.15). The panel on the left shows the cumulative number of cluster member within 1.5° and within an annulus of 1.5° to 2.1° from the cluster center, while the panel on the right gives the radial distribution for all the candidates. For the candidates with a mass above and below $0.5\,M_\odot$, we can see that the radial distribution is similar, regardless of their mass. Furthermore, we have performed a Kolmogorov-Smirnov test for these two distributions and there is a 79.4% probability that the two populations heavier or lighter than $0.5\,M_\odot$ are similar.

We attribute such discrepancies to the fact that there is a low sensitivity in the energy distribution in JHK_s bands from $1.4\,M_\odot$ down to $0.03_\odot$. This is illustrated in Figure 5.16, where we can see that variations in colours with effective temperatures are not as high as for colours with the red optical band, such as R_c–J and 770/19–914/27, with variations as high as 4 magnitudes (as we have seen in Figure 4.3 in §4.1.2). This was also our conclusion with the three synthetic spectra in Figure 3.2 of §3.1.1. Indeed, we can see from Figure 5.16 that the variation from the 10σ detection limit of 2MASS at $0.055\,M_\odot$ ($\sim$2750 K) to the region we observed mass segregation, which is at to $0.7_\odot$ ($\sim$3900 K), is basically below 0.2 dex. This compares to 1.5–4 dex for R_c–J (Figure 4.3, §4.1.2).

Considering the low sensitivity with JHK_s only, we will again obtain the mass functions at different radii, the cumulative functions and the radial distributions, by (1) using J band
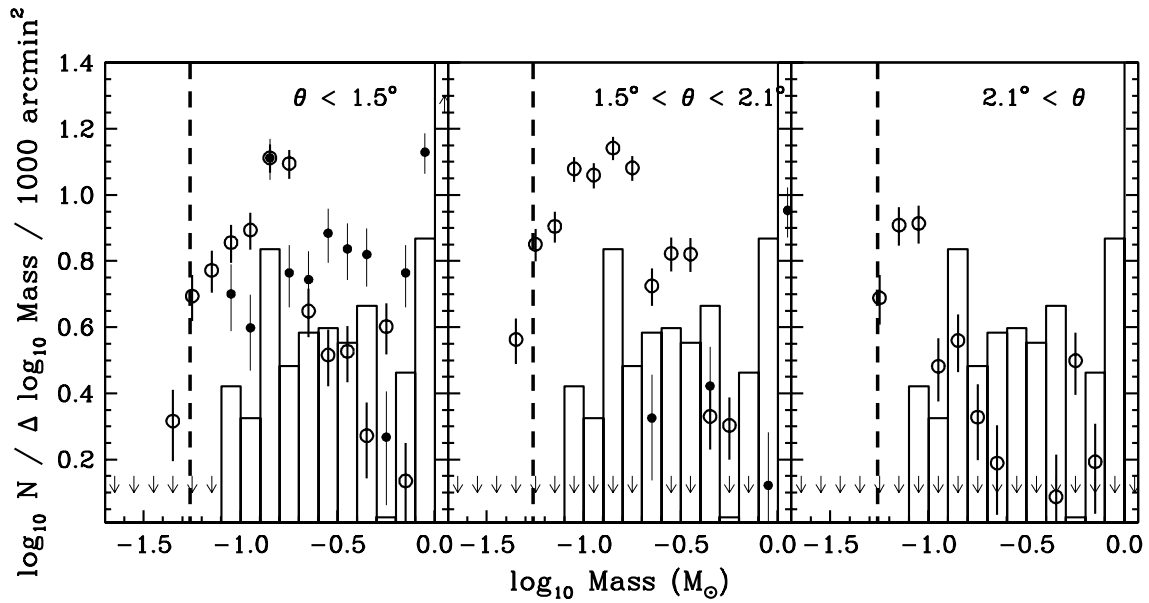
Figure 5.14 This Figure is similar to Figure 5.7 in §5.1.3. Filled dots in each panel represent the mass function of (*left*) all objects within 1.5° of the cluster center, (*center*) within the annulus from 1.5° to 2.1° and (*right*) more then 2.1° away from cluster center. Error bars are Poissonian arising from the number of objects observed in each bin. The histogram is the mass function for all objects within 2.1° of the cluster center and we present as open circles the mass function from our data in each area of the cluster (within 1.5° from cluster center, within the annulus from 1.5° to 2.1° and more then 2.1° away). The mass function of IC 2391 based on 2MASS data was normalized to the mass function based on our data, within 1.5°, at the $\log_{10}M = -0.75$ mass bin ($M = 0.18\,M_\odot$), for ease of comparison.

only for the mass determination and (2) no rejection of objects based on the observed vs. predicted magnitude discrepancy, since this require an estimation of mass and effective temperature based on the energy distribution. The new mass functions are presented in Figure 5.17 (division similar to Figure 5.14) while new cumulative functions and radial profiles of IC 2391 are presented in Figure 5.18. These objects are cluster members based only on colour-magnitude and colour-colour diagrams, which gives a total of 13 122 objects.

Although we observe similarities with the mass function of IC 2391 based on our data (a maximum at ∼0.18 $M_\odot$ and the sudden drop at 0.2 $M_\odot$), there is obviously an over contamination above 0.3 $M_\odot$. This is further illustrated in the right panel in Figure 5.17 which shows a mass function with each bin above 0.1 $M_\odot$ containing more than 50 objects. This is also confirmed by the sudden increase of the cumulative function at 0.5$M_\odot$ and the constant increase of objects with masses above 0.5 $M_\odot$ in the radial plot. We therefore
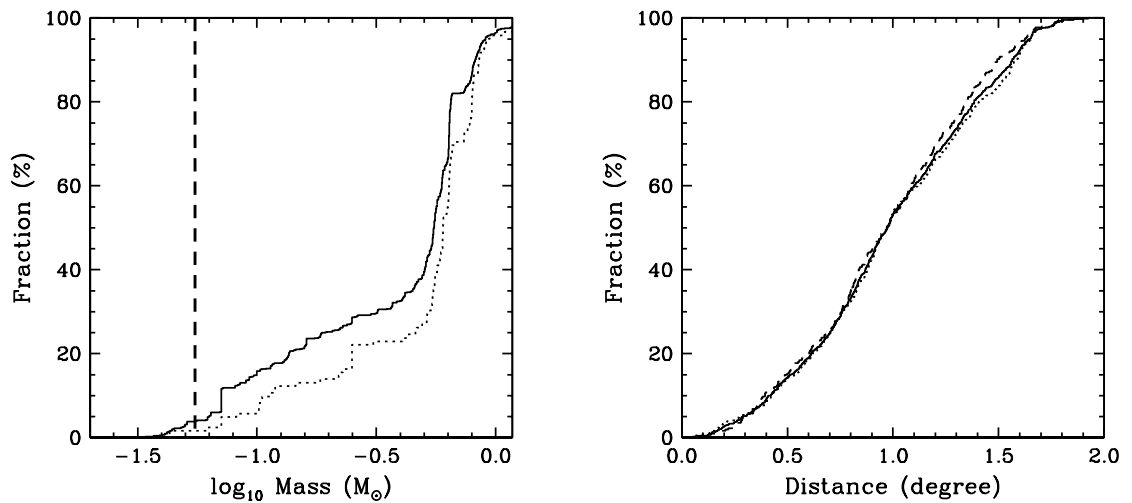
Figure 5.15 Cumulative function and radial profile of IC 2391 based on $JHK_{\rm s}$ photometry from 2MASS. *Left.* Cumulative number of cluster members within 1.5° (filled line) and within the annulus from 1.5° to 2.1° (dotted line). The 10σ detection limit is shown as an horizontal dashed line. *Right.* Radial profile of IC 2391 with all objects (thin line), objects with masses lower then $0.5\,{\rm M}_{\odot}$ (dotted line) and higher than $0.5\,{\rm M}_{\odot}$ (dashed line).

need the fourth step of our selection procedure in order to remove background/foreground contaminants and to perform an efficient analysis of IC 2391 with $JHK_{\rm s}$ data from 2MASS only (the rejection of objects based on the observed vs. predicted magnitude discrepancy).

From this we conclude that the use of $JHK_{\rm s}$ only is not useful for characterizing a population of low mass objects (with masses lower then $0.7\,{\rm M}_{\odot}$) such as in IC 2391 (with an age of $50\,{\rm Myr}$ and a solar metallicity).

This completes the presentation of the results from our photometric and spectroscopic survey on the open cluster IC 2391 and of the public data from 2MASS available for this cluster. In the following chapter, we will present our study of the stellar and substellar mass functions of open clusters, taken from the literature, from various ages and environment, including our estimation of the mass function of IC 2391.
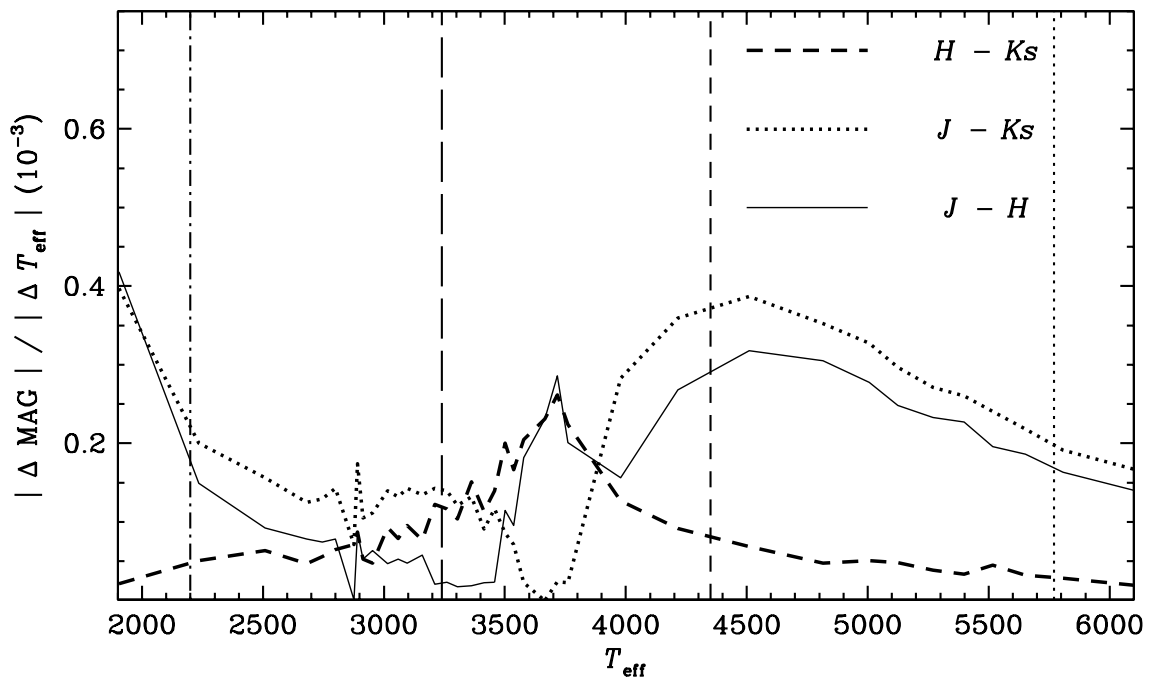
Figure 5.16 Colour sensitivity to effective temperature for the three possible colours in JHK_{s}. The vertical lines mark the approximate effective temperatures for spectral classes L0V (dash-dotted line), M5V (long-dash line), K5V (short-dash line) and G5V (dotted line). We can see that variation in colours with effective temperatures are not as high as for colours with red optical and J bands (as we have seen in Figure 4.3 in §4.1.2).
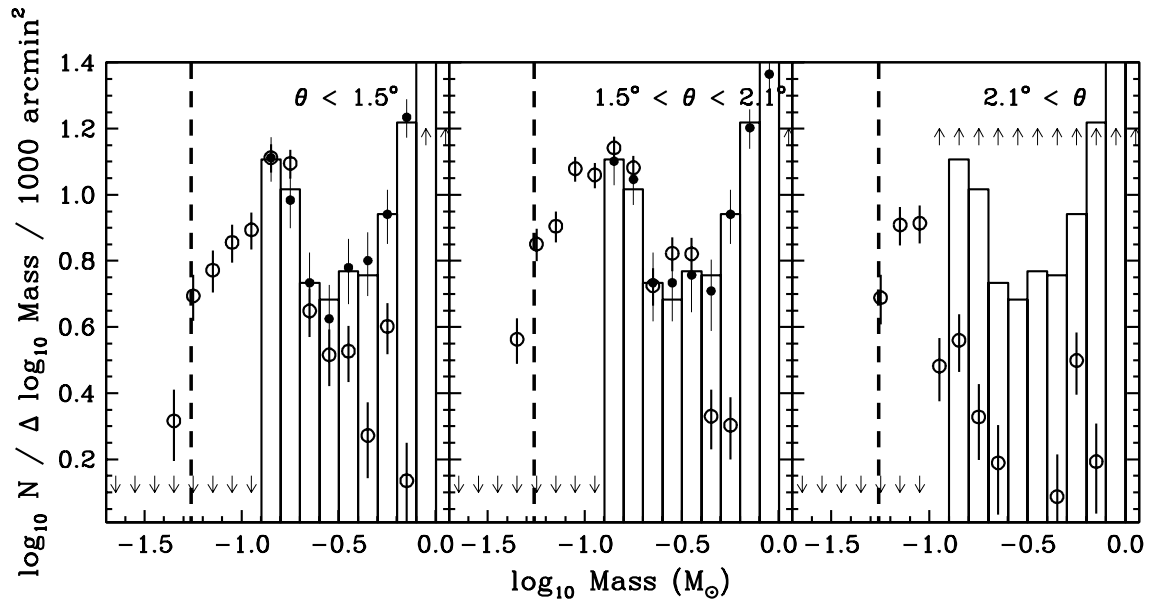
Figure 5.17 Same as Figure 5.15, but using a selection based on colour-magnitude and colour-colour diagrams only.
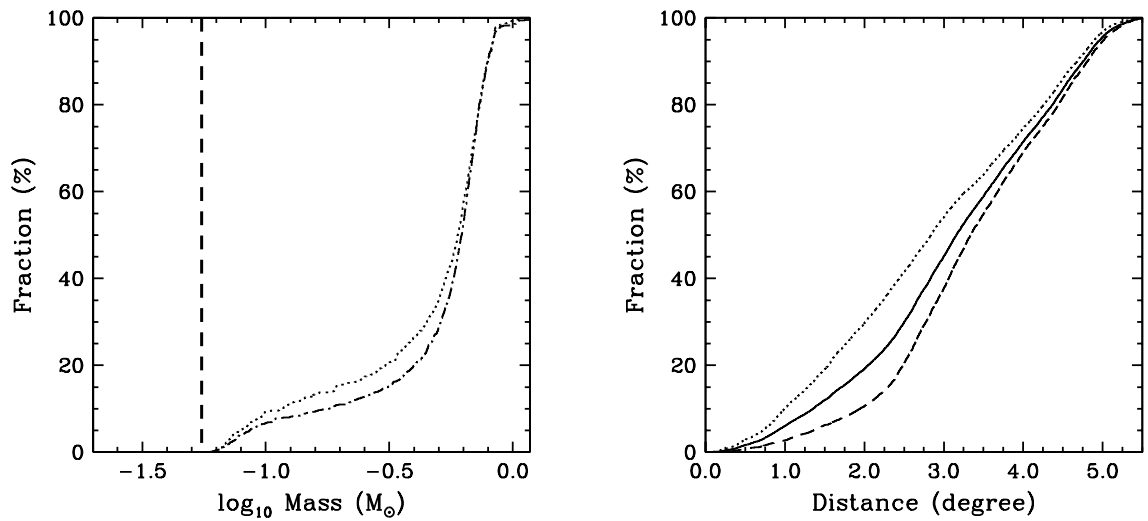
Figure 5.18 Same as Figure 5.15 but using a selection based on colour-magnitude and colour-colour diagrams only.

Table 5.1. All photometric candidates of our survey

Field	ID	RA	DEC	R_c	770/19	815/20	856/14	914/27	J	M	T_eff	[815/20]
01	001	8:26:16.055	-51:02:52.32	19.645	–	16.706	–	16.292	15.023	0.057	2768	17.220
01	002	8:26:14.211	-51:02:47.64	18.426	–	16.200	–	15.920	15.145	0.104	3072	15.943
01	003	8:25:28.826	-51:13:56.71	18.866	–	16.383	–	15.998	14.909	0.081	2957	16.450
01	004	8:25:47.698	-51:06:25.26	18.848	–	16.332	–	15.953	14.969	0.078	2935	16.537
01	005	8:25:26.432	-51:03:59.27	18.359	–	16.077	–	15.771	14.962	0.096	3043	16.080
01	006	8:25:01.148	-51:03:37.82	19.574	–	16.953	–	16.582	15.446	0.072	2890	16.710
01	007	8:24:10.028	-51:07:26.14	19.283	–	16.735	–	16.341	15.427	0.076	2925	16.576
01	008	8:24:33.508	-51:05:35.22	18.764	–	16.437	–	16.094	15.130	0.093	3029	16.146
01	009	8:23:19.415	-51:32:35.82	19.900	–	17.106	–	16.655	15.618	0.065	2838	16.930
01	010	8:23:29.455	-51:32:00.48	18.373	–	16.076	–	15.762	15.014	0.094	3032	16.134

Note. — Table 5.1 is available in its entirety in *Appendix A* at the end of this thesis. A portion is shown here for guidance regarding its form and content. The error on the determination of masses and effective temperature are the following : $\Delta T_\mathrm{eff} = 140\,\mathrm{K}$ and $\Delta\mathrm{M} = 0.1\,\mathrm{M}_\odot$ for stars $(\mathrm{M} > 0.2\,\mathrm{M}_\odot)$, $\Delta T_\mathrm{eff} = 230\,\mathrm{K}$ and $\Delta\mathrm{M} = 0.05\,\mathrm{M}_\odot$ for very low-mass stars $(0.072_\odot < \mathrm{M} < 0.2\,\mathrm{M}_\odot)$, $\Delta T_\mathrm{eff} = 420\,\mathrm{K}$ and $\Delta\mathrm{M} = 0.02\,\mathrm{M}_\odot$ for brown dwarfs $(\mathrm{M} < 0.072\,\mathrm{M}_\odot)$. The magnitude [815/20] is the predicted magnitude based on photometric determination of T_eff and mass.

Table 5.2.   Objects from Barrado y Navascués et al. (2004a), Dodd (2004) and detected
by XMM-Newton which are photometric candidates in our sample

Field	ID	RA	DEC	815/20	M	T_{eff}	[815/20]	NAME	Ic	$(R-I)c$	T_{eff}
18	006	8:38:47.074	-52:14:56.16	17.076	0.053	2723	17.396	CTIO-061	17.309	2.141	2801
20	028	8:38:47.282	-52:44:32.61	16.662	0.077	2927	16.567	CTIO-062	16.765	2.	2937
27	002	8:40:09.537	-53:37:49.81	16.153	0.095	3036	16.115	CTIO-077	16.308	1.929	2960
32	120	8:44:02.109	-52:44:10.73	17.05	0.065	2842	16.911	CTIO-160	17.151	2.09	2806
32	295	8:43:38.422	-52:50:55.13	14.848	0.206	3310	14.707	CTIO-152	14.891	1.781	3053
32	295	8:43:38.422	-52:50:55.13	14.848	0.206	3310	14.707	155	14.53	2.26	-
32	325	8:46:15.404	-52:49:37.61	15.305	0.17	3249	15.046	2XMM J084615.3-524937	-	-	-
32	340	8:46:04.238	-52:45:18.99	15.921	0.122	3134	15.64	2XMM J084604.3-524518	-	-	-
37	024	8:47:07.572	-53:09:45.32	15.377	0.159	3228	15.164	2XMM J084706.2-530944	-	-	-

Note. — CTIO objects are from Barrado y Navascués et al. (2004a), object 155 is from citedodd2004 while the 2XMM objects are from
XMM-Newton.

Table 5.3.   Stellar parameters obtained from spectra.

Field	ID	RA	DEC	SNR	SpT	T_{eff}	M	815/20	T_{eff} (phot)	M (phot)	[815/20]
15	02	8:38:27.108	-53:25:10.55	9.8	M6.0	2840.	0.065	15.567	3158.	0.130	15.524
15	04	8:35:53.166	-53:22:11.77	4.	-	-	-	19.204	2457.	0.038	18.470
15	05	8:36:06.221	-53:28:06.48	5.1	M5.0	3010.	0.089	18.967	2513.	0.040	18.240
15	07	8:35:00.736	-53:23:54.88	1.6	-	-	-	18.952	2506.	0.040	18.270
15	08	8:38:23.477	-53:24:29.07	0.5	-	-	-	18.843	2528.	0.041	18.180
15	09	8:37:24.833	-53:27:03.76	0.6	-	-	-	18.834	2520.	0.041	18.215
15	10	8:38:08.497	-53:36:34.38	1.4	-	-	-	18.838	2511.	0.040	18.249
15	12	8:37:47.255	-53:23:38.06	0.5	-	-	-	18.713	2533.	0.041	18.162
15	13	8:36:32.803	-53:48:27.41	11.9	M4.0	3222.	0.155	18.712	2566.	0.043	18.029
15	15	8:34:54.776	-53:24:23.45	4.3	-	-	-	18.651	2546.	0.042	18.109
15	16	8:37:24.632	-53:19:48.37	5.5	M4.0	3430.	0.318	18.656	2552.	0.042	18.086
15	17	8:35:06.758	-53:19:30.38	1.1	-	-	-	19.764	2391.	0.036	18.743
15	19	8:37:57.798	-53:43:54.69	6.9	M2.5	2660.	0.049	18.547	2546.	0.042	18.107
15	20	8:36:26.653	-53:46:29.29	5.6	M8.5	2780.	0.056	18.522	2554.	0.043	18.077
15	23	8:38:25.315	-53:36:16.38	0.5	-	-	-	18.506	2566.	0.043	18.027
15	25	8:36:12.232	-53:28:43.31	3.2	-	-	-	18.385	2566.	0.043	18.028
15	26	8:38:15.220	-53:27:55.13	0.8	-	-	-	18.334	2593.	0.045	17.920
15	27	8:37:26.524	-53:49:33.99	0.5	-	-	-	18.297	2600.	0.045	17.890
15	28	8:37:10.350	-53:38:43.22	6.	M6.5	2897.	0.07	18.280	2592.	0.045	17.924
15	30	8:34:46.931	-53:27:11.37	2.2	-	-	-	18.278	2613.	0.046	17.839
15	31	8:36:54.229	-53:41:27.08	13.1	M5.5	2925.	0.073	18.235	2620.	0.046	17.809
15	32	8:35:29.945	-53:36:49.00	5.4	M5.5	2925.	0.073	18.187	2628.	0.047	17.777
15	33	8:36:25.082	-53:33:41.88	9.	M3.0	3180.	0.138	18.078	2646.	0.048	17.706
15	34	8:37:20.901	-53:34:49.06	11.8	M6.0	3067.	0.102	17.986	2656.	0.049	17.664
15	36	8:36:43.525	-53:29:42.28	19.4	M5.0	3123.	0.119	17.892	2690.	0.051	17.528
15	37	8:36:18.241	-53:25:57.60	8.3	M8.5	2800.	0.06	17.803	2654.	0.048	17.672
15	38	8:35:31.946	-53:37:15.48	7.	M5.5	3265.	0.173	17.752	2724.	0.053	17.394
15	39	8:35:16.877	-53:50:25.75	4.3	-	-	-	17.709	2711.	0.052	17.446
15	40	8:37:21.423	-53:22:21.01	4.5	-	-	-	17.683	2721.	0.053	17.403
15	41	8:38:14.371	-53:37:57.85	0.7	-	-	-	17.591	2749.	0.055	17.293
15	42	8:36:26.818	-53:50:14.08	4.8	-	-	-	20.866	2194.	0.029	19.562
15	44	8:36:32.268	-53:33:55.23	9.7	M5.5	3123.	0.119	17.440	2794.	0.059	17.114
15	48	8:37:22.883	-53:23:38.94	6.3	M5.0	3010.	0.089	17.313	2808.	0.061	17.059
15	49	8:36:25.252	-53:39:54.53	16.4	M5.0	2968.	0.082	17.237	2818.	0.062	17.014
15	50	8:34:58.773	-53:45:30.20	6.5	M6.5	2780.	0.056	17.182	2825.	0.063	16.985
15	51	8:38:18.367	-53:46:53.79	15.2	M6.0	2882.	0.07	23.580	2825.	0.063	16.985

Table 5.3 (cont'd)

Field	ID	RA	DEC	SNR	SpT	T_{eff}	M	815/20	T_{eff} (phot)	M (phot)	[815/20]
15	53	8:37:41.091	-53:44:00.31	12.7	M6.5	2897.	0.07	16.877	2890.	0.072	16.711
15	54	8:37:12.839	-53:46:09.43	6.8	M8.5	2882.	0.07	16.643	2940.	0.078	16.518
15	55	8:36:05.866	-53:24:58.91	10.4	M5.0	3180.	0.138	16.646	2948.	0.080	16.484
15	56	8:38:06.120	-53:38:10.55	9.	M6.5	2982.	0.085	16.651	2925.	0.076	16.576
15	57	8:35:21.606	-53:42:05.12	8.	M6.0	2925.	0.073	16.473	2955.	0.081	16.456
15	58	8:37:46.333	-53:20:22.54	4.	-	-	-	16.447	2981.	0.085	16.353
15	59	8:36:04.075	-53:29:25.00	20.7	M4.0	3123.	0.119	16.306	3010.	0.089	16.232
15	60	8:36:40.363	-53:21:30.00	6.1	M4.5	3123.	0.119	16.201	3020.	0.091	16.191
15	62	8:36:46.966	-53:38:31.22	23.5	M7.0	2820.	0.063	15.891	3074.	0.104	15.934
15	63	8:36:54.586	-53:45:39.81	35.2	M5.5	3038.	0.095	15.487	3170.	0.134	15.465
15	64	8:37:40.590	-53:45:57.99	13.4	M5.5	3010.	0.089	15.435	3167.	0.133	15.479
15	65	8:38:22.952	-53:42:29.99	28.6	M6.5	3067.	0.102	15.120	3231.	0.160	15.145
15	68	8:38:17.429	-53:24:41.36	5.2	M7.0	2750.	0.051	19.178	2482.	0.039	18.370
15	69	8:37:54.086	-53:27:24.41	1.5	-	-	-	19.088	2486.	0.039	18.351
15	70	8:36:34.643	-53:22:05.17	0.8	-	-	-	19.034	2483.	0.039	18.367
15	72	8:36:24.215	-53:20:12.91	2.8	-	-	-	19.115	2472.	0.039	18.412
15	75	8:37:52.713	-53:42:51.22	3.6	-	-	-	18.873	2521.	0.041	18.208
15	76	8:35:45.205	-53:50:04.22	3.5	-	-	-	18.899	2522.	0.041	18.207
15	78	8:38:26.031	-53:37:33.79	2.1	-	-	-	18.848	2531.	0.041	18.170
15	79	8:37:46.877	-53:30:41.54	1.4	-	-	-	19.114	2518.	0.040	18.224
15	80	8:36:30.984	-53:28:34.95	2.2	-	-	-	18.702	2537.	0.042	18.146
15	81	8:35:58.081	-53:40:27.05	2.	-	-	-	18.715	2522.	0.041	18.205
15	84	8:36:09.958	-53:48:52.69	1.5	-	-	-	18.701	2535.	0.042	18.153
15	85	8:35:10.572	-53:47:30.67	0.8	-	-	-	18.604	2550.	0.042	18.091
15	86	8:35:52.682	-53:38:10.53	3.4	-	-	-	18.587	2548.	0.042	18.103
15	87	8:38:04.168	-53:33:41.70	0.6	-	-	-	18.365	2594.	0.045	17.915
15	88	8:36:23.512	-53:42:25.37	5.3	M5.5	2953.	0.08	18.370	2578.	0.044	17.979
15	90	8:36:28.072	-53:20:45.97	3.3	-	-	-	18.257	2618.	0.046	17.817
15	91	8:35:30.057	-53:44:56.58	0.9	-	-	-	18.234	2603.	0.045	17.880
15	93	8:36:20.262	-53:23:40.58	3.4	-	-	-	18.100	2647.	0.048	17.703
15	95	8:36:01.356	-53:39:24.50	9.1	M5.5	3095.	0.11	20.261	2264.	0.031	19.264
15	96	8:36:46.246	-53:31:32.49	10.5	M5.5	3180.	0.138	17.988	2714.	0.052	17.433
15	98	8:35:21.003	-53:28:04.39	2.9	-	-	-	17.607	2713.	0.052	17.438
15	99	8:36:51.793	-53:34:13.60	16.7	M4.0	3180.	0.138	17.189	2836.	0.065	16.935
20	02	8:38:47.281	-52:44:32.61	17.	M6.5	2897.	0.07	16.662	2927.	0.077	16.567
20	03	8:38:11.866	-52:22:51.09	26.1	M6.5	2810.	0.061	16.633	2958.	0.081	16.446

Table 5.3 (cont'd)

Field	ID	RA	DEC	SNR	SpT	T_{eff}	M	815/20	T_{eff} (phot)	M (phot)	[815/20]
20	05	8:39:24.080	-52:48:06.34	7.2	M5.5	2968.	0.082	19.133	2493.	0.039	18.323
20	06	8:40:13.947	-52:51:23.34	1.1	-	-	-	19.166	2488.	0.039	18.346
20	07	8:38:13.504	-52:19:38.64	5.4	M7.0	2925.	0.073	18.904	2555.	0.043	18.072
20	08	8:40:12.207	-52:25:55.52	7.6	M7.0	2750.	0.051	19.801	2378.	0.035	18.796
20	10	8:37:25.510	-52:40:07.74	4.8	-	-	-	18.921	2520.	0.041	18.213
20	11	8:38:39.264	-52:43:37.10	5.9	M7.0	2750.	0.051	18.849	2527.	0.041	18.186
20	12	8:37:56.884	-52:50:02.53	1.2	-	-	-	18.874	2520.	0.041	18.215
20	15	8:40:24.736	-52:44:31.08	5.1	M6.0	3095.	0.11	18.706	2547.	0.042	18.106
20	17	8:38:42.432	-52:26:29.34	4.3	-	-	-	19.557	2434.	0.037	18.564
20	19	8:39:40.773	-52:49:11.77	0.5	-	-	-	18.573	2547.	0.042	18.105
20	20	8:40:07.148	-52:21:33.61	6.	M5.5	3208.	0.149	18.608	2561.	0.043	18.048
20	23	8:40:48.947	-52:25:39.73	11.3	M5.5	3123.	0.119	18.517	2565.	0.043	18.031
20	24	8:39:22.024	-52:36:56.51	7.	M5.5	3038.	0.095	18.469	2563.	0.043	18.041
20	26	8:40:25.201	-52:20:50.98	6.6	M6.0	3095.	0.11	18.494	2556.	0.043	18.070
20	27	8:39:12.127	-52:42:08.56	8.8	M6.0	3010.	0.089	18.459	2574.	0.044	17.998
20	28	8:38:35.241	-52:36:50.93	10.9	M5.0	3010.	0.089	18.474	2580.	0.044	17.971
20	29	8:40:33.271	-52:48:24.64	7.1	M6.5	3010.	0.089	18.426	2588.	0.045	17.939
20	32	8:39:13.160	-52:50:56.79	2.5	-	-	-	18.272	2606.	0.046	17.866
20	34	8:39:50.948	-52:21:05.58	11.3	M7.0	2750.	0.051	18.209	2641.	0.048	17.724
20	35	8:38:24.703	-52:44:18.77	10.2	M5.5	2968.	0.082	17.995	2672.	0.049	17.602
20	38	8:39:29.612	-52:32:59.31	13.1	M6.0	2953.	0.08	17.861	2681.	0.050	17.563
20	39	8:39:46.855	-52:21:27.85	12.1	M5.5	2968.	0.082	17.849	2707.	0.052	17.459
20	40	8:37:28.753	-52:40:36.93	6.8	M6.0	2882.	0.07	17.814	2722.	0.053	17.401
20	42	8:37:33.367	-52:44:57.58	10.5	M5.5	2925.	0.073	17.658	2755.	0.056	17.269
20	43	8:37:33.974	-52:30:16.38	8.6	M5.5	3095.	0.11	17.558	2780.	0.058	17.168
20	44	8:38:18.227	-52:36:45.94	12.7	M5.0	3052.	0.099	19.657	2433.	0.037	18.569
20	45	8:40:16.671	-52:36:58.32	21.4	M6.5	2780.	0.056	17.571	2740.	0.055	17.329
20	46	8:37:32.709	-52:23:36.72	7.6	M6.5	3138.	0.123	17.500	2753.	0.056	17.277
20	50	8:40:39.638	-52:50:42.80	13.4	M5.5	2925.	0.073	17.210	2824.	0.063	16.986
20	51	8:40:45.126	-52:39:02.16	15.	M7.0	2897.	0.07	17.200	2813.	0.062	17.036
20	52	8:40:26.611	-52:26:43.82	21.2	M6.0	2882.	0.07	17.160	2843.	0.066	16.908
20	54	8:37:58.411	-52:20:30.69	22.	M5.5	3095.	0.11	16.907	2890.	0.072	16.710
20	55	8:38:01.879	-52:29:56.00	19.6	M6.0	2897.	0.07	16.847	2911.	0.075	16.629
20	56	8:38:36.649	-52:27:47.16	20.2	M5.0	3010.	0.089	16.873	2911.	0.075	16.631
20	57	8:37:54.197	-52:21:26.33	22.	M6.0	3123.	0.119	20.323	2289.	0.032	19.159
20	58	8:40:34.407	-52:30:38.65	32.	M5.0	3138.	0.123	16.681	2947.	0.079	16.489

Table 5.3 (cont'd)

Field	ID	RA	DEC	SNR	SpT	$T_{\rm eff}$	M	815/20	$T_{\rm eff}$ (phot)	M (phot)	[815/20]
20	59	8:37:38.539	-52:29:35.37	9.2	M5.0	3010.	0.089	16.645	2956.	0.081	16.453
20	60	8:39:33.260	-52:47:10.40	21.8	M6.0	2925.	0.073	16.520	2958.	0.081	16.445
20	61	8:40:15.153	-52:40:24.56	26.5	M7.5	2840.	0.065	16.494	2955.	0.080	16.459
20	62	8:39:22.724	-52:50:34.42	20.	M2.0	3470.	0.364	16.433	2998.	0.087	16.280
20	63	8:37:34.755	-52:27:02.90	27.6	M5.0	3010.	0.089	16.307	3026.	0.093	16.161
20	65	8:40:51.831	-52:34:48.35	50.7	M6.0	2882.	0.07	19.010	2540.	0.042	18.134
20	69	8:40:47.048	-52:48:30.99	22.5	M5.5	3350.	0.241	15.496	3177.	0.137	15.427
20	71	8:39:24.874	-52:21:45.52	4.1	-	-	-	19.163	2468.	0.039	18.426
20	74	8:39:17.189	-52:26:55.11	12.5	M6.0	2840.	0.065	18.742	2545.	0.042	18.114
20	75	8:40:16.277	-52:26:27.39	8.1	M6.0	2882.	0.07	18.625	2556.	0.043	18.069
20	77	8:39:29.183	-52:38:58.86	1.8	-	-	-	18.398	2583.	0.044	17.961
20	78	8:37:50.558	-52:33:04.66	6.	M5.0	3052.	0.099	18.351	2608.	0.046	17.860

Note. — Table 5.3 is published in its entirety in the electronic edition of the *Astrophysical Journal*. A portion is shown here for guidance regarding its form and content. The error on the determination of masses and effective temperature based on spectroscopy are the following : $\Delta T_{\rm eff} = 190\,{\rm K}$ and $\Delta{\rm M} = 0.03\,{\rm M}_\odot$ for spectra with ${\rm SNR} > 10$, $\Delta T_{\rm eff} = 320\,{\rm K}$ and $\Delta{\rm M} = 0.04\,{\rm M}_\odot$ for spectra with $5 < {\rm SNR} < 10$. This would correspond to an error on the spectral determination of 1 and 1.5 for spectra with ${\rm SNR} > 10$ and $5 < {\rm SNR} < 10$ respectively.

Table 5.4. Objects from Barrado y Navascués et al. (2004a) which we also observed in our spectroscopic follow-up.

Field	ID	RA	DEC	SNR	SpT	T_{eff}	M	NAME	SpT	T_{eff}
15	02	8:38:27.108	-53:25:10.55	9.8	M6.0	2840.	0.065	CTIO-049	M5.0	3000
20	02	8:38:47.281	-52:44:32.61	17.	M6.0	2897.	0.07	CTIO-062	M6.0	2800
20	03	8:38:11.866	-52:22:51.09	26.1	M6.0	2810.	0.061	CTIO-041	M5.0	3000

Table 5.5. Spectroscopic data, photometric and spectroscopic membership status for all objects observed in our spectroscopic follow-up

Field	ID	SNR	SpT	$EW(\text{H}\alpha)$	$EW(\text{NaI } 8182\,\text{Å})$	$EW(\text{NaI } 8194\,\text{Å})$	RV (km/s)	Phot member ?	Spec member ?
15	02	9.8	M6.0	2.468	.8405	1.84	-	YES	NO
15	04	4.	-	-	-	-	-	YES	-
15	05	5.1	M6.0	1.452	-	-	-	NO	NO
15	07	1.6	-	-	-	-	-	YES	-
15	08	0.5	-	-	-	-	-	YES	-
15	09	0.6	-	-	-	-	-	YES	-
15	10	1.4	-	-	-	-	-	YES	-
15	12	0.5	-	-	-	-	-	YES	-
15	13	11.9	M4.5	3.657	-	-	20.05 (1.0)	YES	NO
15	15	4.3	-	-	-	-	-	YES	-
15	16	5.5	M4.0	11.09	-	-	-	YES	NO
15	17	1.1	-	-	-	-	-	YES	-
15	19	6.9	L0.0	3.606	-	.6861	-	YES	NO
15	20	5.6	M7.0	-	-	-	-	YES	NO
15	23	0.5	-	-	-	-	-	YES	-
15	25	3.2	-	-	-	-	-	YES	-
15	26	0.8	-	-	-	-	-	NO	-
15	27	0.5	-	-	-	-	-	YES	-
15	28	6.	M8.0	-	1.686	2.487	41.73 (12.2)	YES	NO
15	30	2.2	-	-	-	-	-	YES	-
15	31	13.1	M6.0	19.74	1.991	-	-	YES	NO
15	32	5.4	M6.5	-	-	-	-1.74 (2.0)	YES	NO
15	33	9.	M1.0	-	-	1.409	-	NO	NO
15	34	11.8	M6.5	5.239	1.035	-	-	NO	NO
15	36	19.4	M4.5	3.71	2.427	-	41.65 (9.1)	NO	NO
15	37	8.3	M7.5	-	-	-	-	YES	YES
15	38	7.	M5.5	5.394	.6298	-	59.56 (13.8)	NO	NO
15	39	4.3	-	-	-	-	-	YES	-
15	40	4.5	-	-	-	-	-	YES	-
15	41	0.7	-	-	-	-	-	YES	-
15	42	4.8	-	-	-	-	-	NO	-
15	44	9.7	M6.0	-	-	1.24	45.34 (26.4)	YES	NO
15	48	6.3	M5.5	-	-	-	-	YES	NO
15	49	16.4	M5.0	-	1.917	3.542	19.45 (10.0)	YES	NO
15	50	6.5	M6.5	2.632	-	-	-	YES	YES
15	51	15.2	M6.0	5.037	.5273	1.119	-	NO	NO

Table 5.5 (cont'd)

Field	ID	SNR	SpT	$EW(\text{H}\alpha)$	$EW(\text{NaI 8182 Å})$	$EW(\text{NaI 8194 Å})$	RV (km/s)	Phot member ?	Spec member ?
15	53	12.7	M5.5	14.79	1.39	2.749	26.7 (12.4)	YES	YES
15	54	6.8	M8.5	4.976	-	2.478	-2.92 (9.5)	YES	YES
15	55	10.4	M4.0	5.552	-	-	5.16 (12.2)	YES	NO
15	56	9.	M7.0	6.8	2.15	1.767	-13.86 (25.8)	YES	YES
15	57	8.	M7.5	-	.7459	-	-4.71 (6.7)	YES	YES
15	58	4.	-	-	-	-	-	YES	-
15	59	20.7	M3.5	7.382	3.115	2.434	1.79 (7.4)	YES	NO
15	60	6.1	M2.0	8.812	1.211	-	-	YES	NO
15	62	23.5	M7.0	-	1.552	2.573	19.92 (6.4)	YES	NO
15	63	35.2	M5.5	12.66	1.017	1.752	7.86 (11.4)	YES	NO
15	64	13.4	M6.5	10.27	2.211	2.458	26.44 (10.0)	YES	NO
15	65	28.6	M6.5	3.481	1.141	2.148	23.95 (5.5)	YES	NO
15	68	5.2	M5.5	2.643	-	-	-16.5 (1.6)	YES	NO
15	69	1.5	-	-	-	-	-	NO	-
15	70	0.8	-	-	-	-	-	NO	-
15	72	2.8	-	-	-	-	-	YES	-
15	75	3.6	-	-	-	-	-	YES	-
15	76	3.5	-	-	-	-	-	YES	-
15	78	2.1	-	-	-	-	-	NO	-
15	79	1.4	-	-	-	-	-	NO	-
15	80	2.2	-	-	-	-	-	YES	-
15	81	2.	-	-	-	-	-	YES	-
15	84	1.5	-	-	-	-	-	YES	-
15	85	0.8	-	-	-	-	-	YES	-
15	86	3.4	-	-	-	-	-	YES	-
15	87	0.6	-	-	-	-	-	NO	-
15	88	5.3	M2.5	15.19	-	2.644	49.66 (14.2)	NO	NO
15	90	3.3	-	-	-	-	-	NO	-
15	91	0.9	-	-	-	-	-	NO	-
15	93	3.4	-	-	-	-	-	NO	-
15	95	9.1	M2.0	14.31	-	1.849	-	NO	NO
15	96	10.5	M5.5	2.515	-	-	-1.86 (4.4)	NO	NO
15	98	2.9	-	-	-	-	-	NO	-
15	99	16.7	M4.0	1.874	-	.8876	43.89 (7.7)	NO	NO
20	02	17.	M6.0	13.03	1.552	2.607	14.95 (8.14)	YES	YES
20	03	26.1	M6.0	39.73	3.673	3.005	16.94 (7.82)	YES	YES

Table 5.5 (cont'd)

Field	ID	SNR	SpT	EW(Hα)	EW(NaI 8182 Å)	EW(NaI 8194 Å)	RV (km/s)	Phot member ?	Spec member ?
20	05	7.2	M5.0	15.93	0.53	.6742	-64.14 (15.44)	YES	NO
20	06	1.1	-	-	-	-	-	YES	-
20	07	5.4	M7.0	74.25	-	-	-	NO	NO
20	08	7.6	M5.5	5.712	1.572	-	-	NO	NO
20	10	4.8	-	-	-	-	-	YES	-
20	11	5.9	M6.5	12.36	-	-	36.92 (26.7)	YES	NO
20	12	1.2	-	-	-	-	-	YES	-
20	15	5.1	M5.5	25.39	2.712	2.396	-	YES	NO
20	17	4.3	-	-	-	-	-	YES	-
20	19	0.5	-	-	-	-	-	YES	-
20	20	6.	M5.0	6.435	-	-	-	YES	NO
20	23	11.3	M5.0	-	3.85	2.208	25.42 (17.6)	YES	NO
20	24	7.	M4.5	25.12	.4947	2.925	17.77 (15.26)	YES	NO
20	26	6.6	M5.5	-	-	1.314	34.66 (19.42)	NO	NO
20	27	8.8	M5.0	14.45	-	1.801	-	YES	NO
20	28	10.9	M5.0	9.123	-	2.245	2.52 (11.34)	YES	NO
20	29	7.1	M5.5	25.52	-	-	20.85 (13.26)	YES	NO
20	32	2.5	-	-	-	-	-	YES	-
20	34	11.3	M6.5	7.454	-	-	-	YES	YES
20	35	10.2	M5.0	38.37	1.34	1.27	98.11 (8.89)	YES	NO
20	38	13.1	M6.5	5.8	-	1.961	6.23 (7.04)	YES	NO
20	39	12.1	M4.5	20.53	-	-	103.85 (14.62)	YES	NO
20	40	6.8	M4.0	8.528	1.115	-	10.72 (23.52)	YES	YES
20	42	10.5	M4.5	13.12	-	1.634	26.74 (11.2)	YES	YES
20	43	8.6	M4.5	5.059	-	-	-	YES	NO
20	44	12.7	M4.0	32.43	3.664	4.312	-	NO	NO
20	45	21.4	M6.5	2.74	2.378	2.332	16.25 (6.59)	YES	YES
20	46	7.6	M6.5	37.14	-	3.617	-	YES	NO
20	50	13.4	M5.5	22.36	1.037	-	21.95 (8.68)	NO	NO
20	51	15.	M7.0	11.21	3.82	3.57	16.6 (8.01)	YES	YES
20	52	21.2	M6.0	1.824	1.886	2.14	13.47 (6.85)	YES	YES
20	54	22.	M5.0	21.36	1.913	3.32	19.32 (7.78)	YES	NO
20	55	19.6	M5.5	14.72	1.352	2.326	53.89 (7.73)	YES	NO
20	56	20.2	M5.0	17.56	2.65	2.191	-18.28 (12.37)	YES	YES
20	57	22.	M6.5	25.09	-	2.44	45.79 (9.29)	YES	NO
20	58	32.	M5.0	-	1.208	2.877	15.11 (8.39)	YES	NO

Table 5.5 (cont'd)

Field	ID	SNR	SpT	EW(Hα)	EW(NaI 8182 Å)	EW(NaI 8194 Å)	RV (km/s)	Phot member ?	Spec member ?
20	59	9.2	M4.5	15.18	-	-	11.31 (27.7)	YES	YES
20	60	21.8	M6.5	23.37	1.292	-	27.91 (7.35)	YES	YES
20	61	26.5	M7.5	4.519	1.227	-	11.78 (7.48)	YES	YES
20	62	20.	M2.0	-6.12	-	1.72	94.74 (6.9)	YES	NO
20	63	27.6	M5.0	13.24	-	-	23.33 (6.88)	YES	YES
20	65	50.7	M5.5	-5.14	1.366	2.816	14.52 (6.34)	NO	NO
20	69	22.5	M5.5	4.696	1.538	-	11.89 (7.47)	YES	NO
20	71	4.1	-	-	-	-	-	YES	-
20	74	12.5	M6.0	5.929	-	.8319	-	YES	NO
20	75	8.1	M5.5	8.711	-	1.487	-	YES	NO
20	77	1.8	-	-	-	-	-	YES	-
20	78	6.	M4.5	28.15	-	1.524	-	YES	NO

Table 5.6.   Stellar parameters obtained from spectra.

Field	ID	RA	DEC	SNR	R_c	R_c-815/20	SpT	T_{eff}	M	T_{eff} (phot)	M (phot)
15	37	8:36:18.241	-53:25:57.60	8.3	21.048	3.245	M7.5	2800	0.06	2654	0.048
15	50	8:34:58.773	-53:45:30.20	6.5	19.643	2.461	M6.5	2780	0.056	2825	0.063
20	34	8:39:50.948	-52:21:05.58	11.3	20.015	1.806	M6.5	2750	0.051	2641	0.048
20	40	8:37:28.753	-52:40:36.93	6.8	19.849	2.035	M4.0	2882	0.07	2722	0.053
20	45	8:40:16.671	-52:36:58.32	21.4	20.076	2.505	M6.5	2780	0.056	2740	0.055
20	51	8:40:45.126	-52:39:02.16	15.0	19.995	2.795	M7.0	2897	0.07	2813	0.062
20	52	8:40:26.611	-52:26:43.82	21.2	19.286	2.126	M6.0	2882	0.07	2843	0.066

Chapter 6

Mass function of other open clusters at different ages and environments

In the previous chapter, we presented our analysis of the open cluster IC 2391 based on our photometric and spectroscopic data, and also using only public data available from 2MASS. We can also obtain information on other open clusters in order to improve statistics on the mass functions sampled and conclusions drawn. Indeed, in the first two chapters we have already reported that the mass function is dependent on the age through dynamical evolution and the environment. However, there is no study reported in the literature presenting a large sample of mass functions for various open clusters and looking at whether there are distinctions between the mass functions in different mass regime, on either side of the stellar/substellar boundary, and dependencies on the age and environment of the clusters.

In this chapter, we will use the mass functions presented in the literature for other clusters of different ages and environments. We will look for variations in the stellar and/or substellar regime of the mass function and for correlations with age and/or environment.

6.1 Mass functions obtained from the literature : open clusters at different ages and environments

Here we present the analysis of the stellar and substellar mass functions of several open clusters at different ages and environments. We only use mass function that extend down to the brown dwarf regime, except for M35 and the Hyades, which are used as data point and examples for dynamical evolution at an age of 160 Myr and 620 Myr respectively. Mass functions of open clusters from different environments can be obtained from areas where the densities of gas are different, such as Taurus and the Trapezium (Briceño et al. 2002). However, we can observe if there is a variation of the substellar mass function with environment by looking at open clusters with different metallicity. Indeed, if a molecular cloud is more metal rich, the temperature of this cloud would be smaller because of more efficient cooling (Moraux et al. 2007). This would give a smaller Jeans mass and would shift the characteristic mass towards lower mass.

In Table 6.1 (at the end of this chapter) we present the open clusters used in this analysis. The mass functions for these clusters, sorted by age, are shown in Figure 6.1. In order to study the variation of the mass function with age, we use the ratio between the number of objects in the fixed mass intervals 0.02–0.072 $M_\odot$, 0.072–0.2 $M_\odot$ and 0.2–0.7 $M_\odot$. For clarity, we identify these regions of the mass functions as the *brown dwarf*, *very low-mass star* and *stellar* populations respectively. In Figure 6.3, we present the ratio of the brown dwarf population to the very low-mass star population, the brown dwarf population to the stellar population and the very low-mass star population to the stellar population. (To compute the ratio, we took the average of the number of objects in all mass bins in each mass interval.)

First, we observe that there is no significant variation between the ratio of both the stellar and very low-mass star populations to the brown dwarf population with ages below 10 Myr. This is in total disagreement with a unique formation process for brown dwarfs by the ejection scenario, where the velocity dispersion would be higher for brown dwarfs than for stars, as suggested by Kumar & Schmeja (2007) by comparing the spatial distribution of brown dwarfs and stars in the Orion Nebula Cluster (1 Myr) and IC 348 (3 Myr). Indeed, if brown dwarfs would have a significantly higher initial velocity than stars, one would expect brown dwarfs not to be retained by the cluster potential well whereas stars would be bound. Our analysis of the stellar/substellar mass function of various open clusters with ages below 10 Myr does not support the conclusions of Kumar & Schmeja (2007).

Also, we can observe that beyond 30 Myr, the ratio of brown dwarfs to stars and very low-mass stars to stars are both decreasing. Although only 3 data points are available
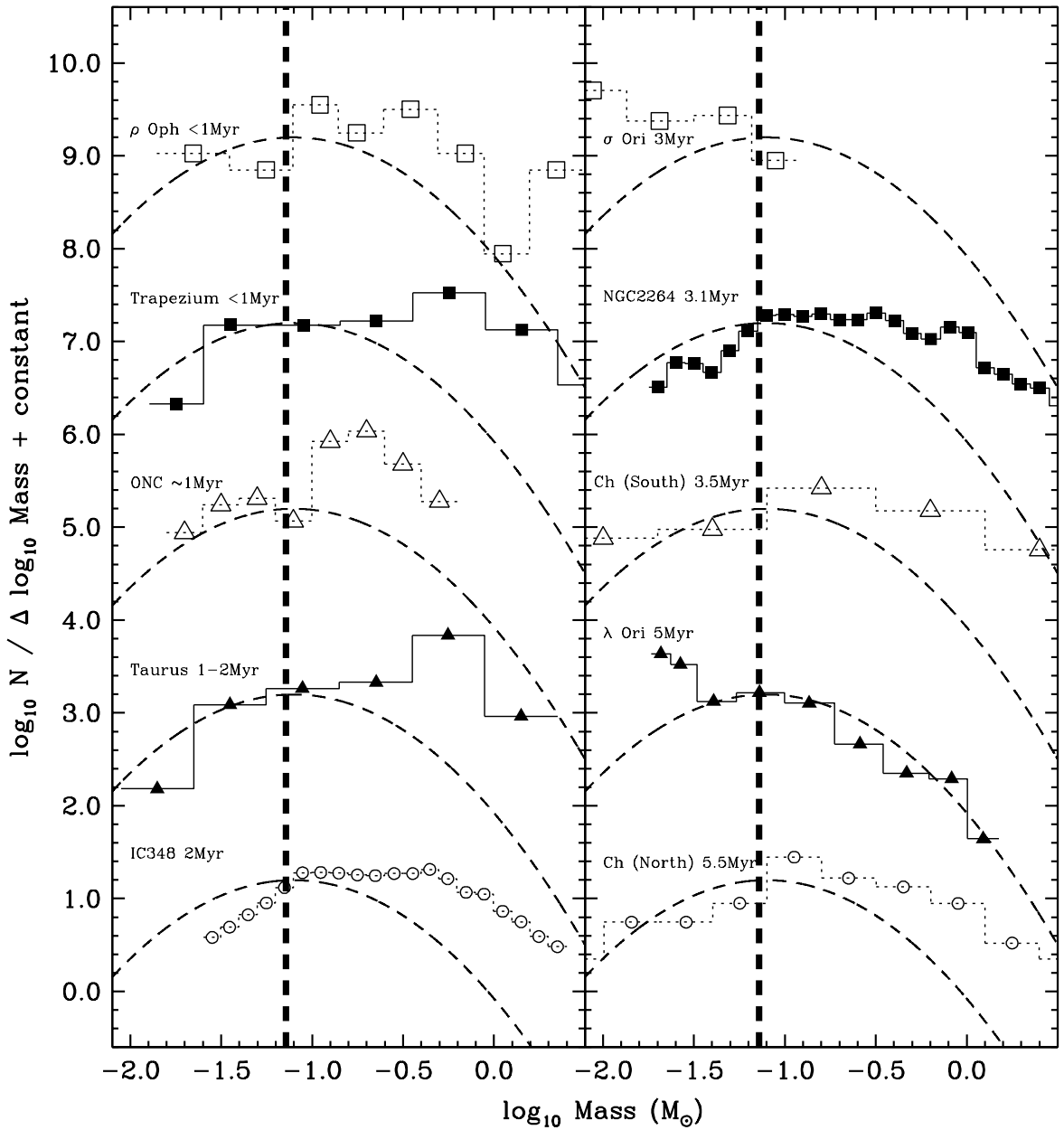
Figure 6.1 Mass functions of open clusters presented in Table 6.1. The lognormal fit of the galactic field stars is shown as a thin dashed line while the vertical thick line represents the stellar/substellar boundary at $0.072\,M_\odot$. The name of the cluster and its age are shown near each mass function. All the mass functions are normalized at the stellar/substellar boundary, except for M35 and the Hyades. (Figure continued on the following page.)

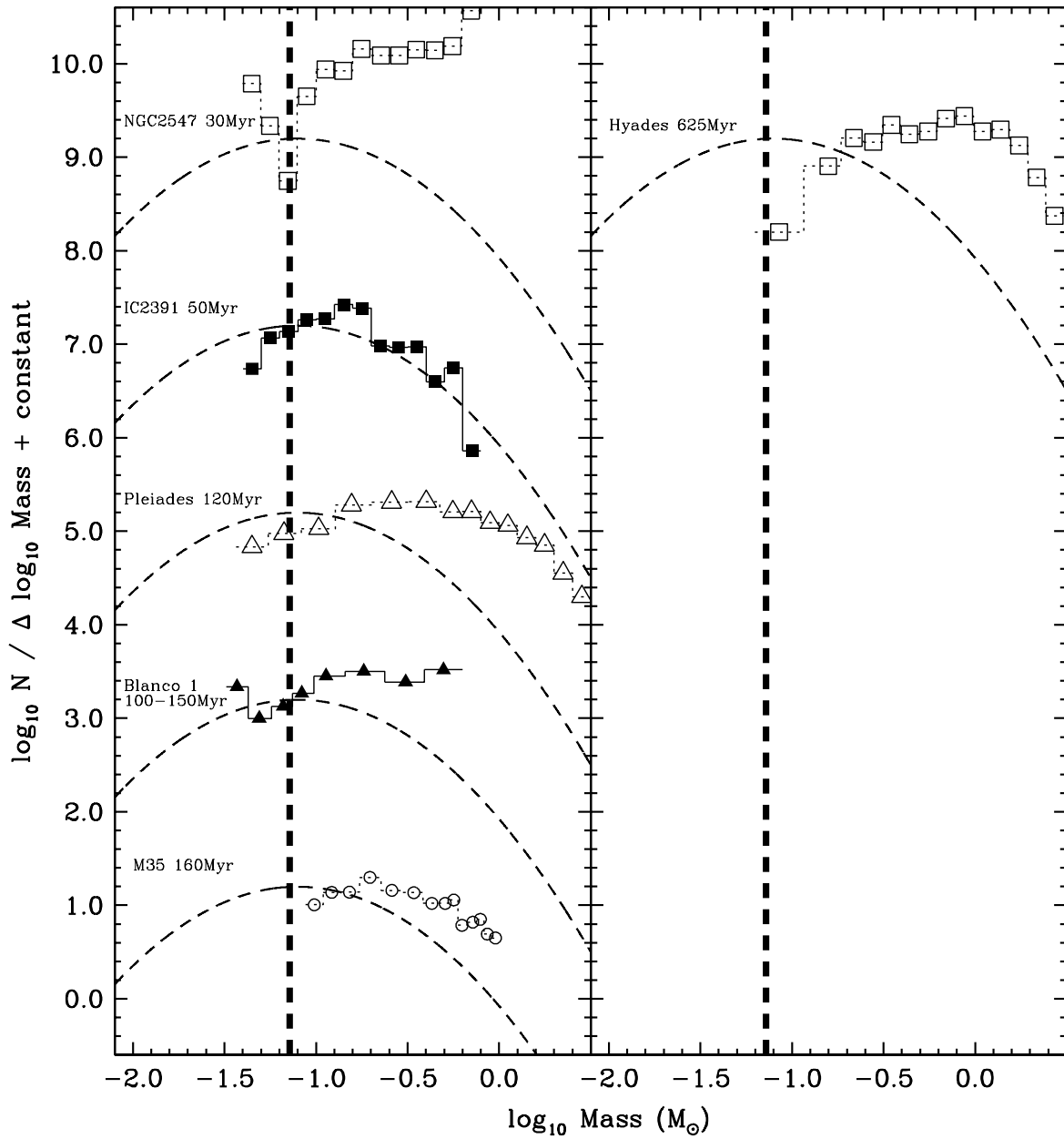beyond that age, this is consistent with dynamical evaporation of the lighter objects. It is

Figure 6.2 Figure 6.1 continued.

also in agreement with the work presented by Bouvier et al. (2008), who estimated that, by comparing the mass function of the Pleiades (120 Myr) with the Hyades (625 Myr), the Hyades might have initially had ∼150–200 brown dwarfs while only ∼10–15 would be in the cluster today.

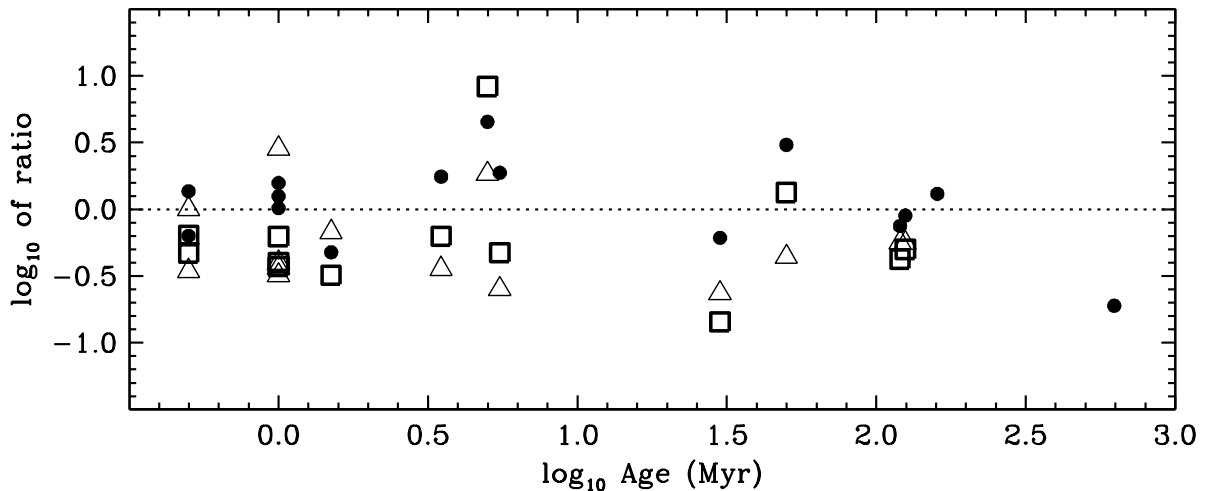Finally, we observe that at all ages the ratio of very low-mass stars to stars is higher than

Figure 6.3 Ratio of the number of objects in the brown dwarf population to the very
low-mass star population (triangle), the brown dwarf population to the stellar popula-
tion (square) and the very low-mass star population the stellar population (dots). The
horizontal dotted line is at a ratio of 1.

both ratios of brown dwarfs to stars and brown dwarfs to very low-mass stars. Furthermore,
this ratio is $\gtrsim 1$ or not lower than 1/2, which is the case for Taurus, the Trapezium, and
NGC 2547. This is an indication that the mean mass of the mass function stays in the mass
range 0.072–$0.2\,M_\odot$ at all ages. Only in the Hyades is the stellar regime significantly more
populated than the very low-mass stars (by a ratio of ~ 5).We can expect that dynamical
evaporation, which doesn't only apply for brown dwarfs, might have started to remove
very low-mass stars in the Hyades. However, Bouvier et al. (2008) do not estimate how
many objects in the 0.072–$0.2\,M_\odot$ range could have been evaporated. A stellar/substellar
mass function determination of other open cluster of the same age as the Hyades, such
as Praesepe ($\sim 650\,\mathrm{Myr}$), could confirm or refute that evaporation of very low-mass stars
occurs in the time scale of $\sim 600\,\mathrm{Myr}$.

We now analyze the mass functions of various open clusters with different metallicities.
Figure 6.4 shows the mass functions where the lower limit reaches the substellar regime
and for which a measurement of metallicity is available.

We can't draw as many conclusions as when comparing mass functions at different ages,
considering that only seven open clusters with different metallicities are available. However,
we note that there is no significant variation of the ratio of very low-mass stars to stars
with metallicity. This would indicate that there is no variation the stellar mass function
with metallicity (at least for the mass interval 0.072–$0.7\,M_\odot$). We see that the Hyades
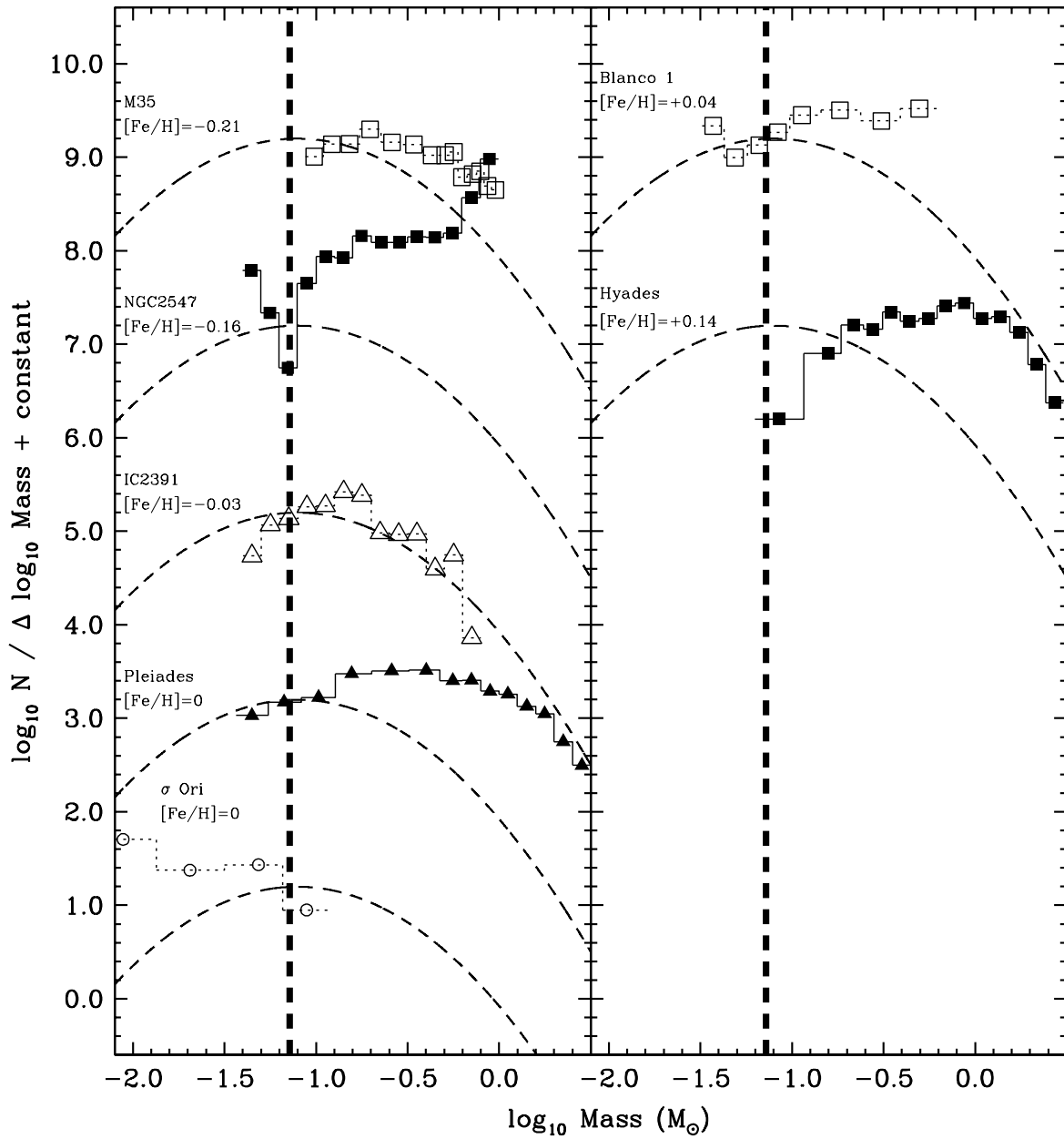
Figure 6.4 Mass functions of open clusters presented in Table 6.1 with metallicity available.
The lognormal fit and the stellar/substellar boundary are the same as in Figure 6.1.

(highest metallicity in our sample with [Fe/H]=0.14) has a low ratio of very low-mass stars
to stars. However, considering our previous discussion, this is a signature of dynamical
evaporation and we can't make any conclusions on metallicity based on this unique data
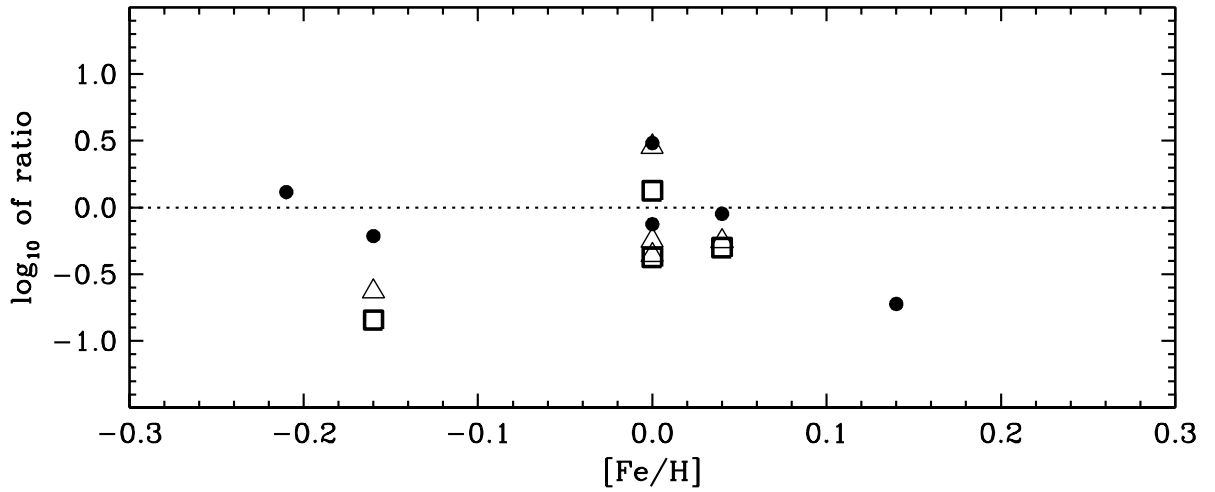point.

Figure 6.5 Same as Figure 6.3, but with metallicity.

As for the variation of the ratios of the brown dwarf population to stars and very low-mass
stars, we can observe that at solar metallicity those ratios stay within as 0.5–2. On the
other hand, the metal poor cluster NGC 2547 ([Fe/H]=-0.16) shows a very low substellar
population compared to the population of stellar objects. This is in agreement with the
fact that lower metallicity in a cloud where star formation occurs would imply a higher
Jeans mass, and thus a higher characteristic mass. Once more, considering that only 4
data points are available in Figure 6.5, this suggestion should be taken with care.

This completes the analysis of the stellar/substellar mass functions of various open clusters
in the literature. In the following chapter, we will review the works and results presented
in this thesis and our conclusions on possible brown dwarf formation mechanisms.

Table 6.1.   Cluster used for our analysis of variation of the stellar and substellar mass function with age and environments.

NAme	RA	DEC	Distance (pc)	Age (Myr)	[Fe/H]	References
ρ Ophiuchi	16:25:35	-23:26:05	160	$\lesssim$1	-	Luhman & Rieke (1999)
Trapezium	05:35:17	-05:23:14	451	$\lesssim$1	-	Luhman (2000b)
Orion Nebula Cluster	05:35:00	-05:29:00	160	1	-	Slesnick et al. (2004)
Taurus	04:41:00	+25:52:00	140	1–2	-	Briceño et al. (2002)
IC 348	03:44:34	+32:09:48	320	2	-	Muench et al. (2003)
σ Orionis	05:38:42	-02:37:00	360	3	0	Caballero et al. (2007)
NGC 2264	06:41:00	+09:53:00	760	3.1	-	Sung et al. (2004)
Chamaeleon (South)	11:53:00	-79:06:00	160–170	3–4	-	Luhman (2007b)
λ Orionis	05:35:16	+09:42:00	402	5	-	Barrado y Navascués et al. (2004b)
Chamaeleon (North)	11:53:00	-79:06:00	160–170	5–6	-	Luhman (2007b)
NGC 2547	08:10:26	-49:10:03	457	30	-0.16	Jeffries et al. (2004)
IC 2391	08:40:36	-53:02:00	146	50	$\sim$0	This work
Pleiades	03:47:24	+24:07:00	150,130	120	$\sim$0	Bouvier et al. (2008),Bihain et al (2006)
Blanco 1	00:03:24	-30:08:00	260	100–150	0.04	Moraux et al. (2007)
M35	06:09:06	+24:21:00	1076	160	-0.21	Barrado y Navascuś et al. (2001a)
Hyades	04:26:52	+15:52:00	46	625	0.14	Bouvier et al. (2008)

Chapter 7

Summary and conclusions

In this last chapter we review the work presented in this thesis. We first recall the results and conclusions obtained from our photometric survey of the open cluster IC 2391. (We will not give a review of the observations and the procedure for candidates selection. The reader is referred to Chapter 3 and 4 respectively for a complete and detailed discussion.) Then we will present the main conclusions drawn from our analysis of JHK_{s} photometry in the area of IC 2391, available with 2MASS, and the analysis of the mass functions of open clusters of different ages and of different environments. We will complete this chapter by discussing the ejection scenario as a formation process of brown dwarfs and the future work recommended in order to improve our knowledge in the area of brown dwarf formation and evolution.

7.1   Review of our IC 2391 survey

We have performed a multi-band photometric survey over 10.9 square degrees of the open cluster IC 2391, and completed a preliminary spectroscopic follow-up of brown dwarfs and very low-mass star candidates from two fields. Our objective was to study, in detail, the mass function of this cluster, and in particular its radial dependence. We observed a radial variation in the mass function from 0.15 to $0.5\,M_\odot$ and have argued that this is a signature of mass segregation, presumably via dynamical evolution. This is consistent with theoretical predictions since the age of IC 2391 is half of its relaxation time. In contrast, we do not observe a significant radial variation in the mass function below $0.15\,M_\odot$. Although this absence of radial variation of the brown dwarf population could be in agreement with the ejection scenario of brown dwarf formation, the fact that we do not observe a discontinuity in the mass function across the stellar/substellar boundary ($0.072\,M_\odot$) implies that the ejection formation scenario is not a significant brown dwarf formation mechanism in this cluster, if this formation mechanism results in a higher velocity dispersion of brown dwarf compared to stars. On the other hand, if the ejection mechanism is a dominant brown dwarf formation path in this cluster, then both brown dwarfs and stars should have the same velocity dispersion.

In addition to the radial study, we derived a mass function from four central deeper fields as well as from five fields near the edge of the cluster observed with only three filters (the outward fields). In both cases we see an apparent rise in the number of objects below $0.05\,M_\odot$ ($\log M = -1.3$), but we concluded that this is an artifact of residual contamination by field M dwarfs. This was also seen by Barrado y Navascués et al. (2004a). The fact that we don't see this rise in the radial fields is because they were observed with *both* the J and R_c filters in addition to the medium band filters. This longer spectral baseline permits a better determination of the energy distributions and thus helps the rejection of objects (in particular field M dwarfs) based on observed magnitude vs. predicted magnitude from models.

Another apparent rise in the mass function over the 0.5–$1.0\,M_\odot$ interval (also observed by Jeffries et al. 2004 for NGC 2547) is due to background giants. Red giant contamination may be reduced by using medium bands such as $770/19$, $815/20$, $856/14$ and $914/27$, and theoretical colours of red giants (Hauschildt et al. 1999b). Our spectroscopic follow-up has confirmed that selection based on these filters resulted in no red giant contaminants among a sample of 61 candidates. This, and the fact that the radial fields have viewer contamination by field M dwarfs, indicates that middle band filters ($770/19$, $815/20$, $856/14$ and $914/27$) and the broad band filters R_c and J, are an optimal choice of a survey of objects with masses from $0.9\,M_\odot$ down to $0.02\,M_\odot$.

We see some variation in the colours of the main (field star) locus which we attribute to variable extinction affecting the background stars. This underlines the need for spectroscopic observations in this cluster to confirm membership or brown dwarf status in individual cases.

We have performed a preliminary spectroscopic follow-up of photometric candidates in two of our deep fields (0.5 sq. degrees). Of 61 photometric candidates, we confirm 19 objects (a third) as true cluster members. Of these, 7 are new brown dwarf members of IC 2391 (in the sense that they fulfill our spectroscopic and photometric criteria). Using our derived mass functions for the deep and radial fields, we expect there to be seven more brown dwarfs in the mass range 0.045 to $0.07\,\mathrm{M_\odot}$ and up to 38 in all the other radial fields in the same mass range.

Ultimately, we would need to perform a spectroscopic follow-up on all the photometric candidates in the radial, outward and deep fields. However, considering the time pressure on multi-object spectrograph, such as the *VIsible MultiObject Spectrograph* at the *European Southern Observatory*, *AAOmega* at the *Anglo-Australian Observatory* and *HYDRA* at *Cerro Tololo Inter-American Observatory* , it is very difficult to perform such spectroscopic follow-up on a time scale of a PhD program. However, we are currently performing a spectroscopic follow-up of our photometric candidates in field 3, 9, 20 and 24. It will then be possible to confirm, by selecting real physical members based on spectroscopy, the radial variation observed in photometry.

Finally, we find that the Hα line cannot be used as a membership criterion from fibre spectroscopy at low spectral resolution (spectral dispersion of $1.14\,\mathrm{\AA}$per pixel) because of spatially variable diffuse Hα emission. This prevents reliable sky subtraction around this line when using a fibre spectrograph with fibers assigned for sky subtraction.

7.2 Survey of IC 2391 based only on JHK_s photometry from 2MASS

The data from the public survey 2MASS was used in order to have a uniform sample (1) where the same instrument and telescope setup is used, and (2) where the sample of data is obtained and reduced independently from our work. We use the same photometric selection procedure as for our photometric survey of IC 2391. We obtain a disagreement between the mass function, the cumulative function and the radial profile of IC 2391 obtained with our optical survey and with 2MASS data. We have attributed such discrepancies to the fact that there is a low sensitivity in the energy distribution in JHK_s bands from $1.4\,\mathrm{M_\odot}$

down to $0.03_{\odot}$ and determination of mass and effective temperature based on the energy distributions would be erroneous, and therefore, the rejection of objects based on observed magnitude vs. the predicted magnitude discrepancy would be inefficient. We have used again the data from 2MASS but without the fourth reduction step (which is the rejection of objects based on observed magnitude vs. the predicted magnitude discrepancy) and used only the J in order to obtain masses and effective temperatures. We obtained an overcontamination above $0.3\,M_{\odot}$ and this was also confirmed with the sudden increase of the cumulative function at $0.5M_{\odot}$ and the constant increase of the radial plot of objects with masses above $0.5\,M_{\odot}$. From this we conclude that JHK_{s} alone cannot be reliably used to characterize a population of low mass objects (with masses lower then $0.7\,M_{\odot}$) such as those in IC 2391 (with an age of $50\,$Myr and a solar metallicity).

7.3 Open clusters from different ages and environments

We have used stellar/substellar mass functions from the literature in order to analyze any possible variation of the mass functions of several open clusters at different ages and environments, different metallicity being the indicator of different environment.

We observed that there was no significant variation between the ratio of both stellar and very low-mass star population with the brown dwarf population with age below $10\,$Myr, which is in total disagreement with a unique formation process of brown dwarfs by the ejection scenario if the velocity dispersion were higher for brown dwarfs than for stars. Also, we can observe that beyond $30\,$Myr the ratio of brown dwarfs to stars and very low-mass stars to stars are both decreasing and would be an indication of dynamical evaporation of the lighter objects. Finally, we observed that at all ages the ratio of very low-mass stars to stars are higher than both ratios of brown dwarfs to stars and brown dwarfs to very low-mass stars. This is an indication that the mean mass of the mass function stays in the mass range of 0.072–$0.2\,M_{\odot}$ at all ages.

We observed that there is no significant variation of the ratio of very low-mass stars to stars with metallicity, which would indicate that there is no variation of the stellar mass function with environment. We further observed that at solar metallicity the ratios of the brown dwarf population with very low-mass stars stay within $1/2$–2. On the other hand, the metal poor cluster NGC 2547 ([Fe/H]=-0.16) shows a very low substellar population compared to the population of stellar objects. This would be in agreement with the fact that lower metallicity in a cloud where star formation occurs would imply a higher Jeans

mass, and thus, a higher characteristic mass. However, considering the very few data points available, our conclusions regarding variation of the mass function with metallicity should be taken with care.

7.4 Conclusions on possible brown dwarf formation mechanism

We recall here the four main possible brown dwarf formation mechanisms presented in §1.2. These mechanisms are (1) formation in a similar way to stars, which is from the compression and fragmentation of a dense molecular cloud, (2) formation by gravitational instability of a disk, (3) formation like stars but with the accretion process interrupted during the protostellar stage, which is by photoevaporation and (4) dynamical ejection of the brown dwarf from its accretion envelope.

Because of the nature of our work (mass function and survey covering 0.02 to $\sim 0.9\,M_\odot$), it is not possible to explicitly put constraints of the formation by photoevaporation, as this would require observations of the spatial distribution of brown dwarfs compared to more massive stars, such as OB stars (with mass higher than $3\,M_\odot$).

Also, it is not possible with our work to put constraints on the planet-like formation. Indeed, one would need to perform a survey of brown dwarfs in binarity (stars–brown dwarf and brown dwarf–brown dwarf) and see if there is any variation with age, environment and with separation between the primary and the secondary objects in the binary system. However, this was not the goal of our survey on IC 2391.

From the data we have obtain for IC 2391 and the analysis of mass functions from various open clusters obtained from the literature, the ejection mechanism can be the dominant brown dwarf formation path if both brown dwarfs and stars have the same velocity dispersion.

However, if brown dwarfs and stars have the same velocity dispersion, our work cannot reject the star-like formation mechanism, as the similarity of velocity dispersion for both stars and brown dwarfs is an observational signature of star-like formation.

It is not possible from the mass function of IC 2391, and from the other clusters obtained from the literature, to conclude which formation scenarios, between star-like and ejection, is the most probable. However, our work was able to put a constraint on the brown dwarf formation mechanisms, which was the primary objective of this thesis.

We have shown the usefulness of performing a survey in open cluster in order to observe brown dwarfs and to obtain the stellar and substellar mass function. In order to fully exploit the mass function of open cluster as a tool, we need to enlarge available sample. Indeed, it can be seen from Figure 6.3 that there is a poor number of clusters in the age range of 6–30 Myr and above 200 Myr with known mass function covering the substellar population. There are even fewer of these clusters with known metallicity.

Furthermore, one would need to observe different clusters using the same (1) instruments and filter, (2) data reduction procedure and (3) photometric selection. Indeed, we have shown in this thesis that, even if the instruments used and the selection procedure were the same, different mass functions were obtained because different filters were available (different mass function from the deep field, radial field, and outward fields for our survey of IC 2391, §5.1). Also, we have seen in §5.3 that a modification of the selection procedure was able to cause large modification to the mass function. We therefore need, in the near future, to obtain a uniform set of mass functions on open clusters in the age range of 6–30 Myr and above 200 Myr (with determination of their metallicity) in order to improve our analysis such as those presented in §6.1.

In addition to the selection procedure used in this work, which is efficient in removing background red giants and field M–dwarfs, the use of proper motion can easily remove background contaminants and high-proper motion objects. Unfortunately, depending on the proper motion of the cluster observed, this could require a significantly long baseline between a series of observations, as 8 yr was even not sufficient to perform a selection on IC 2391 based on proper motion.

If the objective of a survey in an open cluster is to study the behavior of the stellar and substellar populations, a survey reaching the mass interval 0.02–0.055 $M_\odot$, such as our survey, is sufficient to accomplish this scientific goal. A complete coverage of a cluster in a survey is needed if the scientific goal is the spatial distribution of a radial cumulative function is desired. If the scientific goal is the study of the radial variation of the various population of a cluster, then full coverage is not required, as shown by our work. Also, the choice of filter should be based on the sensitivity of the magnitudes in each band and colours with effective temperature, and not only on the very simple reasoning of *cool objects so very red filters*, as this would have given, for instance, very bad results for a simple JHK_s survey of IC 2391. This should be pointed out to people planning to use the JHK_s data from the *UKIRD Infrared Deep Sky Survey*.

Acknowledgements

First, I acknowledge my supervisor Coryn A.L. Bailer-Jones for all the time spent on teaching me. Not only I learned to learn by myself, but also how to be a scientist, with all the responsibility that this implies (from writing efficient proposals to making the appropriate tests on data obtained). This teaching was a very long process and lasted for three years, and I'm still learning from him. So I thank him for being patient with me and for the interest he showed in the work I presented to him. Furthermore, the several readings of this documents and the comments he gave me improved the quality of this thesis. Finally, I acknowledge him for giving me the opportunity to come to Heidelberg to perform my PhD. This allowed me to learn a lot and to meet many new people, and for this he has my thanks.

I want to thank some other people involved in astronomy for having shown an interest in my work by reading my proposals, papers and/or listening to my talks. The comments and help they gave me was more than appreciated. These people are José Caballero, Matthew Colman, Bertrand Goldman, Dimitrios Gouliermis, Ralf Klessen and Reinhard Mundt.

The referees of my thesis committee (Coryn A.L. Bailer-Jones, Max Camenzind, Ralf Klessen and Reinhard Mundt) are acknowledged for being in my oral defense and for reading this thesis. I also acknowledge the following people for reading parts of my thesis and for giving me their comments, corrections and translations: Joseph Carson, Christian Elting, Cassie Fallscheer, Kelly Foyle, Rory Holmes, Owen Matthews, Reinhard Mundt, Rosalind Skelton, Kester Smith and Ingo Waldmann.

Bibliography

Adams, T., Davies, M. B., Jameson, R. F. & Scally, A., 2002a, MNRAS, 333, 547

Adams, J. D., Stauffer, J. R., Skrutskie, M. F., Monet, D. G., Portegies Zwart, S. F., Janes, K. A. & Beichman, C. A., 2002a, AJ, 124, 1570

Allard, F., Hauschildt, P. H., Alexander, D. R. & Starrfield, S., 1997, ARA&A, 35, 137

Allard, F., Hauschildt, P. H., Alexander, D. R., Tamanai, A., & Schweitzer, A., 1997, ARA&A, 35,

Baade, D., Meisenheimer, K., Iwert, O., Alonso, J., Augusteijn, T., Beletic, J., Bellemann, H., Benesch, W., Böhm, A., Böhnhardt, H., Brewer, J., Deiries, S., Delabre, B., Donaldson, R., Dupuy, C., Franke, P., Gerdes, R., Gilliotte, A., Grimm, B., Haddad, N., Hess, G., Ihle, G., Klein, R., Lenzen, R., Lizon, J.-L., Mancini, D., Münch, N., Pizarro, A., Prado, P., Rahmer, G., Reyes, J., Richardson, F., Robledo, E., Sanchez, F., Silber, A., Sinclaire, P., Wackermann, R. & Zaggia, S., 1999, The Messenger 95, 15

Bailer-Jones, C. A. L. & Mundt, R., 2001, A&A, 367, 218

Baraffe, I., Chabrier, G., Allard, F. & Hauschildt, P. H., 1998, A&A, 337, 403

Baraffe, I., Chabrier, G., Allard, F. & Hauschildt, P. H., 2002, A&A, 382, 563

Barrado y Navascués, D., Stauffer, J. R. & Patten, B. M., 1999, ApJ, 522, 53

Barrado y Navascués, D., Stauffer, J. R., Briceño, C., Patten, B., Hambly, N. C. & Adams, J. D., 2001a, ApJS, 134, 103

Barrado y Navascués, D., Stauffer, J. R., Bouvier, J. & Martín, E. L., 2001b, ApJ, 546, 1006

Barrado y Navascués, D., Stauffer, J. R. & Jayawardhana, R., 2004, ApJ, 614, 386

Barrado y Navascués, D., Stauffer, J. R., Bouvier, J., Jayawardhana, R. & Cuillandre, J.-C., 2004, ApJ, 610, 1064

Basri, G., 2000, ARA&A, 38, 485

Bate, M. R., Bonnell, I. A. & Bromm, V., 2002, MNRAS, 332, 65L

Bate, M. R., Bonnell, I. A. & Bromm, V., 2003, MNRAS, 339, 577

Bate, M. R. & Bonnell, I. A., 2005, MNRAS, 356, 1201

Baumgardt, H. & Makino, J., 2003, MNRAS, 340, 227

Bergeron, P., Leggett, S. K. & Ruiz, M. T., 2001, ApJS, 133, 413

Bihain, G., Rebolo, R., Béjar, V. J. S., Caballero, J. A., Bailer-Jones, C. A. L., Mundt, R., Acosta-Pulido, J. A. & Manchado Torres, A., 2006, A&A, 458, 805

Bonnell, I. A. & Davies, M. B., 1998, MNRAS, 295, 691

Boss, A. P., 2001, ApJ, 551, 167

Boudreault, S. & Bailer-Jones, C. A. L., 2008, ApJ, *submitted*

Bouvier, J., Kendall, T. T., Meeus, G., Testi, L., Moraux, E., Stauffer, J. R., James, D., Cuillandre, J. -C., Irwin, J., McCaughrean, M. J., Baraffe, I. & Bertin, E., 2008, A&A, 481, 661

Briceño, C., Luhman, K. L., Hartmann, L., Stauffer, J. R. & Kirkpatrick, J. D., 2002, ApJ, 580, 317

Caballero, J. A., Béjar, V. J. S., Rebolo, R., Eislffel, J., Zapatero-Osorio, M. R., Mundt, R., Barrado Y Navascués, D., Bihain, G., Bailer-Jones, C. A. L., Forveille, T. & Martín, E. L., 2007, A&A, 470, 903

Caballero, J. A., 2008, MNRAS, 383, 375

Carpenter, J. M., Meyer, M. R., Dougados, C., Strom, S. E. & Hillenbrand, L. A., 1999, AJ, 114, 198

Chabrier, G., Baraffe, I., Allard, F. & Hauschildt, P. H., 2000, A&A, 542, 464

Chabrier, G. & Baraffe, I., 2000, ARA&A, 38, 337

Chabrier, G., 2003, ApJ, 586, 133

Chabrier, G., 2003, PASP, 115, 763

Clark, P. C., Bonnell, I. A., Klessen, R. S., 2008, MNRAS, 386, 3

Colina, L., Bohlin, R. & Castelli, F., 1996, Instrument Science Report CAL/SCS, 8, 1

D'Antona, F. & Mazzitelli, I., 1985, ApJ, 296, 502

Deacon, N. R. & Hambl, N. C., 2004, A&A, 416, 125

Dobbie, P. D., Pinfield, D. J., Jameson, R. F. & Hodgkin, S. T., 2002, MNRAS, 335, 79L

Dodd, R. J., 2004, MNRAS, 355, 959

Dreyer, J. L. E., 1895, Mem. R. Astron. Soc., 51, 185

Elmegreen, B. G., 1999, ApJ, 522, 915

Elson, R., Hut, P. & Inagaki, S., 1987, ARA&A, 25 565

Fischer, P., Pryor, C., Murray, S., Mateo, M., & Richtler, T., 1998, AJ, 115, 592

de La Fuente Marcos, R. & de La Fuente Marcos, C., 2000, Ap&SS, 271, 127

González-García, B. M., Zapatero-Osorio, M. R., Béjar, V. J. S., Bihain, G., Barrado Y Navascués, D., Caballero, J. A., Morales-Calderón, M., 2006, A&A, 460, 799

Goodwin, S. P. & Whitworth, A., 2007, A&A, 466, 943

Grossman, A. S., 1970, ApJ, 161, 619

Hambly, N. C., Hodgkin, S. T., Cossburn, M. R. & Jameson, R. F., 1999, MNRAS, 303, 835

Hamuy, M., Walker, A. R., Suntzeff, N. B., Gigoux, P., Heathcote, S. R. & Phillips, M. M., 1992, PASP, 104, 533

Hamuy, M., Suntzeff, N. B., Heathcote, S. R., Walker, A. R., Gigoux, P. & Phillips, M. M., 1994, PASP, 106, 566

Hanuschik, R. W., 2003, A&A, 407, 1157

Hauschildt, P. H., Allard, F. & Baron, E., 1999, ApJ, 512, 377

Hauschildt, P. H., Allard, F., Ferguson, J., Baron, E. & Alexander, D. R., 1999b, ApJ, 525, 871

Hayashi C., Nakano T., 1963, Prog. Theor. Phys., 30, 460

Henry, T. J., Jao, W.-C., Subasavage, J. P., Beaulieu, T. D., Ianna, P. A., Costa, E. & Méndez, R. A., 2006, AJ, 132, 2360

Hester, J. J., Scowen, P. A., Sankrit, R., Lauer, T. R., Ajhar, E. A., Baum, W. A., Code, A., Currie, D. G., Danielson, G. E., Ewald, S. P., Faber, S. M., Grillmair, C. J., Groth, E. J., Holtzman, J. A., Hunter, D. A., Kristian, J., Light, R. M., Lynds, C. R., Monet, D. G., O'Neil, E. J., Jr., Shaya, E. J., Seidelmann, K. P. & Westphal, J. A., 1996, AJ, 111, 2349

Hester, J. J., 1997, AIP Conf. Proc., 393, 143

Hillenbrand, L. A. & Carpenter, J. M., 2000, ApJ, 540, 236

Hogg, A. R., 1960, PASP, 72, 85

Howell, S. B. 1989, PASP, 101, 616

Jameson, R. F., Dobbie, P. D., Hodgkin, S. T. & Pinfield, D. J., 2002, MNRAS, 335, 853

Jeffries, R. D., Naylor, T., Devey, C. R. & Totten, E. J., 2004, MNRAS, 351, 1401

Joergens, V., 2006, A&A, 448, 655

Kharchenko, N. V., Piskunov, A. E., Röser, S., Schilbach, E. & Scholz, R.-D., 2005, A&A, 438, 1163

King, I. R., 1962, AJ, 67, 471

Klessen, R. S. & Burkert, A., 2001, ApJ, 549, 386

Koen, C. & Ishihara, I., 2006, MNRAS, 369, 846

Kontizas, M., Hatzidimitriou, D., Bellas-Velidis, I., Gouliermis, D., Kontizas, E., & Cannon, R. D., 1998, A&A, 336, 503

Kraus, A. L. & Hillebrand, L. A., 2007, AJ, 134, 2340

Kroupa, P., 2001, MNRAS, 322, 231

Kroupa, P., 2002, Science, 295, 82

Kroupa, P. & Bouvier, J., 2003, MNRAS, 346, 369

Koen, C. & Ishihara, A., 2006, MNRAS, 369, 846

Kulkarni, S. & Golimowski, D., 1995, News Release Number: STScI-1995-48

Kumar, S. S., 1963, ApJ, 137, 1121

Kumar, M. S. N. & Schmeja, S., 2007, A&A, 471, 33

Lodieu, N., Dobbie, P. D., Deacon, N. R., Hodgkin, S. T., Hambly, N. C. & Jameson, R. F., 2007, MNRAS, 380, 712

Loibl, B., 1978, A&A, 68, 107

Loktin, A. V. & Beshenov, G. V., 2003, Astronomy Reports, 47, 6

Luhman, K. L. & Rieke, G. H., 1999, ApJ, 525, 440

Luhman, K. L., 1999, ApJ, 525, 466

Luhman, K. L., 2000a, ApJ, 544, 1044

Luhman, K. L., Rieke, G. H., Young, Erick T., Cotera, A. S., Chen, H., Rieke, M. J., Schneider, G., Thompson, R. I., 2000b, ApJL, 540, 1016

Luhman, K. L., 2004, ApJ, 617, 1216

Luhman, K. L., Lada, C. J., Hartmann, L, Muench, A. A., Megeath, S. T., Allen, L. E., Myers, P. C., Muzerolle, J., Young, E. & Fazio, G. G., 2005, ApJL, 631, L69

Luhman, K. L., 2006, ApJ, 645, 676

Luhman, K. L., Adame, L., D'Alessio, P., Calvet, N., McLeod, K. K., Bohac, C. J., Forrest, W. J., Hartmann, L., Sargent, B. & Watson, D. M., 2007a, ApJ, 666, 1219

Luhman, K. L., 2007b, ApJS, 173, 104

Luhman, K. L., Joergens, V., Lada, C., Muzerolle, J., Pascucci, I. & White, R., 2007c, Protostars and Planets V, 443

Martín, E. L., Rebolo, R. & Zapatero-Osorio, M. R., 1996, ApJ, 469, 706

Manzi, S., Randich, S., de Wit, W. J. & Palla, F., 2008, A&A, 479, 141

Marino, A., Micela, G., Peres, G., Pillitteri, I. & Sciortino, S., 2005, A&A, 430, 287

McNamara, B. R. & Ianna, P. A., 1986, BAAS, 18, 1037

Miller, G. E. & Scalo, J. M., 1979, ApJS, 41, 513

Moraux, E., Bouvier, J., Stauffer, J. R. & Cuillandre, J.-C., 2003, A&A, 400, 891

Moraux, E., Bouvier, J., Stauffer, J. R., Barrado y Navascués, D. & Cuillandre, J.-C., 2007, A&A, 471, 499

Muench, A. A., Lada, E. A., Lada, C. J. & Alves, J., 2002, ApJ, 573, 366

Muench, A. A., Lada, E. A., Lada, C. J., Elston, R. J., Alves, J. F., Horrobin, M., Huard, T. H., Levine, J. L., Raines, S. N. & Román-Zúñiga, C., 2003, AJ, 125, 2029

Osterbrock, D. E., Fulbright, J. P., Martel, A. R., Keane, M. J., Trager, S. C. & Basri, G., 1996, PASP, 108, 277

Padoan, P. & Nordlund, Å, 2004, ApJ, 617, 559

Parker, Q. A., Phillipps, S., Pierce, M. J., Hartley, M., Hambly, N. C., Read, M. A., MacGillivray, H. T., Tritton, S. B., Cass, C. P., Cannon, R. D., Cohen, M., Drew, J. E., Frew, D. J., Hopewell, E., Mader, S., Malin, D. F., Masheder, M. R. W., Morgan, D. H., Morris, R. A. H., Russeil, D., Russell, K. S., Walker, R. N. F., 2005, MNRAS, 362, 689

Patten, B. M. & Pavlovsky, C. M., 1999, PASP, 111, 210

Patten, B. M. & Simons, T., 1996, ApJS, 106, 489

Patten, B. M. & Simons, T., 1993, ApJ, 415, 123

Pavlenko, Y. V., van Loon, J. T., Evans, A., Rushton, M. T., Kaminsky, B. M., Filippenko, A. V., Foley, R. J., Li, W., Smalley, B. & Yakovina, L. A., 2006, A&A, 460, 245

Perry, C. L. & Hill, G., 1969 AJ, 74, 899

Pickett, B. K., Durisen, R. H., Cassen, P. & Mejia, A. C., 2000, ApJ, 540, 95

Piotto, G., Bedin, L. R., Anderson, J., King, I. R., Cassisi, S., Milone, A. P., Villanova, S., Pietrinferni, A. & Renzini, A., 2007, ApJ, 661, 53

Piskunov, A. E., Schilbach, E., Kharchenko, N. V., Rser, S. & Scholz, R.-D., 2007, A&A, 468, 151

Platais, I., Melo, C., Memilliod, J.-C., Kozhurina-Platais, V., Fulbright, J. P., Méndez, R. A., Altmann, M. & Sperauskas, J., 2007, A&A, 461, 509

Raboud, D., & Mermilliod, J.-C. 1998, A&A, 333, 897

Randich, S. Y., Pallavicini, R., Meola, G., Stauffer, J. R. & Balachandran, S. C., 2001, A&A, 372, 862

Rebolo, R., Martín, E. L., Basri, G., Marcy, G. W. & Zapatero-Osorio, M. R., 1996, ApJ, 469, L53

Reipurth, Bo, 2000, AJ, 120, 3177

Reipurth, B. & Clarke, C., 2001, AJ, 122, 432

Robichon, F., Arenou, F., Mermilliod, J.-C. & Turon, C., 1999, A&A, 345, 471

Rolleston, W. R. J. & Byrne, P. B., 1997, A&AS, 126, 357

Salpeter, E. E., 1955, ApJ, 121, 161

Sanner J. & Geffert M., 2001, A&A, 370, 87

Saumon, D., Hubbard, W. B., Burrows, A., Guillot, T., Lunine, J. I. & Chabrier, G., 1996, ApJ, 460, 993

Schilbach, E., Kharchenko, N. V., Piskunov, A. E., Röser, S. & Scholz, R.–D., 2006, A&A, 456, 523

Schlegel, D. J., Finkbeiner, D. P. & Davis M., 1998, ApJ, 500, 525

Siegler, N., Muzerolle, J., Young, E., Rieke, G. H., Mamajek, E. E., Trilling, D. E., Gorlova, N.& Su, K. Y. L., 2007, ApJ, 654, 580

Simon, T. & Patten, B., 1998, PASP, 110, 283

Sirianni, M., Nota, A., De Marchi, G., Leitherer, C. & Clampin, M., 2002, ApJ, 579, 275

Slesnick, C. L., Hillenbrand, L. A. & Carpenter, J. M., 2004, ApJ, 610, 1045

Stamatellos, D., Hubber, D. A. & Whitworth, A. P., 2007, MNRAS, 382, 30

Stauffer, J., Hartmann, L. W., Jones, B. F. & McNamara, B. R., 1989, ApJ, 342, 285

Stütz, Ch., Bagnulo, S., Jehin, E., Ledoux, C., Cabanac, R., Melo, C.& Smoker, J. V., 2006, A&A, 451, 285

Sung, H., Bessell, M. S. & Chun, M.-Y., 2004, AJ, 128, 1684

Tarter, J., 1975, PhD thesis. Univ. Calif., Berkeley. 120 pp.

Thies, I. & Kroupa, P., 2007, ApJ, 671, 767

Watkins, S. J., Bhattal, A. S., Boffin, H. M. J., Francis, N., Whitworth, A. P., 1998, MNRAS, 300, 1214

Whitworth, A. P. & Zinnecker, H., 2004, A&A, 427, 299

Whitworth, A. P. & Stamatellos, D., 2006, A&A, 458, 817